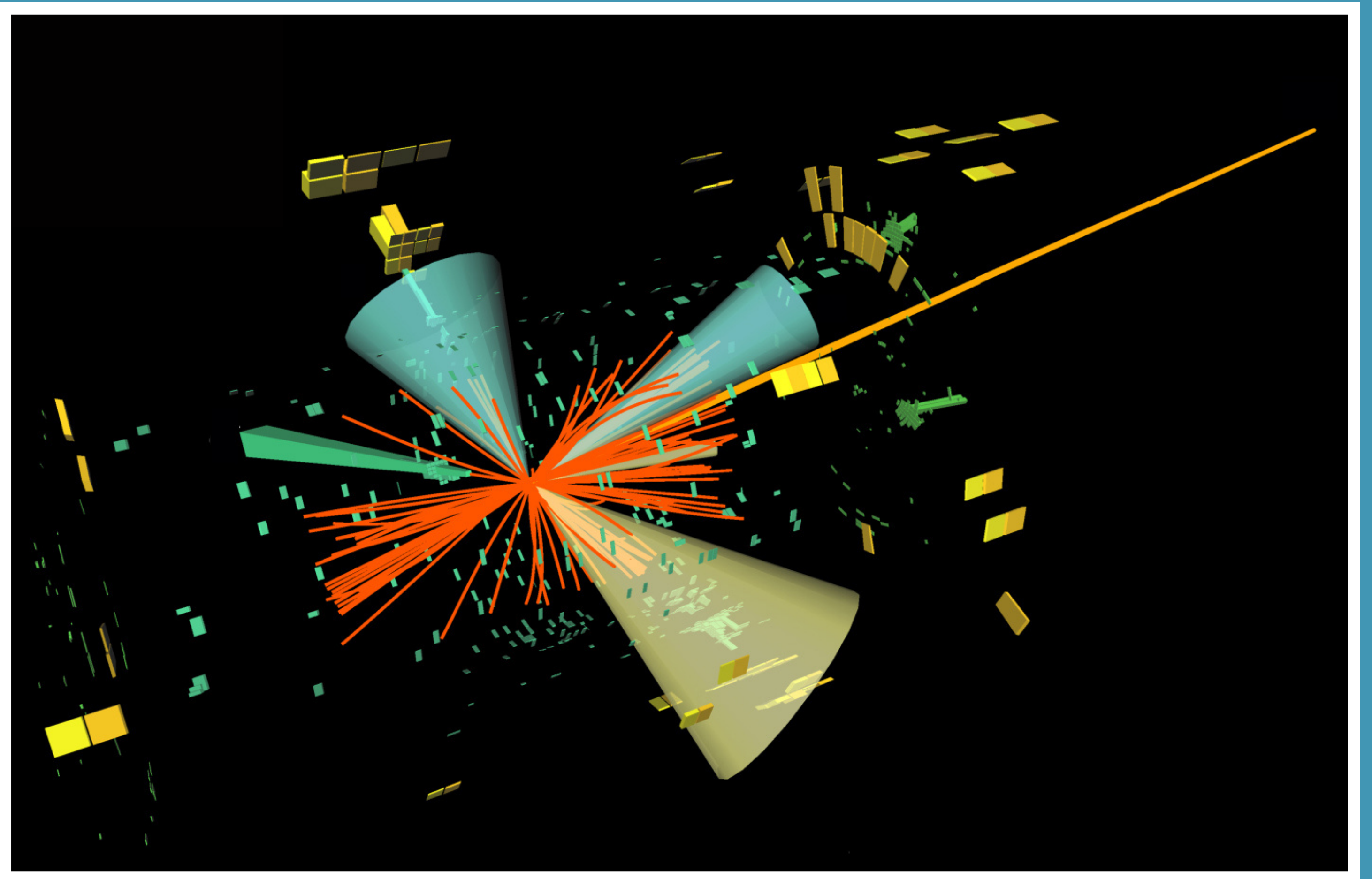




Istituto Nazionale di Fisica Nucleare
LABORATORI NAZIONALI DI FRASCATI

FRASCATI PHYSICS SERIES



Seventh Young Researchers' Workshop

Physics Challenges in the LHC Era

2022

EDITORS:

G. Corcella, G. Grilli di Cortona, E. Nardi, A. Paoloni,
S. Pisano, A. Plascencia, M. Testa

FRASCATI PHYSICS SERIES

Series Editor
Antonella Antonelli

Technical Editor
Lia Sabatini

Cover by Elisa Santinelli

Volume LXXII

Istituto Nazionale di Fisica Nucleare – Laboratori Nazionali di Frascati
Divisione Ricerca
Ufficio Biblioteca e Pubblicazioni Scientifiche
P.O. Box 13, I-00044 Frascati Roma Italy
email: library@lists.lnf.infn.it

Copyright © 2022 by INFN

All rights reserved. No part of this publication may be reproduced, stored in a retrieval system or transmitted in any form or by any means, electronic, mechanical, photocopying, recording or otherwise, without the prior permission of the copyright owner.
ISBN 978-88-86409-74-2

7th Young Researchers' Workshop
Physics Challenges in the LHC Era
2022

PREFACE

The Seventh Young Researchers' Workshop 'Physics Challenges in the LHC Era' took place on July 11th and 14th, 2022, as part of the program of the XX edition of the Summer/Spring School 'Bruno Touschek' in Nuclear, Subnuclear and Astroparticle Physics, which was held at INFN, Laboratori Nazionali di Frascati (LNF). Through the years, the Young Researchers' Workshop series has become an important opportunity for graduate students and young postdoctoral fellows to present their research activity to an audience with both junior and experienced researchers in theoretical and experimental nuclear, particle and astroparticle physics.

The 2022 edition featured a number of very impressive talks discussing pretty diverse topics. From the experimental side, we had presentations highlighting detectors and results from the LHC experiments, such as ATLAS, CMS and LHCb, as well as NA61/SHINE and AMS. From the theory viewpoint, the workshop talks dealt with the leptonic $g-2$ anomaly, inflation, gravitational waves, extensions of the Standard Model, such as scenarios predicting light vectors or Twin Higgs bosons, oscillations of neutrinos, leptogenesis, axions and dark sectors. The present volume contains contributions which summarize the presentations given at the Young Researchers' Workshop: in many cases, they represent the first peer-reviewed publication for the school participants as sole authors.

Before concluding, as chairman of the XX 'Bruno Touschek' Summer School and Young Researchers' Workshop, I wish to warmly thank all co-organizers, the School secretary, the lecturers and, above all, the young participants who livened up the event and contributed to create a friendly as well as scientifically stimulating atmosphere.

Frascati, December 22, 2022

Gennaro Corcella
(Chairman of the 7th Young Researcher Workshop)

CONTENTS

<i>Carlos Mirò</i>	Addressing leptonic g-2 anomalies in a flavor-conserving Two-Higgs-Doublet model	1
<i>Nico Alexis Benincasa</i>	Multi-step phase transitions and gravitational waves in the inert doublet model	9
<i>Giulia Manco</i>	Colouring the jets at LHC for Xbb tagger improvement	20
<i>Daniela Mascione</i>	Pruning Deep Neural Networks for LHC challenges	27
<i>Aleksei Chernov</i>	Studying radiative charm-meson decays at the LHCb experiment	32
<i>Jòzef Borsuk</i>	Analysis of the $B^0 \rightarrow K^{*0} \mu^+ \mu^-$ decay in the high $K\pi$ invariant-mass region at the LHCb experiment	39
<i>Camille Normand</i>	On the effective lifetime of $B_s \rightarrow \mu\mu\gamma$	45
<i>Clara Landesa Gómez</i>	Strange particle production in pPb collisions at the LHCb experiment	53
<i>Yuliia Balkova</i>	Strangeness production in the NA61/SHINE experiment at the CERN SPS energy range	60
<i>Federico Montekali</i>	New Small Wheel Micromegas trigger simulation analysis	66
<i>Saswat Mishra</i>	Cross-section measurement of $VH \rightarrow b\bar{b}$ process at CMS experiment	73
<i>Ipsita Ray</i>	Extraction of $ V_{ub} $ from $B \rightarrow \pi l \nu$ modes	80
<i>Gülce Karagöz</i>	Measurement of the Helium flux in the low earth orbit with the Alpha Magnetic Spectrometer	86
<i>Claudio Toni</i>	Gauging the baryonic and lepton family numbers with harmless Wess-Zumino term	92
<i>Simone Marciano</i>	Neutrino Mixing and Leptogenesis in a $L_e - L_\mu - L_\tau$ model	99
<i>Gabriel Massoni Salla</i>	Probing dark abelian gauge sector at the intensity frontier	105
<i>Michał Łukawski</i>	Twin stau as a self-interacting dark matter	111
<i>Federica Fabiano</i>	Exclusive vector meson photoproduction in fixed-target collisions at LHCb	117

ADDRESSING LEPTONIC $g - 2$ ANOMALIES IN A FLAVOR CONSERVING TWO-HIGGS-DOUBLET MODEL

Carlos Miró

Departament de Física Teòrica and IFIC, Universitat de València-CSIC, E-46100, Burjassot, Spain
E-mail: Carlos.Miro@uv.es

Abstract

The discrepancy between the experimental determination of the muon and electron anomalous magnetic moments and their Standard Model expectations might be interpreted as New Physics. These anomalies can be addressed in the context of a general Flavor Conserving Two-Higgs-Doublet Model, which provides a simultaneous explanation in two regimes of scalar masses. The implications of the W boson mass measurement reported by the CDF Collaboration are also considered.

1 Introduction

Two anomalies related to the anomalous magnetic moment of leptons, $a_\ell = (g - 2)_\ell/2$, have emerged. On the one hand, there exists a 4.2σ tension between the Standard Model (SM) prediction and the experimental determination of the muon anomalous magnetic moment reported by the Muon $g - 2$ Collaboration ¹⁾,

$$\delta a_\mu^{\text{Exp}} = a_\mu^{\text{Exp}} - a_\mu^{\text{SM}} = (2.5 \pm 0.6) \times 10^{-9}. \quad (1)$$

Despite the current discrepancies concerning the data-driven computation of the Hadronic Vacuum Polarization contribution and the latest results published by some lattice collaborations ²⁾, we interpret this deviation as a sign of New Physics (NP). On the other hand, the electron anomalous magnetic moment might also be affected by NP. In this sense, depending on the input value of the fine structure constant determined from atomic recoils, a 2.4σ tension arises from ^{133}Cs measurements ³⁾ and a 1.6σ tension from ^{87}Rb measurements ⁴⁾

$$\delta a_e^{\text{Exp,Cs}} = -(8.7 \pm 3.6) \times 10^{-13}, \quad \delta a_e^{\text{Exp,Rb}} = (4.8 \pm 3.0) \times 10^{-13}. \quad (2)$$

A simultaneous explanation of these two anomalies has been considered in the context of general Flavor Conserving Two-Higgs-Doublet Models (2HDMs) ^{5, 6}, that can also accommodate the recent CDF W boson anomaly ⁷.

In the following, we present the main features of the model in section 2. The new contributions to a_ℓ are addressed in section 3. Finally, we discuss our results in section 4 and summarize in section 5. For further details on this work, we refer to ⁶.

2 Model

The most general Yukawa sector in 2HDMs, assuming massless neutrinos, can be written as

$$\mathcal{L}_Y = -\bar{Q}_L^0 (Y_{d1}\Phi_1 + Y_{d2}\Phi_2) d_R^0 - \bar{Q}_L^0 (Y_{u1}\tilde{\Phi}_1 + Y_{u2}\tilde{\Phi}_2) u_R^0 - \bar{L}_L^0 (Y_{\ell 1}\Phi_1 + Y_{\ell 2}\Phi_2) \ell_R^0 + \text{h.c.}, \quad (3)$$

where Q_L^0 and L_L^0 are the SM left-handed quark and lepton doublets, respectively; d_R^0 , u_R^0 and ℓ_R^0 , the SM right-handed quark and lepton singlets; Φ_1 and Φ_2 , the two Higgs doublets, with $\tilde{\Phi}_j \equiv i\sigma_2\Phi_j^*$; and Y_{fi} ($f = d, u, \ell$ and $i = 1, 2$), the 3×3 Yukawa coupling matrices. All fermionic fields must be understood as 3-dimensional vectors in flavor space. It is convenient to rotate the scalar fields into the so-called *Higgs basis*, where only one scalar doublet acquires a vacuum expectation value (vev). Then, going to the fermion mass basis via the usual bidiagonalization procedure, it is straightforward to obtain

$$\mathcal{L}_Y = -\frac{\sqrt{2}}{v}\bar{Q}_L(M_d H_1 + N_d H_2) d_R - \frac{\sqrt{2}}{v}\bar{Q}_L(M_u \tilde{H}_1 + N_u \tilde{H}_2) u_R - \frac{\sqrt{2}}{v}\bar{L}_L(M_\ell H_1 + N_\ell H_2) \ell_R + \text{h.c.}, \quad (4)$$

where the matrices M_f ($f = d, u, \ell$), coupled to the only Higgs doublet that acquires a vev, are the diagonal fermion mass matrices. However, the new flavor structures represented by the N_f matrices are not diagonal in general and thus can introduce dangerous Flavor Changing Neutral Currents. In order to avoid them, we consider a type I (or type X) quark sector, shaped by a \mathbb{Z}_2 symmetry, and a general Flavor Conserving (gFC) lepton sector, based on the hypothesis presented in ⁸). Therefore,

$$N_d = t_\beta^{-1} M_d, \quad N_u = t_\beta^{-1} M_u, \quad N_\ell = \text{diag}(n_e, n_\mu, n_\tau), \quad (5)$$

where $t_\beta \equiv \tan\beta = v_2/v_1$ is the ratio of the vevs of the scalar doublets in eq.3. The N_ℓ matrices in the lepton sector are diagonal, arbitrary and one loop stable under Renormalization Group Evolution (RGE) in the sense that they remain diagonal. The effective decoupling between muons and electrons arising from the independence of n_μ and n_e may allow us to explain both δa_ℓ anomalies within our I-gFC framework.

Completing the definition of the model, the scalar potential is built with the same \mathbb{Z}_2 symmetry, but it is softly broken by the term $(\mu_{12}^2 \Phi_1^\dagger \Phi_2 + \text{h.c.})$ with $\mu_{12}^2 \neq 0$ in order to have scalar masses larger than 1 TeV and values of t_β larger than 8. Furthermore, we neglect CP violation in the scalar and the Yukawa sectors. In this way, our scalar spectrum contains two CP-even neutral scalars $\{h, H\}$, one CP-odd pseudoscalar A and two charged scalars H^\pm , with no mixing between the CP eigenstates. We will identify the state h with the 125 GeV scalar discovered at the LHC: this condition will lead to the so-called *scalar alignment limit* where the h couplings are SM-like. Finally, the new lepton Yukawa couplings are real, i.e., $\text{Im}(n_\ell) = 0$.

3 New Physics contributions to a_ℓ

The complete theoretical prediction for the anomalous magnetic moment of lepton ℓ consists of the sum of the SM prediction, a_ℓ^{SM} , and the NP correction, δa_ℓ :

$$a_\ell^{\text{Th}} = a_\ell^{\text{SM}} + \delta a_\ell. \quad (6)$$

One can factorize out the typical one loop factors and the SM Higgs-like couplings from the NP term as

$$\delta a_\ell = K_\ell \Delta_\ell, \quad K_\ell = \frac{1}{8\pi^2} \left(\frac{m_\ell}{v} \right)^2. \quad (7)$$

Aiming to solve the lepton anomalies, that is $\delta a_\ell = \delta a_\ell^{\text{Exp}}$, one needs

$$\Delta_\mu \simeq 1, \quad \Delta_e^{\text{Cs}} \simeq -16, \quad \Delta_e^{\text{Rb}} \simeq 9. \quad (8)$$

On that respect, both one loop and two loop (of Barr-Zee type) diagrams can play a relevant role to explain the previous anomalies simultaneously. In the scalar alignment limit and keeping only leading terms in a m_ℓ^2/m_S^2 ($S = \text{H, A, H}^\pm$) expansion, the one loop result reads

$$\Delta_\ell^{(1)} \simeq |n_\ell|^2 \left(\frac{I_{\ell\text{H}}}{m_{\text{H}}^2} - \frac{I_{\ell\text{A}} - 2/3}{m_{\text{A}}^2} - \frac{1}{6m_{\text{H}^\pm}^2} \right), \quad (9)$$

where

$$I_{\ell S} = -\frac{7}{6} - 2 \ln \left(\frac{m_\ell}{m_S} \right). \quad (10)$$

Under the same assumptions, the two loop contribution is given by

$$\Delta_\ell^{(2)} \simeq -\frac{2\alpha}{\pi} \frac{\text{Re}(n_\ell)}{m_\ell} F, \quad (11)$$

where

$$F = \frac{t_\beta^{-1}}{3} [4(f_{t\text{H}} + g_{t\text{A}}) + (f_{b\text{H}} - g_{b\text{A}})] + \frac{\text{Re}(n_\tau)}{m_\tau} (f_{\tau\text{H}} - g_{\tau\text{A}}), \quad (12)$$

with $f_{fS} = f(m_f^2/m_S^2)$ and $g_{fS} = g(m_f^2/m_S^2)$ depending only on the scalar and fermion masses, as defined in ⁶). In the following section, we explore how to solve the lepton anomalies through these new contributions.

4 Analysis and results

The aim of this work is to identify which regions of the parameter space of the model are able to reproduce the δa_ℓ anomalies while satisfying all relevant low and high energy constraints. The list of constraints, modelled with a gaussian likelihood factor or an equivalent χ^2 term, reads as follows (for details, see ⁶).

- Perturbative unitarity of $2 \rightarrow 2$ high energy scattering of scalars, perturbativity of the quartic couplings in the scalar potential ⁹) and boundedness from below ¹⁰).
- Signal strengths of the 125 GeV Higgs boson ^{11, 12, 13, 14, 15, 16, 17, 18, 19, 20, 21, 22, 23}) that we identify with the CP-even state h: this condition forces the alignment limit in the scalar sector.

- Agreement with electroweak precision data through corrections in the oblique parameters S and T ^{24, 25}), that requires near degeneracies $m_{H^\pm} \simeq m_H$ and/or $m_{H^\pm} \simeq m_A$ in the scalar spectrum.
- LEP data from $e^+e^- \rightarrow \mu^+\mu^-, \tau^+\tau^-$ with center-of-mass energies up to $\sqrt{s} = 208$ GeV ²⁶): this constraint essentially imposes $m_H, m_A > 208$ GeV.
- LHC direct searches of new scalars: resonant processes $pp \rightarrow S \rightarrow \mu^+\mu^-, \tau^+\tau^-$ ($S = H, A$) via gluon-gluon fusion ^{27, 28, 29, 30, 31} and H^\pm searches in $pp \rightarrow H^\pm tb, H^\pm \rightarrow \tau\nu, tb$ ^{32, 33, 34, 35}).
- H^\pm -induced processes that must be kept under control in Lepton Flavor Universality (LFU) measurements concerning purely leptonic decays $\ell_j \rightarrow \ell_k \nu \bar{\nu}$ as well as pseudoscalar meson decays ($K, \pi \rightarrow e\nu, \mu\nu$ ^{24, 36, 37}), and in $b \rightarrow s\gamma$ and $B_q^0 - \bar{B}_q^0$ mixing processes ^{24, 38, 39}).
- Perturbativity upper bounds on the new lepton Yukawa couplings, namely $|n_\ell| \leq 250$ GeV.

In the plots below, we show selected results of the allowed parameter space of the model where $\delta a_\mu^{\text{Exp}}$ and $\delta a_e^{\text{Exp, Cs}}$ are solved (other scenarios concerning δa_e will be treated in the following section). The different colors represent three contours in the joint $\Delta\chi^2 = \chi^2 - \chi_{\text{Min}}^2$. In a 2D- $\Delta\chi^2$ distribution they correspond, darker to lighter, to 1, 2 and 3σ regions.

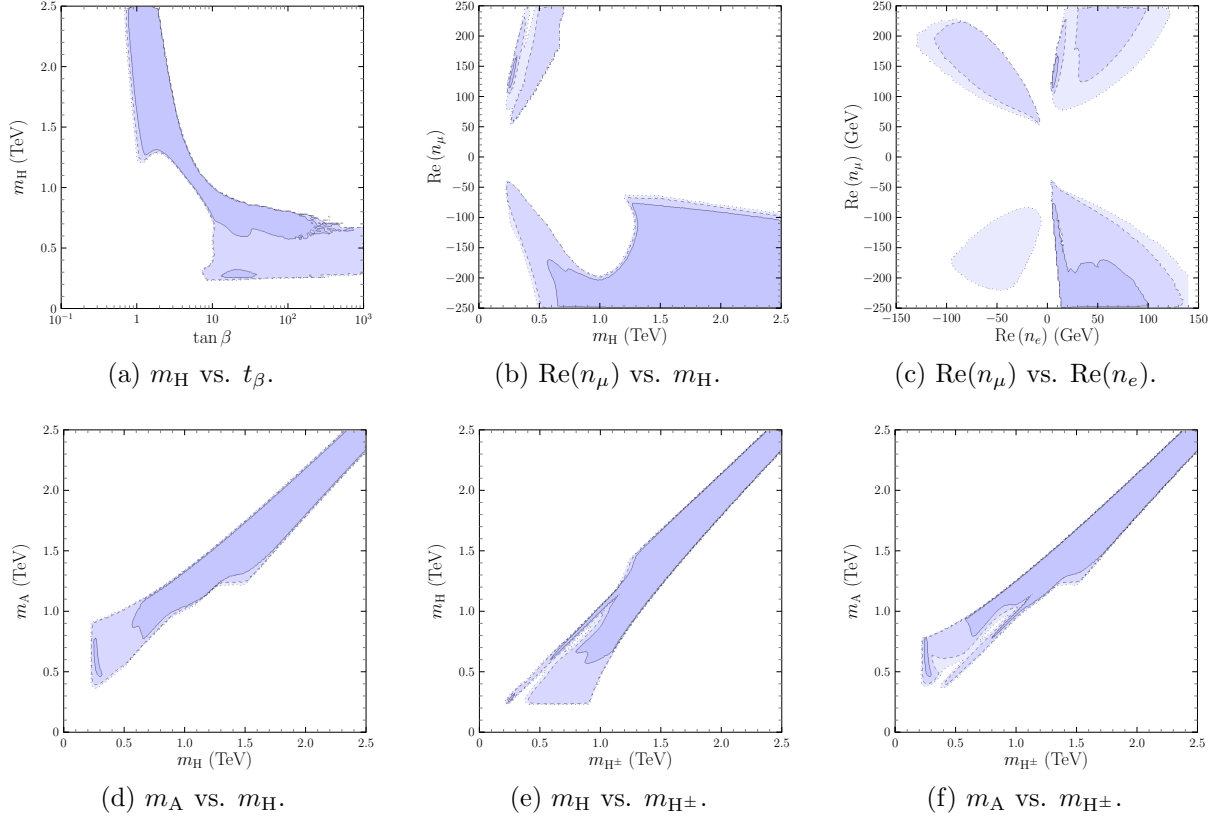


Figure 1: Illustrative plots of the allowed parameter space where the δa_ℓ anomalies are reproduced.

In fig.1a one can roughly distinguish two types of solutions: (i) all scalar masses above 1.2 TeV and the ratio of the two vevs $t_\beta \sim 1$, and (ii) all new scalars masses in the $[0.2;1.2]$ TeV range and $t_\beta > 10$.

In the low mass solution, the muon anomaly is explained at one loop through the H contribution and thus $\text{Re}(n_\mu)$ can appear with both signs, as fig.1b illustrates. Instead, for heavy new scalars, the muon anomaly receives dominant two loop contributions in such a way that the muon coupling is fixed to be negative. On the other hand, the electron anomaly must be explained at two loops in the whole range of scalar masses when considering the previous constraints. In particular, the latter implies the existence of a linear relation between both lepton couplings given by $\text{Re}(n_\mu) \simeq -13\text{Re}(n_e)$, as can be seen in the lower part of fig.1c inside the darkest region: departure from this straight line introduces an important one loop contribution to the muon anomaly lowering also the scalar mass ranges. Finally, from figs.1d–1f, it is easy to check that all new scalars are degenerate in the heavy mass regime, with mass differences not exceeding 200 GeV; while, in the low mass region, the pseudoscalar is heavier than the scalar and the charged scalar is degenerate with either the scalar or the pseudoscalar.

4.1 Different scenarios for δa_e

So far we have focused on the value of the electron anomaly related to the Cs recoil measurements of the fine structure constant. This scenario is more challenging from the theoretical point of view due to the opposite sign of both leptonic anomalies. Nevertheless, in order to have a complete picture, we have performed the analyses taking into account the Rb case and also an average scenario combining these two results, namely $\delta a_e^{\text{Exp,Avg}} = -(2.0 \pm 2.2) \times 10^{-13}$. Although $\delta a_e^{\text{Exp,Cs}}$ and $\delta a_e^{\text{Exp,Rb}}$ are rather incompatible, this average value might be interesting to analyze since it has also negative sign, i.e. opposite to the muon anomaly, but it is roughly 4 times smaller than the Cs value.

The final results show that the main difference among the analyses is the change of sign of the electron coupling depending on the case, as can be checked in fig.2. There are also changes concerning the extension of the allowed regions, but the main features of our solutions still apply.

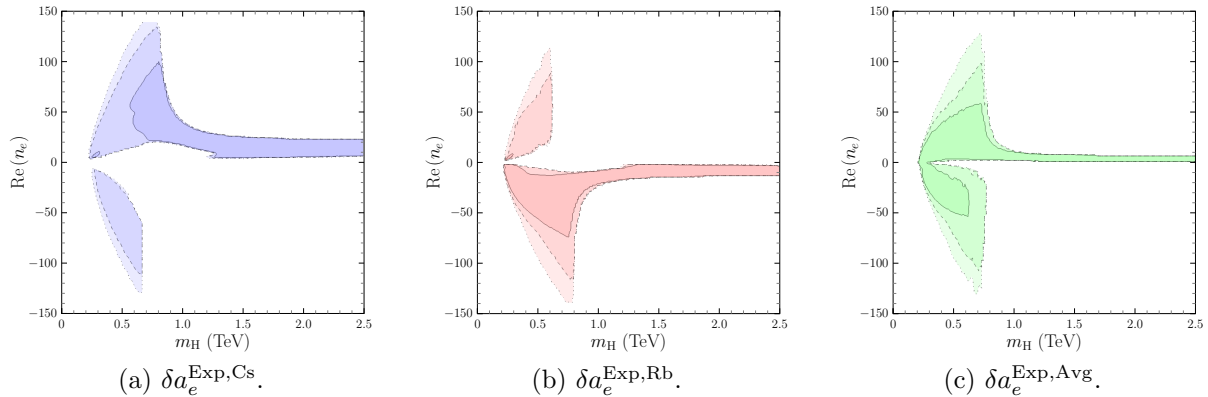


Figure 2: $\text{Re}(n_e)$ vs. m_H in the different scenarios considered for δa_e^{Exp} .

4.2 The CDF W boson mass anomaly

The recent measurement of the W boson mass reported by the CDF Collaboration ⁷⁾ can also be addressed in this framework through deviations in the oblique parameters $(\Delta S, \Delta T) \neq (0, 0)$. In particular, we consider two scenarios: (i) a “conservative” average between the CDF value and previous measurements

of the W mass, and (ii) only using the CDF result. In this section, the analyses are performed using the value of the electron anomaly arising from Cs recoil, that is, $\delta a_e^{\text{Exp,Cs}}$.

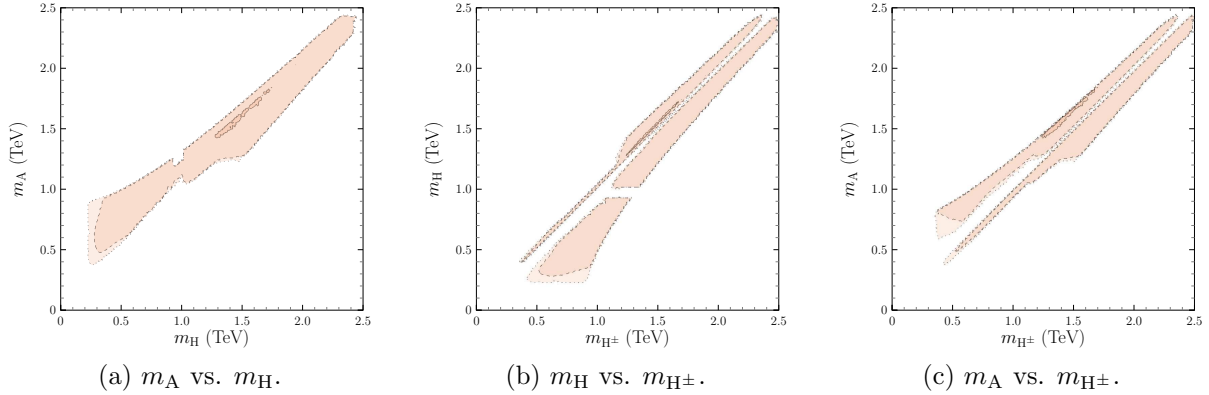


Figure 3: *Correlations involving the scalar masses in the “conservative” average scenario.*

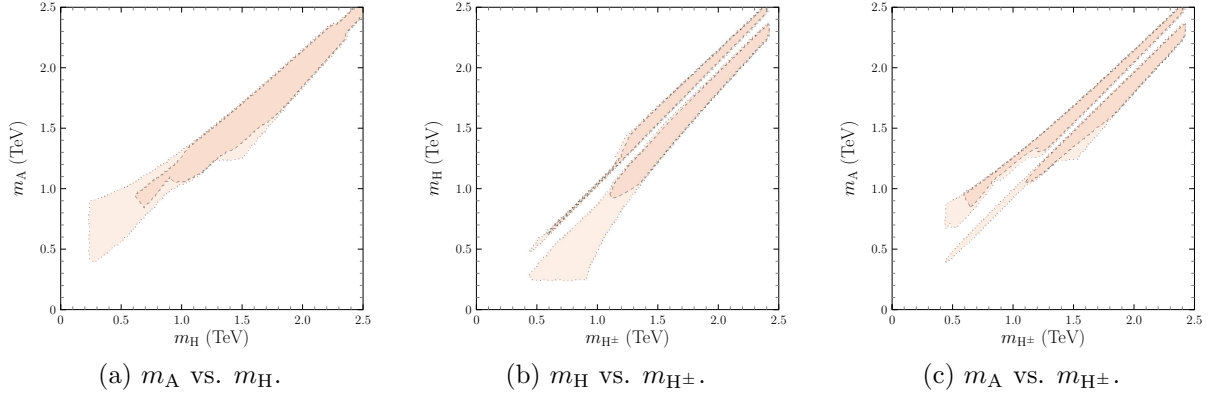


Figure 4: *Correlations involving the scalar masses in the scenario that only uses the CDF result.*

Figs.3 and 4 show the correlations among the scalar masses in these two scenarios. As one can easily check, scalar masses larger than 2 TeV are more difficult to obtain and near degeneracies $m_{H^\pm} \simeq m_H$ and $m_{H^\pm} \simeq m_{H^\pm}$ are absent. In fact, overall agreement with the previous constraints is worse in several regions of the parameter space, specially in the second scenario. Despite these changes, the main features of our solutions, previously mentioned, remain unchanged.

5 Summary

We present a particular Two-Higgs-Doublet Model, type I (or X) in the quark sector and general Flavor Conserving in the lepton sector, that is stable under one loop RGE and allows for LFU violation beyond the mass proportionality. This framework provides a simultaneous explanation of both $(g-2)_{\mu,e}$ anomalies in two possible regimes: (i) scalar masses in the [0.2;1.2] TeV range with $t_\beta \gg 1$, or (ii) scalar masses above 1.2 TeV and $t_\beta \sim 1$. The electron anomaly is explained through two loop Barr-Zee contributions in the whole range of scalar masses, while the muon anomaly also receives important one loop contributions

in the low mass region. Different assumptions concerning the value of the electron anomaly are fully considered. Furthermore, the CDF W boson anomaly can also be accommodated in this context.

Acknowledgements

CM is funded by *Conselleria de Innovación, Universidades, Ciencia y Sociedad Digital* from *Generalitat Valenciana* under grant ACIF/2021/284. CM acknowledges the organizers of the XX LNF Summer School ‘Bruno Touschek’ for the opportunity to present this work.

References

1. Muon $g - 2$ Collaboration, Phys. Rev. Lett. **126**, 14 (2021).
2. S. Borsanyi *et al*, Nature **593**, 51 (2021).
3. R.H. Parker *et al*, Science **360**, 191 (2018).
4. L. Morel *et al*, Nature **588**, 61 (2020).
5. F.J. Botella *et al*, Phys. Rev. D **102**, 3 (2020).
6. F.J. Botella *et al*, arXiv:2205.01115.
7. CDF Collaboration, Science **376**, 170 (2022).
8. F.J. Botella *et al*, Phys. Rev. D **98**, 3 (2018).
9. I.F. Ginzburg *et al*, Phys. Rev. D **72**, 11 (2005).
10. I.P. Ivanov *et al*, Phys. Rev. D **92**, 5 (2015).
11. ATLAS Collaboration, Eur. Phys. J. C **81**, 6 (2021).
12. ATLAS Collaboration, Eur. Phys. J. C **81**, 2 (2021).
13. ATLAS Collaboration, ATLAS-CONF-2020-058 (2020).
14. ATLAS Collaboration, ATLAS-CONF-2020-026 (2020).
15. ATLAS Collaboration, Phys. Lett. B **812**, (2021).
16. ATLAS Collaboration, ATLAS-CONF-2020-027 (2020).
17. ATLAS Collaboration, Phys. Lett. B **798**, (2019).
18. ATLAS Collaboration, Eur. Phys. J. C **80**, 10 (2020). [Erratum: Eur. Phys. J. C **81**, 29 (2021), Eur. Phys. J. C **81**, 398 (2021)].
19. CMS Collaboration, CMS-PAS-HIG-16-003 (2016).
20. CMS Collaboration, CMS-PAS-HIG-19-005 (2020).
21. CMS Collaboration, JHEP **01**, 148 (2021).
22. CMS Collaboration, JHEP **07**, 027 (2021).

23. CMS Collaboration, Eur. Phys. J. C **81**, 6 (2021).
24. P.A. Zyla *et al*, Review of Particle Physics, PTEP **2020**, 8 (2020).
25. W. Grimus *et al*, Nucl. Phys. B **801**, 81 (2008).
26. ALEPH Collaboration, Eur. Phys. J. C **49**, 411 (2007).
27. ATLAS Collaboration, JHEP **10**, 182 (2017).
28. CMS Collaboration, Phys. Lett. B **798**, (2019).
29. ATLAS Collaboration, JHEP **01**, 055 (2018).
30. CMS Collaboration, JHEP **02**, 048 (2017).
31. CMS Collaboration, JHEP **09**, 007 (2018).
32. ATLAS Collaboration, JHEP **11**, 085 (2018).
33. CMS Collaboration, JHEP **07**, 142 (2019).
34. CMS Collaboration, JHEP **01**, 096 (2020).
35. CMS Collaboration, JHEP **07**, 126 (2020).
36. V. Cirigliano *et al*, Phys. Rev. Lett. **99**, 23 (2007).
37. A. Pich *et al*, Prog. Part. Nucl. Phys. **75**, 41 (2014).
38. M. Misiak *et al*, Phys. Rev. Lett. **98**, 2 (2007).
39. A. Crivellin *et al*, Phys. Rev. D **87**, 9 (2013).

MULTI-STEP PHASE TRANSITIONS AND GRAVITATIONAL WAVES IN THE INERT DOUBLET MODEL

Nico Benincasa

National Institute of Chemical Physics and Biophysics, R vala 10, Tallinn, Estonia

Luigi Delle Rose

Dipartimento di Fisica, Universit  della Calabria, I-87036 Arcavacata di Rende, Cosenza, Italy

Kristjan Kannike

National Institute of Chemical Physics and Biophysics, R vala 10, Tallinn, Estonia

Luca Marzola

National Institute of Chemical Physics and Biophysics, R vala 10, Tallinn, Estonia

Abstract

The inert doublet model is a well-motivated extension of the Standard Model that contains a dark matter candidate and modifies the dynamics of the electroweak symmetry breaking. In order to detail its phenomenology, we perform a comprehensive study of cosmic phase transitions and gravitational wave signals implied by the framework, accounting for the latest results of collider experiments. We require the neutral inert scalar to constitute, at least, a subdominant part of the observed dark matter abundance. While most of the phase transitions proceed through a single step, we identify regions of the parameter space where the electroweak vacuum is reached after multiple phase transitions. The resulting gravitational wave spectrum is generally dominated by single-step transitions and, in part of the parameter space, falls within the reach of near-future gravitational wave detectors such as LISA or BBO. We find that direct detection experiments efficiently probe the part of parameter space associated with multi-step phase transitions, which remain unconstrained only in the Higgs resonance region.

1 Introduction

Although the discovery of the Higgs boson at the LHC ^{16, 2)} brought to completion the search for Standard Model (SM) particles, we are far from having a complete description of Nature. The cosmological observations of the last thirty years, for instance, have revealed that the SM constituents explain only a small share of the total energy budget of the Universe. In particular, the analysis of the microwave radiation background shows that baryons constitute only about 15% of all matter ³⁾. The remaining part is accounted for by dark matter (DM), a substance of unknown nature which finds no description in the SM. Presently, the leading direct detection experiments have not yet found clear signals of DM scattering on nucleons or electrons, resulting in upper bounds on the direct detection cross sections ^{4, 7, 35)}. Similarly, this far collider searches have not found any presence of DM particles in the produced states ¹⁾.

This lack of signals gives encouragement to look for other avenues in the attempt to pinpoint the possible physics beyond the SM. In the present paper we revisit the phenomenology of the Inert Doublet Model (IDM) (23, 34, 10, 31), paying special attention to the reach of future gravitational-wave (GW) experiments.

With the present paper, we intend to improve on existing analyses pertaining to cosmic phase transitions (PT) within the IDM. To this purpose, we analyze the parameter space allowed by the latest collider and DM searches in the attempt to map the available phase transition patterns, as well as the GW signals they produce. Although most commonly the EW phase transitions occur in a single step ($O \rightarrow h$), we find regions of the parameter space where two-step ($O \rightarrow H \rightarrow h$ or $O \rightarrow hH \rightarrow h$) and even three-step ($O \rightarrow H \rightarrow hH \rightarrow h$) transitions are realised. We pay particular attention to two- and three-step processes that involve multiple first-order phase transitions, which have the potential to generate a clear GW signature presenting multiple peaks in the spectrum.

2 The inert doublet model

2.1 Tree-level potential

The SM Higgs doublet H_1 and the inert doublet H_2 can be decomposed as

$$H_1 = \begin{pmatrix} G^+ \\ \frac{v+h+iG^0}{\sqrt{2}} \end{pmatrix}, \quad H_2 = \begin{pmatrix} H^+ \\ \frac{H+iA}{\sqrt{2}} \end{pmatrix}, \quad (1)$$

where h is the SM Higgs boson, $\langle h \rangle = v = 246.22$ GeV is the electroweak (EW) vacuum expectation value (VEV) and G^+ and G^0 are Goldstone bosons. The inert doublet comprises a charged scalar field H^\pm , and two neutral scalars, H and A , with opposite CP-parities.

The tree-level potential of the model,

$$V = -m_1^2 |H_1|^2 - m_2^2 |H_2|^2 + \lambda_1 |H_1|^4 + \lambda_2 |H_2|^4 + \lambda_3 |H_1|^2 |H_2|^2 + \lambda_4 |H_1^\dagger H_2|^2 + \frac{\lambda_5}{2} [(H_1^\dagger H_2)^2 + \text{h.c.}], \quad (2)$$

respects a discrete \mathbb{Z}_2 symmetry under which H_2 is odd and all the SM fields are even. The symmetry thus ensures the stability of the lightest component of the inert doublet and forbids new Yukawa couplings between H_2 and the SM fermions, hence the epithet *inert*.

The requirement that the tree-level potential be minimised at the EW vacuum leads to the following parametrization

$$\begin{aligned} m_1^2 &= \frac{m_h^2}{2}, & m_2^2 &= -m_H^2 + \lambda_{345} \frac{v^2}{2}, & \lambda_1 &= \frac{m_h^2}{2v^2}, & \lambda_3 &= \lambda_{345} + 2 \frac{m_{H^\pm}^2 - m_H^2}{v^2}, \\ \lambda_4 &= \frac{m_H^2 + m_A^2 - 2m_{H^\pm}^2}{v^2}, & \lambda_5 &= \frac{m_H^2 - m_A^2}{v^2}, \end{aligned} \quad (3)$$

given in terms of the tree-level scalar mass matrix eigenvalues m_h^2, m_H^2, m_A^2 and $m_{H^\pm}^2$ ($m_{G^0} = m_{G^\pm} = 0$ at tree-level in the EW vacuum).

The inert doublet self-coupling λ_2 does not affect DM phenomenology, but can influence the phase structure of the potential by inducing new minima at non-zero temperature. With the parametrization in eq. (3), the model is completely specified by the quantities $\lambda_2, \lambda_{345} \equiv \lambda_3 + \lambda_4 + \lambda_5$, and the masses m_H, m_{H^\pm}, m_A , which we use as input parameters in our analysis. The lightest neutral components of H_2 is a viable DM candidate. In our analysis, this role is assigned to H , in effect choosing $\lambda_5 < 0$. Equivalently,

A could be the DM candidate, related to our case through the substitutions $\lambda_{345} \leftrightarrow \tilde{\lambda}_{345} = \lambda_3 + \lambda_4 - \lambda_5$ and $m_H \leftrightarrow m_A$.¹

For the treatment of the phase transitions in sec.4.1, we suppose that excursions in the field space occur only in the (h, H) plane, while the remaining scalar degrees of freedom are prevented from acquiring a VEV at any temperature. Therefore, the terms in the tree-level potential relevant for this analysis are

$$V_0(h, H) = -\frac{m_1^2}{2}h^2 + \frac{\lambda_1}{4}h^4 - \frac{m_2^2}{2}H^2 + \frac{\lambda_2}{4}H^4 + \frac{\lambda_{345}}{4}h^2H^2. \quad (4)$$

2.2 Coleman-Weinberg correction to the potential

The tree-level potential in eq. (2) receives important radiative contributions sourced by the one-loop n -point functions, resummed in the Coleman-Weinberg correction¹⁹⁾

$$V_{\text{CW}}(h, H) = \frac{1}{64\pi^2} \sum_i n_i m_i^4 \left(\ln \frac{m_i^2}{\mu^2} - C_i \right), \quad (5)$$

where $i = W, Z, t, h, H, G^0, A, G^\pm, H^\pm$ (as customary, we retain only the dominant fermion contribution given by the top quark), m_i are the eigenvalues of the field-dependent masses, μ is the renormalization scale (which we set to $\mu = v$) and C_i are constants peculiar to the renormalization scheme. The bosonic and fermionic contributions are weighted by the coefficients n_i given by $n_W = 6$, $n_Z = 3$, $n_t = -12$, $n_h = n_H = n_{G^0} = n_A = 1$ and $n_{H^\pm} = n_{G^\pm} = 2$ ²²⁾. After using dimensional regularization with the $\overline{\text{MS}}$ subtraction scheme, we have $C_i = \frac{3}{2}$ for scalars, fermions and longitudinal vector bosons, as well as $C_i = \frac{1}{2}$ for transverse vector bosons.

Following previous analyses^{18, 17, 25)}, we compensate possible radiative shifts of the EW VEV and masses, and address the problematic Goldstone contributions with a set of counterterms specified in

$$V_{\text{CT}}(h, H) = \delta m_h^2 h^2 + \delta m_H^2 H^2 + \delta \lambda_1 h^4, \quad (6)$$

2.3 Finite temperature effects

At finite temperature, thermal corrections result in a further contribution²⁴⁾,

$$V_{\text{T}}(h, H, T) = \frac{T^4}{2\pi} \left[\sum_i n_i^{\text{B}} J_{\text{B}} \left(\frac{m_i^2}{T^2} \right) + \sum_i n_i^{\text{F}} J_{\text{F}} \left(\frac{m_i^2}{T^2} \right) \right], \quad (7)$$

to the scalar potential. The two sums are over the boson and fermion degrees of freedom, respectively and the corresponding thermal functions⁶⁾ are

$$J_{\text{B/F}}(x) = \int_0^\infty dt t^2 \ln \left(1 \mp e^{-\sqrt{t^2+x}} \right). \quad (8)$$

A consistent treatment of thermal corrections also requires the resummation of the leading self-energy daisy diagrams, which shifts the field-dependent masses

$$m_i^2(T) = m_i^2 + c_i T^2, \quad (9)$$

¹In regard of this, notice that $\lambda_5 \rightarrow -\lambda_5$ under the substitution $m_H \leftrightarrow m_A$ and that the quartic couplings determining the DM abundance via hHH or hAA interactions are, respectively, by λ_{345} and $\tilde{\lambda}_{345}$.

by a thermal contribution quantified in the coefficients c_i 28, 36, 14)

In our analysis we use the above thermal masses when computing the quantum and the finite-temperature corrections to the tree-level potential. The full thermally-corrected effective potential is thus

$$V_{\text{eff}}(h, H, T) = V_0(h, H) + V_{\text{CW}}(h, H, T) + V_{\text{CT}}(h, H) + V_{\text{T}}(h, H, T). \quad (10)$$

3 Constraints

With the full expression of the scalar potential at hand, we briefly review the constraints applied in the forthcoming analysis.

3.1 Theoretical constraints

A first requirement is the stability of the scalar potential, which guarantees that minima appear at finite field values. For the IDM, the potential is bounded from below if the following conditions are satisfied:

$$\lambda_1 > 0, \quad \lambda_3 + 2\sqrt{\lambda_1\lambda_2} > 0, \quad \lambda_3 + \lambda_4 - |\lambda_5| + 2\sqrt{\lambda_1\lambda_2} > 0. \quad (11)$$

A charge-breaking vacuum is avoided by $\lambda_4 - |\lambda_5| < 0$, which always holds if H^\pm is heavier than the DM candidate H 26).

Perturbative unitarity requires that the combinations of couplings e_i from the eigenvalues of the two-to-two scattering matrix be bounded: $|e_i| < 8\pi$. From the full 22×22 S -matrix 8), we have 13) $e_{1,2} = \lambda_3 \pm \lambda_4$, $e_{3,4} = \lambda_3 \pm \lambda_5$, $e_{5,6} = \lambda_3 + 2\lambda_4 \pm 3\lambda_5$, $e_{7,8} = -\lambda_1 - \lambda_2 \pm \sqrt{(\lambda_1 - \lambda_2)^2 + \lambda_4^2}$, $e_{9,10} = -3\lambda_1 - 3\lambda_2 \pm \sqrt{9(\lambda_1 - \lambda_2)^2 + (2\lambda_3 + \lambda_4)^2}$, $e_{11,12} = -\lambda_1 - \lambda_2 \pm \sqrt{(\lambda_1 - \lambda_2)^2 + \lambda_5^2}$. The strongest constraints are given by $|\lambda_2| < 4\pi/3$ and $|\lambda_{345}| < 4\pi$.

3.2 Experimental constraints

The decay widths of the Z and W bosons measured at LEP with high precision preclude decays of these particles into the new states. Therefore, we require that the masses of the inert doublet components satisfy 15)

$$m_H + m_{H^\pm} > m_W, \quad m_A + m_{H^\pm} > m_W, \quad m_H + m_A > m_Z, \quad 2m_{H^\pm} > m_Z. \quad (12)$$

LEP searches for new neutral final states further exclude a range of masses 33), thereby forcing

$$m_H > 80 \text{ GeV}, \quad m_A > 100 \text{ GeV} \quad \text{or} \quad m_A - m_H < 8 \text{ GeV}, \quad (13)$$

in addition to

$$m_{H^\pm} > 70 \text{ GeV} \quad (14)$$

due to searches for charged scalar pair production 39).

Similarly, if $m_H < m_h/2$, the Higgs boson can decay into DM with a partial width of

$$\Gamma_{h \rightarrow HH} = \frac{\lambda_{345}^2 v^2}{32\pi m_h} \sqrt{1 - \frac{4m_H^2}{m_h^2}} \quad (15)$$

which is constrained by measurements of the Higgs boson invisible width. The current values provided by the ATLAS and CMS experiments 9, 30) on the invisible branching ratio $\text{BR}_{\text{inv}} = \Gamma_{h \rightarrow HH} / (\Gamma_{h \rightarrow \text{SM}} + \Gamma_{h \rightarrow HH})$ are $\text{BR}_{\text{inv}} < 0.23 - 0.36$. In the following, we will use the conservative limit $\text{BR}_{\text{inv}} < 0.23$.

Collider analyses also provide constraints on the electroweak precision observables (EWPO), sensitive to new radiative contributions in the electroweak sector. The EWPO are usually expressed via the Peskin-Takeuchi parameters S , T and U ^{37, 38)}, determined through a joint fit of the precision observables and SM predictions. The EWPO fit within the SM alone ³²⁾ gives the results presented in tab. 1.

Parameter	Result	Correlation
S	0.06 ± 0.10	$0.90 (T), -0.57 (U)$
T	0.11 ± 0.12	$-0.82 (U)$
U	-0.02 ± 0.09	

Table 1: Peskin-Takeuchi parameters ^{37, 38)} as determined by the electroweak precision observables ³²⁾.

The IDM contributions to the S , T and U parameters, which add to the SM result, are given by ²⁷⁾

In the IDM new EWPO contributions vanish in the limit of degenerate masses, so these observables tend to discourage hierarchical mass spectra. For the purpose of constraining the IDM parameter space, we require that the total values of S , T and U remain within the 95% joint confidence level.

Finally, the properties of our DM candidate are constrained by the latest Planck measurements, which gives the corresponding relic density as $\Omega_c h^2 = 0.120 \pm 0.001$ ³⁾. In our analysis we impose the 3σ upper bound indicated by the data, although we allow for the possibility that the inert doublet yield only a subdominant DM component. For the computation of the relic abundance we rely on the micrOMEGAS code ¹²⁾.

4 Results

In our analysis, we scan the parameter space shown in tab. 2. We then use the CosmoTransitions package ⁴²⁾ to obtain, for each point selected, the temperature-dependent phase structure of the scalar potential and to assess the nature of the corresponding phase transitions.

Parameter	Range
m_H	[10, 1000] GeV
m_A	[10, 1000] GeV
m_{H^+}	[10, 1000] GeV
λ_2	$[0, \frac{4\pi}{3}]$
λ_{345}	$[-1.47, 4\pi]$

Table 2: The parameter ranges used in our scan. We selected only configurations with $m_H < m_A$, since H is our DM candidate. The lower bound on λ_{345} is imposed by the stability of the potential ¹³⁾.

The obtained points are then selected according to the bounds discussed above.

4.1 Phase transition

The PT patterns found in our analysis are summarised in fig. 1, which schematically shows the sequences of transitions that connect the high-temperature minimum of the IDM potential, O , to the EW vacuum phase h . The red arrow indicates one-step PTs $O \rightarrow h$, which directly connect the two minima. The blue arrows characterise two-step PTs $O \rightarrow H \rightarrow h$, in which the EW vacuum is reached after a transient phase, H , where only the inert doublet neutral component acquires a VEV. Similarly, the yellow arrows denote two-step PT patterns $O \rightarrow Hh \rightarrow h$ going through a different transient phase, Hh , in which

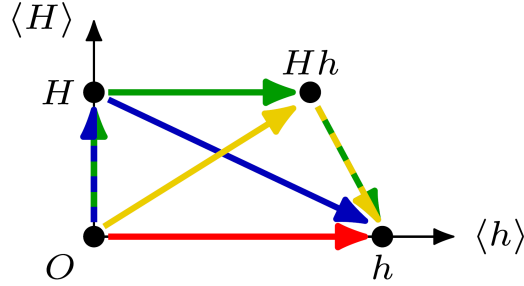


Figure 1: Schematic representation of the possible phases and PT patterns supported by the IDM scalar potential. The high-temperature minimum of the potential, where $\langle h \rangle = \langle H \rangle = 0$, is denoted with O . The phase h is characterised by $\langle h \rangle \neq 0$ and $\langle H \rangle = 0$, and includes the EW vacuum. The configuration where $\langle H \rangle \neq 0$ but $\langle h \rangle = 0$ is denoted with H , while a phase with $\langle h \rangle, \langle H \rangle \neq 0$ is indicated with Hh . The arrows show the different PT sequences identified in our analysis.

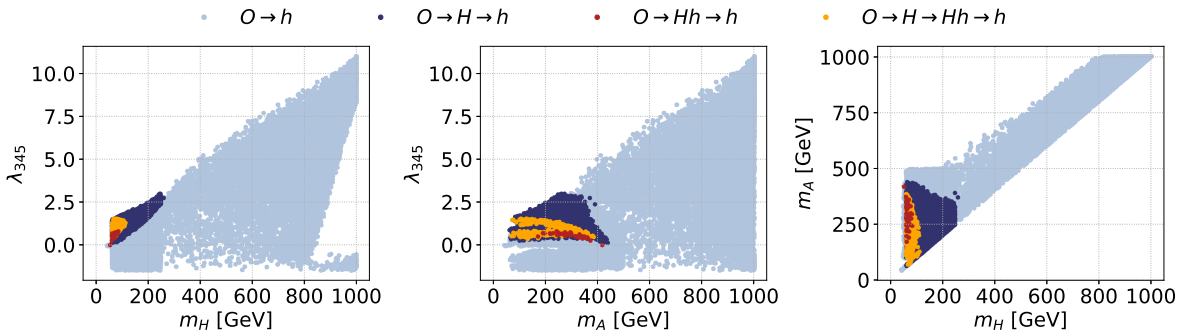


Figure 2: Projections of the IDM parameter space on the planes spanned by m_H , m_A and λ_{345} . Each panel shows the regions yielding a one-step PT $O \rightarrow h$ (light blue), a two-step PT $O \rightarrow H \rightarrow h$ (dark blue) and $O \rightarrow Hh \rightarrow h$ (red), as well as a three-step PT $O \rightarrow H \rightarrow Hh \rightarrow h$ (orange). For all these transitions, we require at least one FOPT. Points leading to DM overabundance are not shown.

both h and H acquire non-vanishing thermal VEVs. In our scan we have also identified three-step PTs $O \rightarrow H \rightarrow Hh \rightarrow h$ as indicated by the green arrows.

The sequences of PTs involving at least one first-order phase-transition (FOPT) step are presented in isolation in fig. 2. As we can see, most of the covered parameter space gives rise to one-step $O \rightarrow h$, whereas multi-step PTs only occur in a limited region roughly bounded by $0 \lesssim \lambda_{345} \lesssim 3$, $m_H \lesssim 250$ GeV and $m_A, m_{H^+} < 500$ GeV, which we scan with greater accuracy. In particular, we find that three-step PTs require $\lambda_{345} \lesssim 1.5$, while two-step PTs using a transient Hh phase are allowed only for $\lambda_{345} \lesssim 0.8$.

4.2 Direct detection

Before proceeding with the analysis of the resulting GW signal, we consider a further bound given by the direct detection experiments, which probe the spin-independent cross section of DM on nuclei. To this purpose, we show in fig. 3 the obtained spin-independent scattering cross section σ_{SI} as function of the

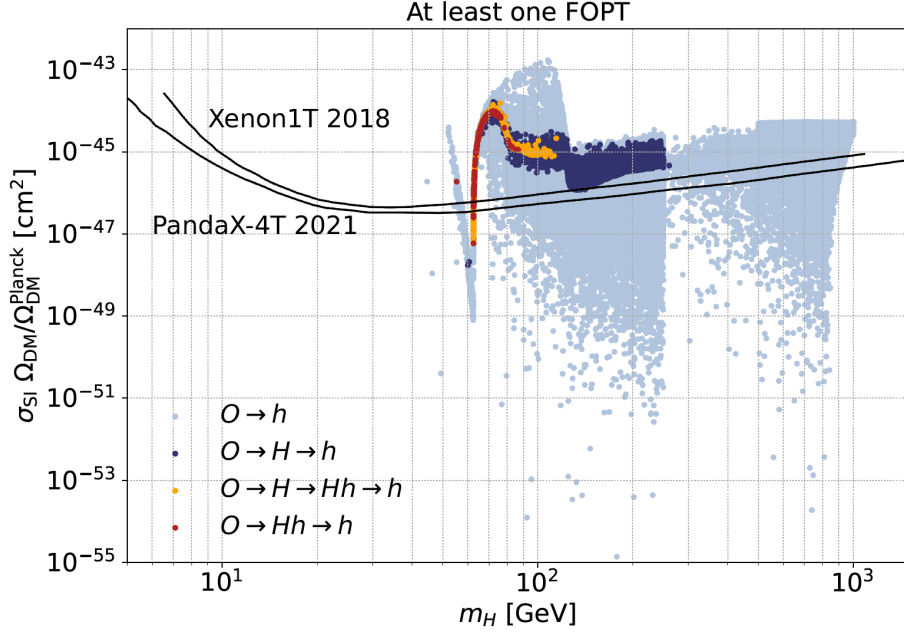


Figure 3: Spin-independent direct-detection cross section as function of the DM mass for transition patterns involving at least one FOPT. The colour code highlights the pattern type: one-step PT $O \rightarrow h$ (light blue), two-step PT $O \rightarrow H \rightarrow h$ (dark blue) and $O \rightarrow Hh \rightarrow h$ (red), as well as a three-step PT $O \rightarrow H \rightarrow Hh \rightarrow h$ (orange). The experimental bounds are taken from refs. ^{7, 35}). Points leading to DM overabundance are not shown.

DM mass, highlighting the different transition pattern identified. The analysis is presented for processes involving at least one FOPT. Because we allow for DM under-abundances, the plot has been obtained by re-scaling the cross section with the fraction $\Omega_{DM}/\Omega_{DM}^{Planck}$, where Ω_{DM} is the DM abundance produced by the IDM and Ω_{DM}^{Planck} the value given by the latest Planck measurement ³). The indicated experimental bounds use the 2018 release of the XENON1T data ⁷) and the 2021 PandaX-4T result ³⁵).

As we can see, most of the multi-step PTs fall above of the considered exclusion bounds. These processes may still occur near the Higgs resonance region ($m_H \simeq m_h/2$), where resonance effects allow for the lower values of the λ_{345} coupling required by these solutions. Another region of interest is for $m_H \in [120, 160]$ GeV, resulting in a signal borderline with the current exclusions for processes involving at least one FOPT. Contrary to the Higgs resonance region, these solutions select only multi-step PTs following the pattern $O \rightarrow H \rightarrow h$ and yield underabundant DM.

4.3 Gravitational wave

The GW signals supported by the IDM parameter space are shown in fig. 4, where we depict the value of the the peak of the power spectrum $h^2 \Omega_{GW}^{peak}$ and the associated frequency at this peak f^{peak} for each point of scan performed.

The obtained GW signals are always dominated by the sound wave contribution. We also display the sensitivity curves of near future GW detectors LISA ^{40, 5}), BBO ^{20, 21}) and DECIGO ^{41, 29}). LISA, in particular, will probe mostly one-step transitions $O \rightarrow h$ and part of the solutions using the

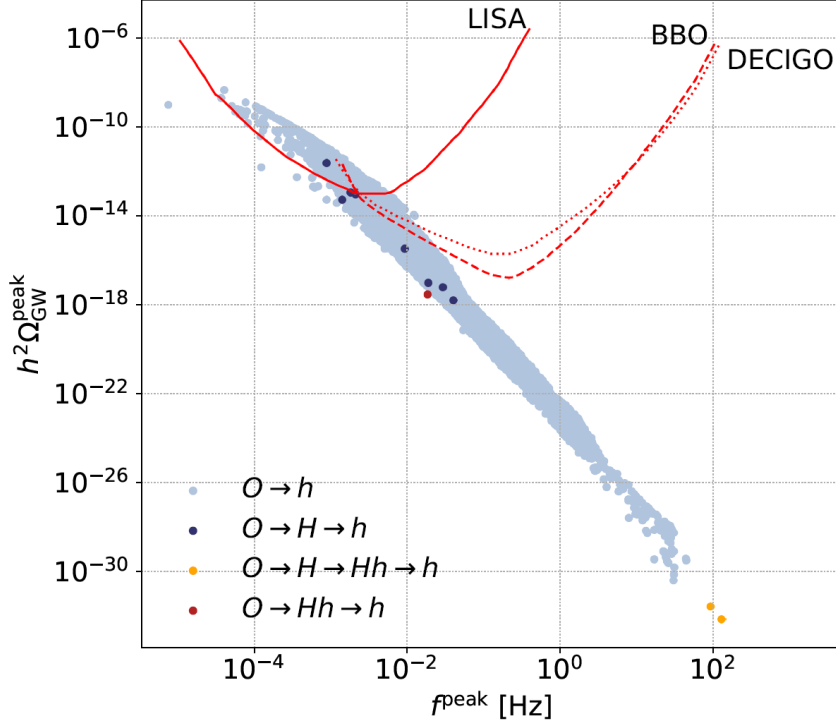


Figure 4: GW signal $h^2 \Omega_{\text{GW}}^{\text{peak}}$ as a function of the frequency f for the considered parameter space. The colour code indicates the PT pattern. Points leading to DM overabundance and excluded by Xenon1T are not shown.

$O \rightarrow H \rightarrow h$ pattern. Overall, we see that single-step PTs tend to produce stronger signals. Finally, no points yielding a detectable GW signal by LISA, BBO or DECIGO, while satisfying Planck relic density constraint were found.

5 Conclusion

With the present paper we intended to address a thorough study of the cosmic phase transitions as well as the implied gravitational wave signals, with a comprehensive exploration of the phase structure and possible transitions supported by the inert doublet model. In our work we took into account available collider constraints, electroweak precision observables and theoretical bounds imposed by stability of the potential and perturbativity. Furthermore, the latest results of dark matter experiments have been used to investigate the properties of the neutral scalar component of the inert doublet, assumed to provide at least a subdominant dark matter component.

Our study of the thermal evolution of the scalar potential has given a full characterization of the possible phase transition patterns supported by the inert doublet model (see fig. 1). Although in most of the parameter space the electroweak vacuum is reached through a single phase transition, our analysis shows well-defined parameter regions where the electroweak vacuum is reached via a chain of consecutive phase transitions. Both two-step and three-step phase transitions with different transient phases (where only the inert doublet or both the doublets acquire a vacuum expectation value) are possible. Multi-step

transitions can occur when the inert doublet components are not heavier than a few hundred GeV and couplings have moderate values, as shown in fig. 2 for patterns involving at least one first-order step.

By cross-correlating the identified phase transition patterns with dark matter phenomenology, we find that the inert doublet model can explain the observed relic abundance only in a part of its parameter space where the electroweak vacuum is reached through single-step processes of either order. Although multi-step phase transition patterns are associated with a significant dark matter underdensity, we see that dark matter direct detection experiments are able to tightly constrain these solutions. Focusing on patterns that involve at least one first-order phase transition, fig. 3 shows that the direct detection bounds allow for multi-step phase transitions almost exclusively for dark matter masses close to half the Higgs boson mass.

Finally, after applying the results of direct detection searches as a further constraint, we have investigated the gravitational wave spectra produced by different phase transition patterns. The results, gathered in fig. 4, show that one-step processes dominate the signal. Future gravitational wave experiments will probe a part of these solutions yielding a significant dark matter underdensity, implying that the detection of a compatible signal would require another dark matter component. Whereas few points with multiple first-order phase transitions fall above the sensitivity curves of the considered experiments, we find that the generated gravitational signal is always strongly dominated by the transitions initiated during the transient phase at intermediate temperature. Therefore, it is highly unlikely that such transitions will induce a gravitational wave signal with two separate distinguishable peaks at different frequencies.

Acknowledgements

This work was supported by the Estonian Research Council grants PRG434 and PRG356, by the European Regional Development Fund and the programme Mobilitas Plus grants MOBTT5 and MOBTT86, and by the EU through the European Regional Development Fund CoE program TK133 “The Dark Side of the Universe”. The work of LDR has been partially supported by a fellowship from “la Caixa” Foundation (ID 100010434) and from the European Union’s Horizon 2020 research and innovation programme under the Marie Skłodowska-Curie Action grant agreement No 847648.

References

1. ATLAS Collaboration, Constraining the Dark Sector with the monojet signature in the ATLAS experiment, in: ATL-PHYS-PUB-2021-020
2. G. Aad *et al*, Phys. Lett. B, 716:1-29 (2012).
3. N. Aghanim *et al*, Astron. Astrophys., 641:A6 (2020).
4. D. S. Akerib *et al*, Phys. Rev. Lett., 118(2):021303 (2017).
5. LISA Collaboration, Laser Interferometer Space Antenna, in: eprint arXiv:1702.00786
6. G. W. Anderson *et al*, Phys. Rev. D, 45:2685-2698 (1992).
7. E. Aprile *et al*, Phys. Rev. Lett., 121(11):111302 (2018).
8. A. Arhrib *et al*, Phys. Rev. D, 85:095021 (2012).

9. ATLAS collaboration, Combined measurements of Higgs boson production and decay using up to 139 fb^{-1} of proton-proton collision data at $\sqrt{s} = 13 \text{ TeV}$ collected with the ATLAS experiment, in: ATLAS-CONF-2021-053
10. R. Barbieri *et al*, Phys. Rev. D, 74:015007 (2006).
11. G. Belanger *et al*, Phys. Rev. D, 91:115011 (2015).
12. G. Belanger *et al*, Eur. Phys. J. C 81(3):239 (2021).
13. A. Belyaev *et al*, Phys. Rev. D, 97(3):035011 (2018).
14. J. Bernon *et al*, JHEP, 05:151 (2018).
15. Q. H. Cao *et al*, Phys. Rev. D, 76:095011 (2007).
16. S. Chatrchyan *et al*, Phys. Lett. B, 716:30-61 (2012).
17. J. M. Cline *et al*, JHEP, 11:089 (2011).
18. J. M. Cline *et al*, Phys. Rev. D, 55:3873-3881 (1997).
19. S. R. Coleman *et al*, Phys. Rev. D, 7:1888-1910 (1973).
20. V. Corbin *et al*, Class. Quant. Grav., 23:2435-2446 (2006).
21. J. Crowder *et al*, Phys. Rev. D, 72:083005 (2005).
22. C. Delaunay *et al*, JHEP, 04:029 (2008).
23. N. G. Deshpande *et al*, Phys. Rev. D, 18:2574 (1978).
24. L. Dolan *et al*, Phys. Rev. D, 9:3320-3341 (1974).
25. S. Fabian *et al*, JCAP, 09:011 (2021).
26. I. F. Ginzburg *et al*, Phys. Rev. D, 82:123533 (2010).
27. W. Grimus *et al*, Nucl. Phys. B, 801:81-96 (2008).
28. D. J. Gross *et al*, Rev. Mod. Phys., 53:43-80 (1981).
29. S. Kawamura *et al*, PTEP, 2021(5):05A105 (2021).
30. V. Khachatryan *et al*, JHEP, 02:135 (2017).
31. L. L. Honorez *et al*, JCAP, 02:028 (2007).
32. C. T. Lu *et al*, Phys. Rev. D, 106:035034 (2022).
33. E. Lundstrom *et al*, Phys. Rev. D, 79:035013 (2009).
34. E. Ma, Phys. Rev. D, 73:077301 (2006).
35. Y. Meng *et al*, Phys. Rev. Lett., 127(26):261802 (2021).
36. R. R. Parwani *et al*, Phys. Rev. D, 45:4695-4705 (1992).

37. M. E. Peskin *et al*, Phys. Rev. Lett., 65:964-967 (1990).
38. M. E. Peskin *et al*, Phys. Rev. D, 46:381-409 (1992).
39. A. Pierce *et al*, JHEP, 08:026 (2007).
40. eLISA Collaboration *et al*, The Gravitational Universe, in: eprint arXiv:1305.5720
41. N. Seto *et al*, Phys. Rev. Lett., 87:221103 (2001).
42. C. L. Wainwright *et al*, Comput. Phys. Commun., 183:2006-2013 (2012).

COLOURING THE JETS AT LHC FOR Xbb TAGGER IMPROVEMENT

Giulia Manco

Università degli studi di Pavia and INFN, Sezione di Pavia

Abstract

After 10 years from its discovery, the Higgs boson is still one of the most investigated particles. The Higgs decay in two b -quarks is very interesting and the most probable decay, but, due to the large QCD background, it is not straightforward to study. For this reason, the LHC community is investing in the direction of Xbb taggers ($X=Z$ or Higgs boson), which aims at finding an optimal Higgs-tagger using jet substructure information. In this document, colour-sensitive variables will be studied as Xbb tagger, exploiting the different colour configuration of a colour-singlet and a colour-octet. Observable performances are tested on the $VHbb$ channel in the boosted limit.

1 Introduction

The Higgs boson was discovered in 2012 at LHC by the ATLAS and CMS Collaborations ¹⁾ ²⁾. Since then, the high energy physics community has been involved in the measurements of its properties. The Higgs boson gives the opportunity to test the Standard Model (SM) predictions and discover new physics. In particular, the coupling of the Higgs particle is the only interaction that can feel the difference between fermion generations.

At a Higgs boson mass of 125 GeV, the most probable decay is in two b quarks, with a branching ratio of about 58%. The direct measurement of the $b\bar{b}$ channel provides a test of the Yukawa coupling to a down-type quark and constrains the overall Higgs decay width. While this decay is the most frequent, it is a real experimental challenge to observe it. This is due to the overwhelming large QCD background that can mimic the signal signature. For these reasons it took six years until ATLAS and CMS obtained the necessary 5σ significance for the evidence of this decay channel ³⁾ ⁴⁾. The production mode used in these analyses is Higgs-boson (H) production in association with a vector boson V (W or Z), with V decaying

leptonically and the Higgs hadronically into a pair of b -quarks, which provides a clean experimental signature. The hard b -quarks produced by the Higgs boson decay are usually detected as two separate b -jets. When the momentum of the jets is higher than their invariant mass, the regime is called *boosted*. In such a situation, the two b -jets are close in angle and hence reconstructed as a single jet, also known as a large-radius jet.

In order to better discriminate the $H(b\bar{b})$ process over the production of b -jets from a gluon collinear splitting ($g \rightarrow b\bar{b}$), many strategies have been developed. Several jet substructure techniques have been designed, which aim at improving the discrimination performance by finding hard prongs inside the large-radius jet. Specifically, the different radiation pattern of signal and background can be exploited. In the signal case, the b -jets originate from a colour singlet and the radiation is more constrained inside the two b -quark system. In the background case, the radiation is more diffuse, due to the colour connection with the initial state, as shown in Figure 1.

In this paper, observables sensitive to the different colour configuration will be exploited, referring to this recent article ⁷⁾. The idea is build a tagger that can be applied to the decay products of a generic colour singlet X . In this regards, the Xbb tagger group in ATLAS aims at providing recommendations for $H \rightarrow b\bar{b}$ tagging and tools for its use within analysis. It is an activity which involves the investigation of both jet substructure and b -tagging performance in boosted $H \rightarrow b\bar{b}$ topologies ⁸⁾. The identified tagger with colour-sensitive variables is matter of interest of this group.

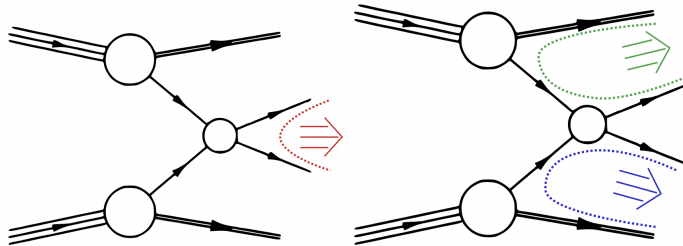


Figure 1: Possible colour connections for the signal on the left ($pp \rightarrow H \rightarrow b\bar{b}$) and for the background on the right ($pp \rightarrow g \rightarrow b\bar{b}$) ⁵⁾.

2 Observables

In the following, a selection of high-level colour-sensitive variables are presented. They were introduced in the literature in the past few years.

2.1 Jet Pull

Let us consider a hard jet J_a . The *pull vector* \vec{t} is the jet shape observable defined as: ⁵⁾

$$\vec{t} = \frac{1}{p_{T_a}} \sum_{i \in J_a} p_{T_i} |\vec{r}_i|^2 \hat{r}_i, \quad (1)$$

where p_{T_a} is the transverse momentum of the jet, and the sum runs over all the the jet constituents. y and ϕ represent rapidity and azimuthal angle and \vec{r}_i is the distance vector between the jet axis and its

i -th constituent in the y - ϕ plane

$$\vec{r}_i = (y_i - y_a, \phi_i - \phi_a). \quad (2)$$

The pull vector is sensitive to the different colour connections of the event and points toward the direction of emitted radiation.

We can introduce the projections of the pull vector along the direction between the two jets t_{\parallel} and in the perpendicular direction t_{\perp} (10, 11). We also consider the pull angle θ_p defined as (9):

$$\theta_p = \arccos \frac{t_{\parallel}}{|t|}. \quad (3)$$

2.2 Jet colour ring

The jet colour ring (11) is defined from the ratio of the squared matrix elements of signal and background, where the signal is considered as the decay of a colour singlet and the color octet is the background. In the soft-collinear limit approximation, such a ratio becomes:

$$\mathcal{O} = \frac{\Delta_{ak}^2 + \Delta_{bk}^2}{\Delta_{ab}^2}, \quad (4)$$

where Δ_{ij} are the distances between jets (or subjects) in the azimuth-rapidity plane, a is the leading jet, b the subleading jet and k a soft emission. The observable name originates from its geometric interpretation: radiation from colour singlets will tend to fall between the two jets, leading to values of $\mathcal{O} < 1$, while in the case of colour octets, one will tend to have $\mathcal{O} > 1$.

2.3 D_2

The variable D_2 (12) is defined as the ratio of two normalized N -point energy correlation functions (ECFs) (6), e_k^β :

$$D_2^{(\beta)} = \frac{e_3^{(\beta)}}{(e_2^{(\beta)})^3}. \quad (5)$$

β is a parameter which we have set to $\beta = 2$. The variable is usually calculated on a large radius jet, and is useful to discriminate 2-prong jets from 1-prong jets.

2.4 Lund jet plane

The Lund jet plane is defined in reference (13). It is formed by parsing backwards the Cambridge–Aachen (C/A) clustering history of the jet. The procedure starts by undoing the final clustering step and by recording the kinematics of the splitting. The primary Lund jet plane is obtained by iterating the above procedure, always following the hardest branching in each splitting and recording the azimuth-rapidity separation of the branchings involved in the splitting and the relative transverse momentum of the emission.

3 Observable performances on $VHbb$ channel

3.1 Event simulation and selection

In order to test the observable discrimination performance, 300k events for $pp \rightarrow H(b\bar{b})Z(\nu_\ell\bar{\nu}_\ell)$ signal and 4M events for the $pp \rightarrow b\bar{b}\nu_\ell\bar{\nu}_\ell$ background processes are generated. Number of events are chosen in order to have 50k events for both signal and background, accounting for the efficiency after applying

Table 1: *Percentage of events which pass the analysis selections.*

	Truth	Reco
Signal	20%	17%
Background	1.6%	1.3%

Table 2: *Area under the ROC curves for different combination of observables.*

	Truth	Reco
CS observables	0.826	0.788
D_2 +CR	0.817	0.787
LP _{CNN}	0.876	0.828
CS + LP _{CNN}	0.893	0.846

the selection cuts, shown in Table 1. Hard events are generated with `MG5_aMC@NLO v2.8.3.2` ¹⁴⁾ in a boosted regime and parton-level events are then showered in `Pythia v8.305` ¹⁵⁾. Detector effects are considered with a fast detector simulation of `Delphes v3.5.0` ¹⁶⁾. From `Delphes`, the Monte Carlo truth is extracted, containing the particle-level information. Reference ⁷⁾ gives a complete description of analysis selection and simulation used here.

3.2 Discrimination performance

In Fig. 2 the normalised distributions for eight colour sensitive variables (CS) are shown, both for signal and background, and at truth and reco level. Looking at the plots, the discrimination power of D_2 and \mathcal{O} can be appreciated and the detector effects, in particular on pull variables, can be observed. In Fig. 2 the average Lund images for the signal and background processes in the truth and reco case are presented. From the plot, it is possible to appreciate the detector effect on the images, which adds in the reco case a radiation for the middle values of Δ and k_t . After having determined the distributions of the CS observables and the Lund jet images, these are used as inputs to ML algorithms in order to build combined classifiers. Specifically, a Boosted Decision Tree (BDT) is trained on the CS observables, whereas Lund images are classified using a Convolutional Neural Network (CNN). The output distribution of CNN Lund jet plane classifier is shown in Figure 2. More details about these methods and architectures are provided in ⁷⁾. Different combinations of variables are also considered in order to improve the total discrimination power. In this case the procedure is in two steps and uses the CNN Lund jet plane classifier as an additional input to the BDT.

In Fig. 3 the receiver operating characteristic (ROC) curves for several combinations of observables are shown. The background rejection ($1/\epsilon_b$) vs the signal efficiency (ϵ_s) is presented: the higher the curve, the better the discriminant power. Namely, we have considered: all the colour-sensitive observables (CS) or just the D_2 and the colour ring (D_2 +CR), combined through a BDT; the CNN Lund jet plane classifier (LP_{CNN}); the combination of all the CS observables with the (CS+LP_{CNN}), by means of the two-step procedure explained above. For each curve in Fig. 3, the value of the area under the ROC curve (AUC) is reported in Table 2.

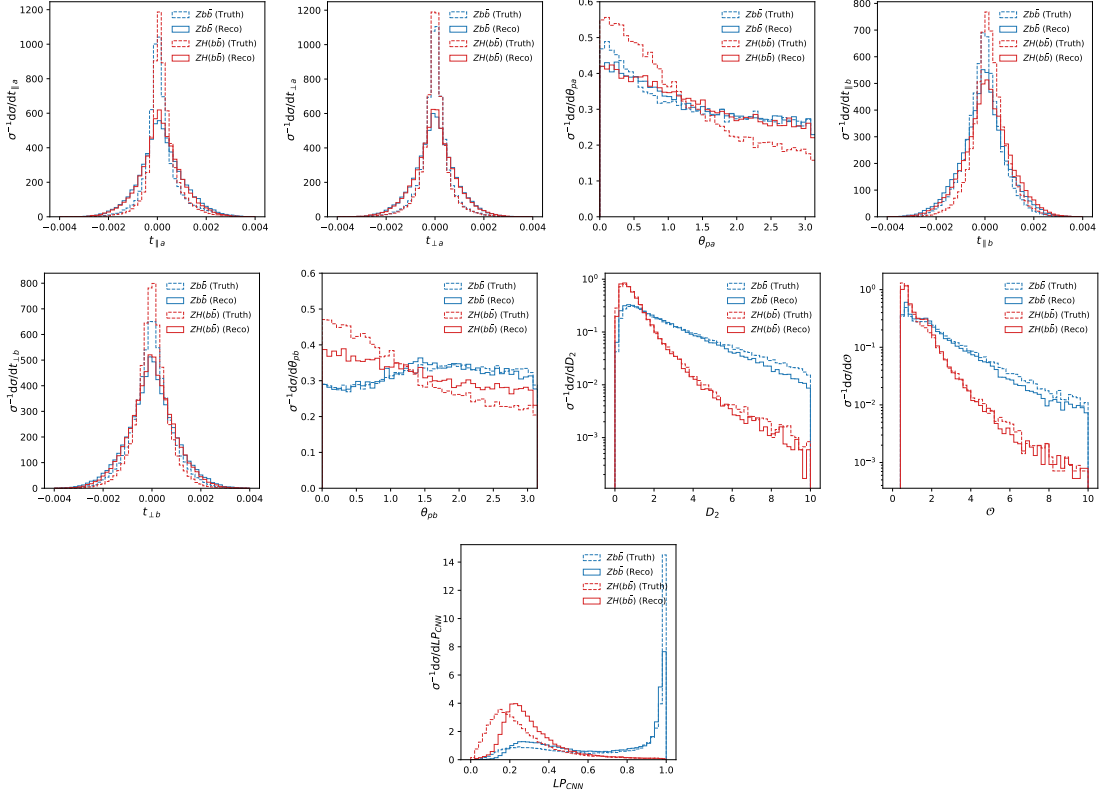


Figure 2: *Observables for signal and background, truth and reco cases, as defined in Section 2* ⁷⁾.

3.3 Results

As expected, the performances are worse in the reco case, due to detector resolution. However, discrimination is still good for most combinations, close to 0.85 for CS + LP_{CNN} . It is evident that most of the discriminating power of CS is due to D_2 +CR alone, both in AUC values and in distributions. It is clear that pull variables are not as powerful in discrimination as the other variables. Moving to combination with Lund jet plane, Lund jet plane alone performs better than the whole set of CS observables. When LP_{CNN} is combined with CS observables, there is a noticeable improvement of the overall classification power, with a value of AUC equal to 0.893 in the truth case and 0.846 in the reco case.

4 Conclusions

In this paper, the problem of finding a $Xb\bar{b}$ tagger, namely how to distinguish the b -jets originating from a colour singlet, such as Higgs boson, from those originating from the QCD background is investigated. Colour-sensitive observables present in literature are exploited in combination in order to perform a powerful discriminator. These observables are tested on the signal process $pp \rightarrow H(b\bar{b})Z(\nu_\ell\bar{\nu}_\ell)$, but the strategy can be valid in a more general context. The discrimination performance is estimated using ML techniques, namely BDT and CNN architecture. The BDT is trained with the colour-sensitive variables, including the Lund jet plane CNN discriminator. The results are encouraging, with a power in discrimination of 0.893 AUC for the combination of CS + LP_{CNN} .

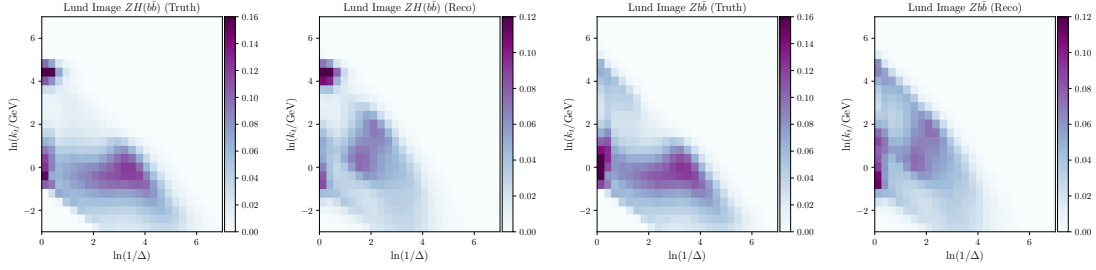


Figure 3: Averaged primary Lund jet plane images for $ZH(b\bar{b})$ and $Zb\bar{b}$ in the truth and reco case γ .

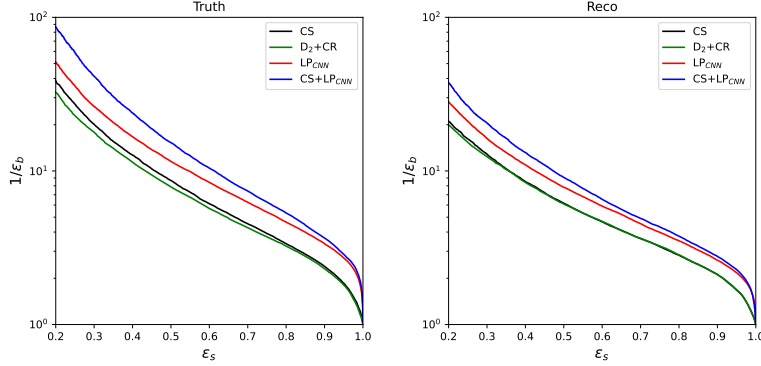


Figure 4: The ROC curves showing background rejection as a function of signal efficiency for the truth (left) and reco case (right) for CS variables, LP_{CNN} and the combined cases γ .

In the end, this tagger, which is a combination of several theory-driven single-variable observables with a representation of the radiation pattern within a jet, is not only effective in theory, but also shows promising prospects for application to experimental analyses.

5 Acknowledgements

The author acknowledges the University of Pavia, in particular her supervisor Daniela Rebuffi, for the opportunity to attend the Frascati Summer School. We also thank the authors of the publication which inspired this paper γ): Luca Cavallini, Andrea Coccaro, Charanjit Khosa, Simone Marzani, Fabrizio Parodi, Daniela Rebuffi, Alberto Rescia and Giovanni Stagnitto. In the end, the author acknowledges the organizers of the LNF ‘Bruno Touschek’ Summer School for the opportunity to present this work.

References

1. ATLAS Collaboration, G. Aad et al., *Phys. Lett. B* **716**, 1 (2012).
2. CMS Collaboration, S. Chatrchyan et al., *Phys. Lett. B* **716**, 30 (2012).
3. ATLAS Collaboration, M. Aaboud et al., *Phys. Lett. B*, **786**, 59 (2018).
4. CMS Collaboration, A.M. Sirunyan et al., *CMS-PAS-HIG-18-016*, (2018).

5. J. Gallicchio and M.D. Schwartz, *Phys. Rev. Lett.* **105**, 022001 (2010).
6. A.J. Larkoski, G.P. Salam and J. Thaler, *JHEP* **2013**, 108 (2013).
7. L. Cavallini, A. Coccaro, C.K. Khosa, G. Manco, S. Marzani, F. Parodi, D. Rebutti, A. Rescia and G. Stagnitto, *Eur. Phys. J. C*, **82**, 493 (2022).
8. ATLAS Collaboration, *ATL-PHYS-PUB-2020-019*, (2020).
9. A.J. Larkoski, S. Marzani, C. Wu, *Phys. Rev. D* **99**, 091502 (2019).
10. Y. Bao and A.J. Larkoski, *JHEP* **12**, 035 (2019).
11. A.J. Larkoski, S. Marzani and C. Wu, *SciPost Phys.* **9**, 026 (2020).
12. I. Moutl, L. Necib and J. Thaler, *JHEP* **12**, 153 (2016).
13. F.A. Dreyer, G.P. Salam and G. Soyez, *JHEP* **12**, 064 (2018).
14. J. Alwall, R. Frederix, S. Frixione, V. Hirschi, F. Maltoni, O. Mattelaer et al., *JHEP* **07**, 079 (2014).
15. T. Sjostrand, S. Ask, J.R. Christiansen, R. Corke, N. Desai, P. Ilten et al., *Comput. Phys. Commun.* **191**, 159 (2015).
16. DELPHES 3 Collaboration, *JHEP* **02**, 057 (2014).

PRUNING DEEP NEURAL NETWORKS FOR LHC CHALLENGES

Daniela Mascione

Università degli Studi di Trento and TIFPA, Via Sommarive 14, 38123 Trento, Italy
Fondazione Bruno Kessler, Via Sommarive 18, 38123 Trento, Italy

Abstract

The enormous amount of data generated at the Large Hadron Collider makes it challenging to maintain current event selection mechanisms. There is growing interest in attempting to make use of Deep Neural Networks for event selection with the aid of FPGAs, already employed at the selection early stages. However, because of the constraints imposed by systems based on FPGAs, Deep Learning algorithm design is made more difficult. We therefore investigated a pruning strategy for quickly optimizing Deep Neural Networks under size constraints to fit the resources of FPGAs.

1 Introduction

The Large Hadron Collider (LHC) at CERN produces on average 40 million proton-proton collision events each second. As a result of the detection of the particles produced in these events in the sensors of detectors positioned all around the LHC ring, roughly 40k ExaBytes of raw data are generated in one year of operation ¹⁾. Due to bandwidth restrictions, the main general-purpose particle detectors at the LHC, ATLAS and CMS, discard the majority of collision events through a two-steps selection mechanisms ²⁾. The initial selection stage, known as the level-1 trigger (L1T), is where the majority of events are discarded. Its job is to reduce the event rate by 2 orders of magnitude in a few microseconds ($\mathcal{O}(1)\mu\text{s}$). In the L1T algorithms are implemented as programmable logic on special electronic boards with field-programmable gate arrays (FPGAs). The events acknowledged by the L1T are then further processed in the so-called High Level Trigger (HLT) with selection algorithms on readily available CPUs and GPUs.

Making sure not to discard interesting events is a big challenge, and Deep Learning algorithms might be useful in this regard. There are several community efforts to explore the possibility to apply Deep Learning in the selection stages, especially in the L1T, prior to the introduction of any selection

bias. Recent developments in this field make it possible to deploy Deep Neural Networks (DNNs) on the FPGAs mounted on the L1T boards ³⁾. However, DNNs have to be adapted to fit the L1T infrastructure. In this context, we investigated an effective method to resize DNNs by pruning superfluous nodes.

2 Deep Neural Networks

DNNs are computing systems designed for non-linear learning problems ⁴⁾. They are based on a collection of connected basic units or nodes called artificial neurons that are aggregated into layers. Simple neural network architectures are made of three kinds of layers: the input layer, the output layer, and the hidden layer. Networks that have more than one hidden layer are called Deep Neural Networks.

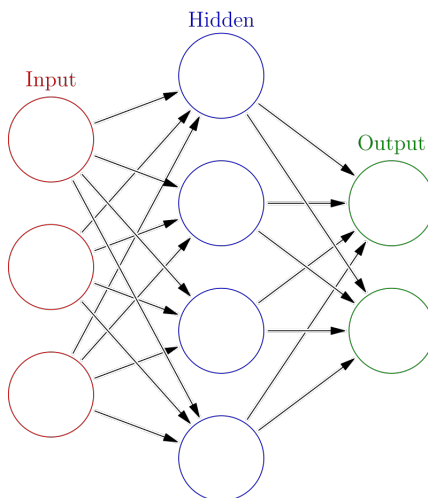


Figure 1: *Schematic representation of an artificial neural network with the input layer, the output layer, and one hidden layer. Source: https://commons.wikimedia.org/wiki/File:Colored_neural_network.svg*

Through a process called training, neural networks learn to recognize a pattern in the input data. During training, nodes convert weighted inputs into outputs: each neuron performs calculations that comprise a linear combination of the input data, which is then passed through a non-linear function called activation function. The activation function's primary goal is to disrupt the model's linearity. All these computations are carried out over the entire network: neurons receive inputs and produce a single output that is sent to multiple other neurons of subsequent layers. The inputs to a neuron may be the outputs of other neurons or they may be external data (such as images). The goal of recognizing a pattern in the input data (such as identifying an object in an image, for example) is accomplished by the outputs of the neural network's final output neurons (that may, for instance, be the likelihood of an object appearing in an image). The network's performance is then evaluated in relation to the expected output and the network's various parameters are modified to restart the calculation process in order to achieve an accurate result.

3 Pruning

Typically DNNs, especially the more effective ones, call for colossal amounts of computation and memory. These demands don't always correspond to the FPGAs' programmable resources (like the number of logic

units and memory slots), hence DNNs must be optimized before being implemented on FPGAs. Neural network pruning, which consists in eliminating superfluous structures from an existing network, is a popular strategy for lowering DNNs resource requirements ⁵⁾. The goal is to downsize a large, accurate starting network without suffering too much performance loss.

There are many different strategies to prune a DNN. The most popular pruning techniques are based on removing single parameters in accordance with a particular ranking determined after the starting network has been trained to convergence ⁶⁾. The pruned model is then retrained to recover from performance loss. Typically, pruning and retraining are conducted repeatedly, gradually shrinking the network. These techniques can be time-consuming as a result. For this reason, we investigated an alternative strategy for shrinking DNNs by removing during training the number of nodes determined by the user. This strategy works by adding a shadow network - whose neurons have just one connection to each of the single nodes of the original network - on top of the DNN that needs to be optimized. The layers of the shadow network contribute to training, as training is optimized for learning with precisely the required number of nodes: the calculations performed by the shadow nodes during training are such that their output will be zeroed when they are connected to “undesired” nodes. As a result, some nodes will be “switched off” and only a fraction of neurons will be used for learning.

4 Tests and results

The aforementioned pruning strategy has been tested to resize a DNN used to identify jets that contain b -quarks originating from boosted Higgs bosons decay in proton-proton collision events. The $H \rightarrow b\bar{b}$ channel accounts for 58% of all Higgs boson decays ⁷⁾, and it is therefore important for the investigation of Higgs boson properties. However, it can be difficult to identify these events in a proton-proton collision experiment because of the massive, irreducible background coming from QCD multi-jet production. The DNN used for tests was developed to distinguish between this background and the Higgs boson decay, without including pile-up effects.

Different networks were pruned during training by varying the number of desired nodes to be used for learning. Figure 2 shows the background rejection rate as a function of the Higgs tagging efficiency. A higher rate of background rejection for each tagging efficiency value denotes better DNN performance. Better performance is achieved with higher number of nodes required, as expected: this suggests that only the indicated percentage of nodes is actually used for learning, while the remaining nodes have been “turned off”.

In theory, the pruned DNNs might be retrained as independent models. The results are consistent with those that can be achieved by pruning during training, as shown in Figure 3, and there is therefore no need for fine-tuning following pruning.

5 Conclusion

A pruning strategy for reducing the number of DNNs nodes used for learning has been investigated. As a result, the overall size of the neural network is reduced, with the user ultimately determining its final dimensions. This makes it possible to adapt Deep Neural Networks to fit the resources of FPGAs used at the early stages of event selection at the LHC, in the challenging task of making sure not to discard interesting events.

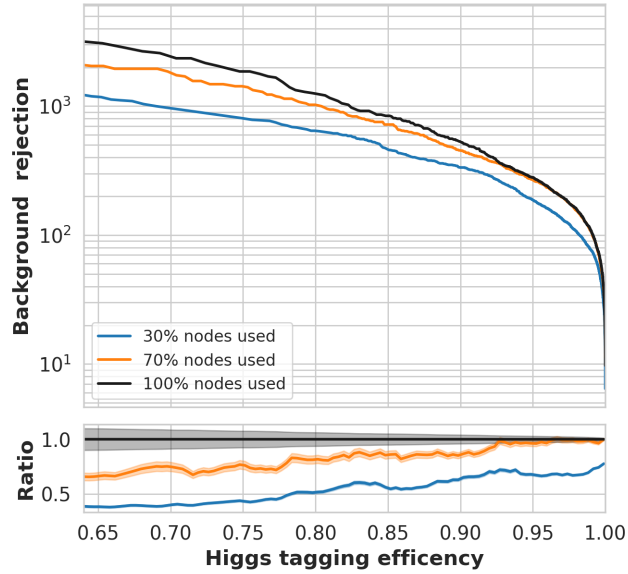


Figure 2: *Background rejection rate versus Higgs tagging efficiency for different models pruned during training by varying the number of desired nodes.*

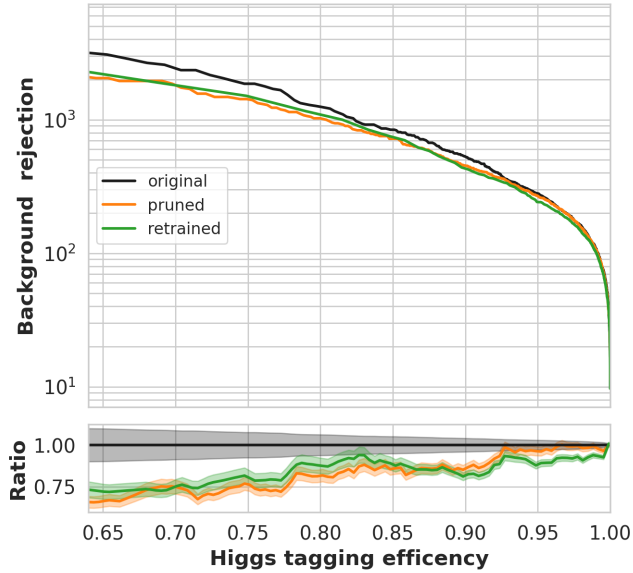


Figure 3: *Background rejection rate versus Higgs tagging efficiency for the original model (black), the model pruned during training (orange) and the retrained pruned model (green).*

6 Acknowledgements

The work described in this paper has been carried out in a joint effort with Andrea Di Luca, Francesco Maria Follega, Marco Cristoforetti and Roberto Iuppa, members of the *deepPP* group of the University of

Trento and Fondazione Bruno Kessler. For contacts and information about the group's activities please visit <https://www.deeppp.eu/>

References

1. L. Clissa, arXiv:2202.07659 (2022).
2. W.H. Smith, Annu. Rev. Nucl. Part. Sci., **66**, 123 (2016).
3. J. Duarte *et al.*, JINST **13**, P07027 (2018).
4. Y. LeCun *et al.*, Nature **521**, 436 (2015).
5. Y. Cheng, *et al.*, IEEE Signal Processing Magazine, **35 (1)**, 126 (2018).
6. D. Blalock *et al.*, What is the state of neural network pruning?, in: Proceedings of machine learning and systems 2, 129 (2020).
7. LHC Higgs Cross Section Working Group collaboration, Handbook of LHC Higgs Cross Sections: 4. Deciphering the Nature of the Higgs Sector, in: CERN Yellow Reports: Monographs, **2/2017**, (2017).

STUDYING RADIATIVE CHARM-MESON DECAYS AT THE LHCb EXPERIMENT

Aleksei Chernov

Institute of Nuclear Physics of Polish Academy of Sciences, Krakow

Abstract

A measurement of branching fractions and A_{CP} for the radiative charm meson decay modes $D^0 \rightarrow K^*\gamma$, $D^0 \rightarrow \rho\gamma$ and $D^0 \rightarrow \phi\gamma$ is performed. Simulations have been finalized and a data-driven approach in order to correct for possible differences between data and Monte-Carlo output has been considered. The analysis is still work in progress and no unblinding has taken place.

1 Introduction

These proceedings concern the radiative charm meson decays $D^{*+} \rightarrow (D^0 \rightarrow V\gamma)\pi^+$ (+c.c.), where V stands for a vector meson ϕ , ρ or K^* . Some Feynman diagrams contributing to those processes are shown in Fig 1. Results are presented for the $D^0 \rightarrow K^*\gamma$ channel, which has a higher branching fraction by an order of magnitude ¹⁾. Only prompt decays, i.e decays where the D^* is produced in the initial collision, are considered. In principle, secondary decays where the D^* is produced in the decay of a B meson can be used to study the same physics, but for this analysis they are suppressed by a cut on the D^0 impact parameter.

1.1 Motivation

$D^0 \rightarrow \phi\gamma$ and $D^0 \rightarrow \rho\gamma$ decays are highly suppressed in the Standard Model ($BR \sim 10^{-5}$) and therefore could be sensitive to New Physics. In particular, the CP asymmetry between D^0 and \bar{D}^0 mesons could be different from the Standard Model prediction, however, a good experimental precision is required. Previous studies of radiative charm decays by the BELLE collaboration ²⁾ were limited mostly by statistics.

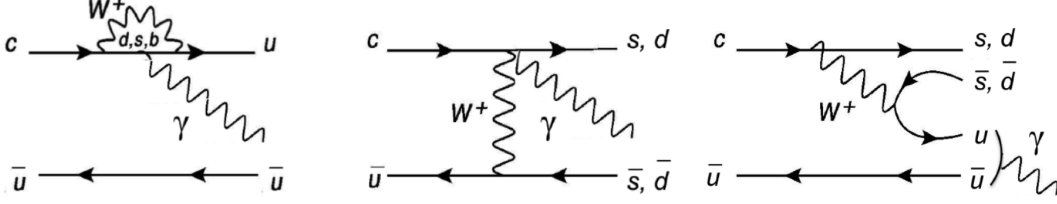


Figure 1: *Examples of radiative charm decays. From left to right: penguin (with possible BSM enhancement in the loop), tree-level and a long-distance diagrams.*

1.2 Experimental challenges for the radiative charm decays at the LHCb

Photons in radiative charm decays are relatively soft, i.e. with energy ~ 1 GeV. The photon combinatorial background tends to decrease with transverse momenta, so softer photons (compared to, e.g, beauty decays) mean more combinatorial background. The trigger efficiency in the soft region is also quite low: $\epsilon < 10^4$.

For neutral objects, one can only use the information from the calorimeter cluster to reconstruct. This leads to a much worse resolution compared to purely hadronic or semileptonic final states. But perhaps the most challenging aspect is the presence of an irreducible peaking background in form of $V\pi^0$. Since the π^0 almost always decays into two photons ¹⁾, we have two classes of such a background:

- *Resolved* π^0 , where both γ 's are reconstructed as separate calorimeter clusters, but one of them is missed in the reconstruction of the full decay chain. Missing energy/momentum means that we have a tail on the low-mass side.
- *Merged* π^0 , where the $\gamma\gamma$ final state is reconstructed as a single cluster. This background peaks in the same region of invariant mass as the radiative signal, but has a significantly higher branching fraction, and discriminating this overwhelming peaking background from the signal is the main challenge of the radiative analyses.

For extraction of A_{CP} , the nuisance asymmetries, namely the production asymmetry between D^{*+} and D^- and the detection asymmetries for final-state hadrons, need to be taken into account, which necessitates the usage of reference channels. The raw asymmetry reads:

$$A_{raw} = A_{CP} + A_{production}(D^{*\pm}) + A_{detection}(h^\pm) \quad (1)$$

For $\phi\gamma$ and $\rho\gamma$, fully hadronic $D^0 \rightarrow KK$ and $D^0 \rightarrow \pi\pi$ are used as reference channels. The kinematic reweighting is used to match the momenta of the D^0 daughters and the slow pion to the signal, thus:

$$A_{raw}^{sig} - A_{raw}^{ref} \approx A_{CP}^{sig} - A_{CP}^{ref}. \quad (2)$$

CP violation in the charm sector had been discovered in 2019 ³⁾, in the form of $\Delta A_{CP} = A_{CP}(KK) - A_{CP}(\pi\pi)$, however, individual asymmetries for KK and $\pi\pi$ modes are not yet known precisely.

2 Analysis strategy

2.1 Overview

We use 2 fb^{-1} of the LHCb data collected in Run 1. Additional 3.5 fb^{-1} of Run 2 data is available, but at the moment we focus on finalizing the analysis with just Run 1 data. The full decay chain is:

$$D^{*+} \rightarrow (D^0 \rightarrow V\gamma)\pi_{soft}^+ ; D^{*-} \rightarrow (\bar{D}^0 \rightarrow V\gamma)\pi_{soft}^- ; V = \rho, \phi, K^*.$$

The vector mesons' final state is a pair of charged hadrons: $\phi \rightarrow KK$, $\rho \rightarrow \pi\pi$, $K^* \rightarrow K^-\pi^+$. The flavour of the initial charmed meson (D^0 or \bar{D}^0) is *tagged* by the charge of the soft pion; in the event reconstruction, we require two charged tracks, a photon-like object and a soft pion.

2.2 Discriminating variables

As mentioned in the introduction, we are challenged by a dominant background that is completely swamping the signal if one looks only at the invariant mass. However, γ is a vector, while π^0 is a pseudoscalar, which leads to different polarisations. A previous BELLE analysis ²⁾ uses a 2D fit to the invariant mass and helicity angle θ of the vector meson V (see Figure 2). We add a third discriminating

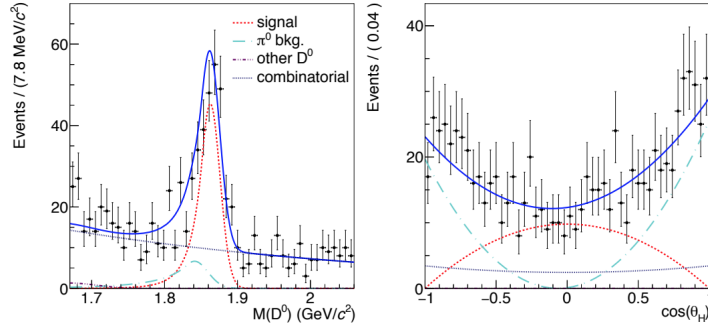


Figure 2: *Multi-dimensional fit to the invariant mass (left) and helicity angle of ϕ for the $D^0 \rightarrow \phi\gamma$ data. Figure taken from ²⁾.*

variable, namely $\Delta M \equiv M(D^*) - M(D^0)$. The effects that worsen the mass resolution subtract to the first order, resulting in a much narrower peak, so that this observable allows us to control mis-tagging, i.e. recombining a good D^0 decay with a wrong π_{slow}^\pm , since such decays exhibit a peak in the $M(D^0)$ and θ mass distributions, but not in ΔM . Figure 3 shows an example of a fit to the ΔM distribution using the Run 1 simulation. One can easily see that resolution is $\mathcal{O}(\text{MeV})$, while for $M(D^0)$, it is $\mathcal{O}(100\text{MeV})$. The data sample is divided into two subsets by selecting a range in $\cos\theta$: a calibration set, close to the helicity edge, where the signal is suppressed and the peaking background is dominant, and a helicity central region, where the signal dominates. Models for each observable are created using Monte Carlo simulations and validated with calibration sets. In the central helicity region, all shapes are fixed and only the relative yields are free. From the multidimensional simultaneous fit to π^+ - and π^- -tagged data, the raw asymmetry $A_{raw} = A_{CP} + A_{detection} + A_{production}$ can be extracted.

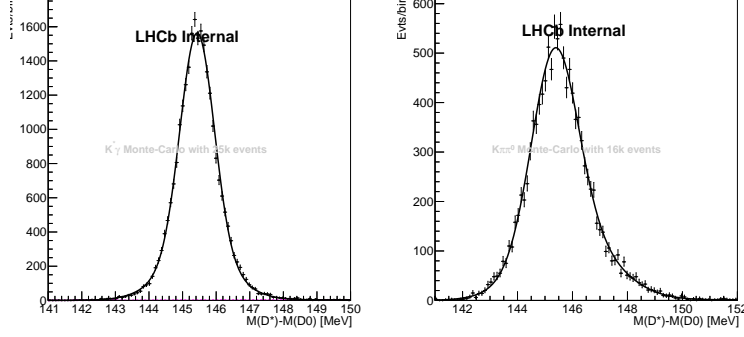


Figure 3: Fits to the ΔM observable using Run 1 simulation for $D^0 \rightarrow K^*\gamma$ (left) and $D^0 \rightarrow K^-\pi^+\pi^0$ (right).

2.3 Treatment of correlated observables

A complication of adding the ΔM observable to the two-dimensional fit is that now not all of our observables are independent. We chose to use a relatively simple model to incorporate correlations between M and ΔM observables. By using simulations, one fits the ΔM distribution in bins of M , with all shape parameters fixed except a scale factor λ , that is applied to the width(s) of the Gaussian-like component(s). The effective width of the ΔM distribution then becomes a function of $M(D^0)$:

$$\sigma_{\Delta M} = \sigma_{\Delta M}^0 \times \lambda(M). \quad (3)$$

From the fits in bins, we obtain a histogram of $\lambda(M)$ and fit it with a polynomial function, typically limited to the third order to avoid overfitting. Thus, the effective width becomes:

$$\sigma_{\Delta M} = \sigma_{\Delta M}^0 \times (P_0 + P_1M + P_2M^2 + P_3M^3). \quad (4)$$

Correlations between observables in peaking backgrounds are treated in the same way. In the multi-dimensional fit, we have to use a conditional probability density function:

$$P = [F^1(\Delta M|M) \times F^2(M)] \times G(\cos \theta). \quad (5)$$

Parameters (P_0, P_1, P_2, P_3) are determined by fitting same ΔM model in the bins of $M(D^0)$ (see Eq. 4), with only a scale factor λ , applied to the width of the double Gaussian function, as a free parameter of the fit. Then, a histogram of λ is fitted by a third-order polynomial (Fig. 5), in order to obtain a continuous functional form.

2.4 Secondary peaking background

In addition to the $V\pi^0$ peaking background, $V\eta$ decays, where one of the photons in the final state $\eta \rightarrow \gamma\gamma$ is missed, pass our reconstruction and selection. Although the mean of the η peak is almost 200 MeV below that of radiative signal (Figs.6 and 2), because of the aforementioned poor resolution for the invariant mass of final states with neutral particles, it overlaps with the lower-mass part of the $V\pi^0$ peak. This background is treated similarly to $V\pi^0$: models for all observables are determined from Monte-Carlo simulations, and then fits to ΔM in bins of $M(D^0)$ are performed to parametrize the dependence of the ΔM resolution on $M(D^0)$ with a third-order polynomial.

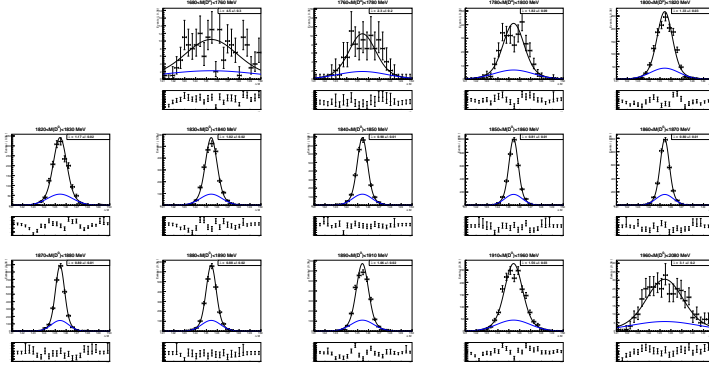


Figure 4: Fits to the ΔM observable in bins of $M(D^0)$, using Run 1 simulation for $D^0 \rightarrow K^*\gamma$. One can easily discern that ΔM resolution is the best around the signal peak in $M(D^0)$ and degrades with the distance from the peak, in both higher- and lower-mass regions

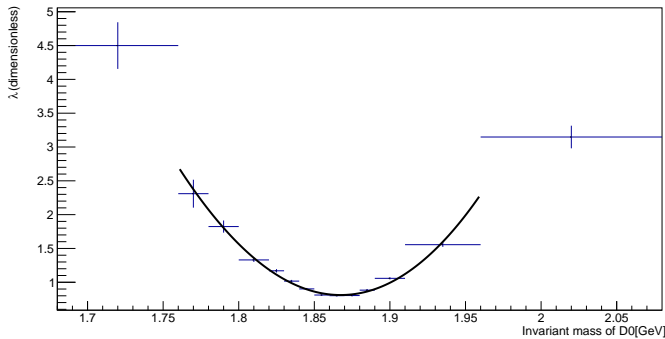


Figure 5: Values of a scale factor λ , which is the only free parameter allowed to change between different bins of invariant mass, with a polynomial fit curve.

2.5 Multiple candidates treatment

For the Run 1 data, the pileup is not as significant as for Run 2 or for prospective Run 3 data, so we do not expect any significant effect. Monte Carlo studies suggest that, after applying an offline selection, we have negligible (less than 1%) proportion of events that contain multiple D^0 candidates; however, in real data we observe a fraction $\sim 1\%$ for all channels. Although small, the subsample with event multiplicity $\mu = 2$ has significantly higher fraction of combinatorial background (see Fig.7). In order to suppress it, for every event that has more than one D^0 candidate we select the one with the lowest χ^2 according to *DecayTreeFitter*⁴ (a mechanism utilizing Kalman filters to reconstruct vertices and tracks first developed at B -factories) and discard the second one (and further orders of multiplicity, but there is only one event with $\mu > 2$ after offline selection).

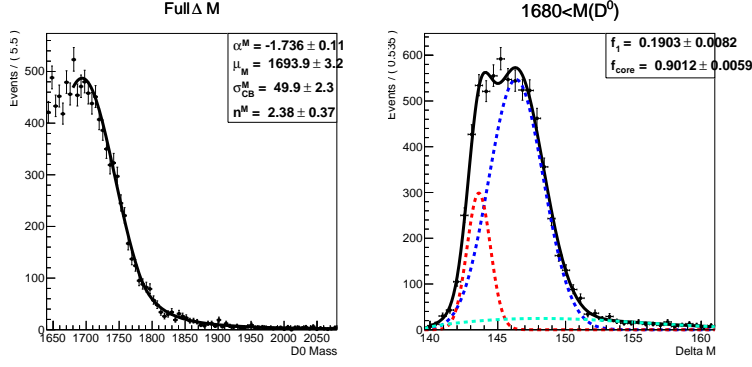


Figure 6: Multidimensional fit to the $D^0 \rightarrow K^*\eta$ simulation with one photon in the final state $\eta \rightarrow \gamma\gamma$ missing. Correlations between observables are incorporated, although for the η channel they are significantly weaker compared to γ and π^0 modes.

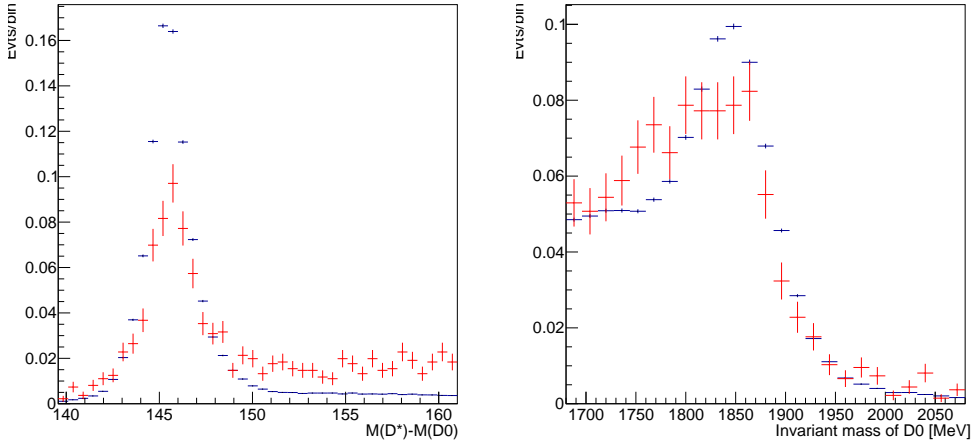


Figure 7: Normalized ΔM (left) and $M(D^0)$ (right) distributions for subsamples of the Run 1 $K^*\gamma$ data with event multiplicity $\mu = 1$ (blue) and $\mu \geq 2$ (red).

3 Fits to the calibration data

We use a calibration sample mainly to allow for corrections of differences between data and Monte-Carlo simulations. The following components are considered: the radiative signal (very small in a calibration sample), the $V\pi^0$ background (dominant), the $V\eta$ background (sub-leading), the pure combinatorial and the background components for both photon and π^0 , where the D^0 meson is combined with a random soft pion. This is a combinatorial background that peaks in $M(D^0)$ and can only be resolved by the third observable. The yields for each class are free; a common scale factor ν is applied to the widths of all peaking components in the invariant-mass spectrum. Another scale factor is applied to the width of the ΔM component, that is shared between γ and π^0 modes, but is separate for η . The signal-enhanced projections (selecting a window of 3σ in ΔM) of the fit to the calibration data are shown in Fig. 8.

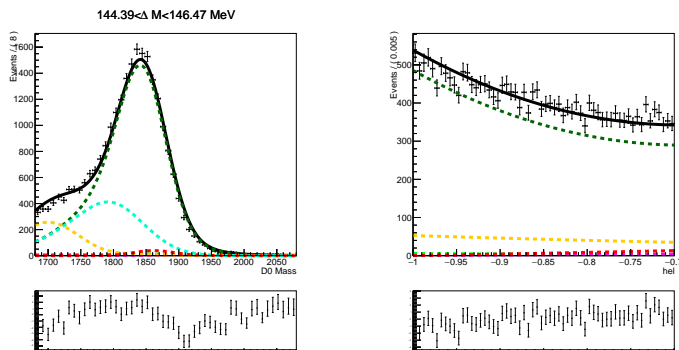


Figure 8: *Signal-enhanced region projection of the three-dimensional fit to the calibration subsample ($\cos\theta < -0.7$) of data collected in Run1, $K^*\gamma$ channel. Green is π^0 peaking background, red is radiative signal, orange is η peaking background. Combinatorial components in the signal-enhanced region are negligible.*

4 Outlook

Our group is still working on finalizing the fits presented, mostly to ensure that we understand the cross-feeding between the low-mass tail in the π^0 component, the η peak and their combinatorics. The next step is to freeze the shapes with the corrections we obtained from the calibration and fit the signal-enhanced helicity region. From the simultaneous fit to the signal helicity region, the raw asymmetry A_{raw} for each of the channels will be obtained, which will then be combined with the reference channels to obtain A_{CP} .

5 Acknowledgements

I thank to my supervisor Jolanta Brodzicka, who is the leader of this analysis, my co-worker Shantam and Prasanth, Mark Williams from Manchester, all of the wonderful CERN staff members, who kept the facilities running during the pandemic lockdowns, and to my wonderful family who supported me in those troubled times. And, of course, special thanks to the organizers of the Frascati Summer School!

References

1. R.L. Workman et al. (Particle Data Group), Prog. Theor. Exp. Phys. (2022) (2022).
2. Belle Collaboration (T. Nanut et al.), ‘Observation of $D^0 \rightarrow \rho\gamma$ and Search for CP Violation in Radiative Charm Decays’, Phys. Rev. Lett. **118**, 051801 (2017).
3. LHCb Collaboration (R. Aaij et al.), ‘Observation of CP Violation in Charm Decays’, Phys. Rev. Lett. **122**, 211803 (2019).
4. W. D. Hulsbergen, ‘Decay Chain Fitting with a Kalman Filter’, Nucl. Instrum. Meth. A **552**, 566-575 (2005) (preprint available at <https://arxiv.org/abs/physics/0503191>).

**ANALYSIS OF THE $B^0 \rightarrow K^{*0} \mu^+ \mu^-$ DECAY
IN THE HIGH $K\pi$ INVARIANT-MASS REGION AT THE LHCb EXPERIMENT**

Józef Borsuk
on behalf of the LHCb Collaboration
Institute of Nuclear Physics Polish Academy of Sciences

Abstract

Measurements of the differential branching fraction and angular moments of the decay $B^0 \rightarrow K^{*0}(\rightarrow K^+ \pi^-) \mu^+ \mu^-$ in the $K^+ \pi^-$ invariant mass range $1330 \text{ MeV}/c^2 < m_{K\pi} < 1530 \text{ MeV}/c^2$ performed by the LHCb collaboration are presented. The preparation of a new analysis based on data from the LHC Run 2 is announced.

1 Introduction

One of the main goal of modern particle physics is to test theory predictions of the so-called Standard Model (SM) ¹⁾. This model defines all discovered elementary particles and describes interactions between them in a way of exchanging particles. It does not incorporate gravitational interactions. The development of a such model is a great success, however, the SM is not free from several open issues. One of the main problems is the fact that in the Universe there is more matter than antimatter. Additionally, the SM does not incorporate dark matter particles, dark energy and describes neutrinos as massless particles. With this number of unexplained phenomena it is important to search for so-called physics Beyond the Standard Model (BSM) which would help in better understanding Nature.

One of the best way to look for new phenomena is to investigate flavour-changing neutral current (FCNC) processes such as the $B^0 \rightarrow K^{*0} \mu^+ \mu^-$ decay ²⁾. In FCNC transitions one quark changes its flavour without changing its electric charge; such processes are highly suppressed in the SM by the so-called GIM mechanism ³⁾. In the SM FCNCs can proceed only through electroweak penguin or box diagrams. New Physics can be tested indirectly when some new heavy particles would enter the loop causing anomalies with respect to the SM predictions. Those anomalies can be studied through angular analyses of the $B^0 \rightarrow K^{*0} \mu^+ \mu^-$ decay, which can reveal yet unknown contributions, for instance an

additional vector or axial vector introduced by some New Physics models ⁴⁾. The results presented in this paper are based on the analysis of 3 fb⁻¹ data set of pp collisions collected by the LHCb experiment during Run 1 ⁵⁾. The author of this contribution is working on a similar analysis based on data from Run 2, which corresponds to an integrated luminosity of almost 6 fb⁻¹.

2 LHCb detector

The LHCb detector ⁶⁾ is a single-arm forward spectrometer designed to study heavy flavour physics. It contains ring-imaging Cherenkov detectors (RICH1, RICH2), hadronic and electromagnetic calorimeters (HCAL, ECAL), muon identification systems (M1-M5) and tracking detectors of high precision (vertex locator - VELO, TT and T1-T3) - see Fig. 1. The fact that it covers a pseudorapidity range $2 < \eta < 5$, where most final-state particles from B-meson decays can be found, makes it an exceptional detector to study rare processes.

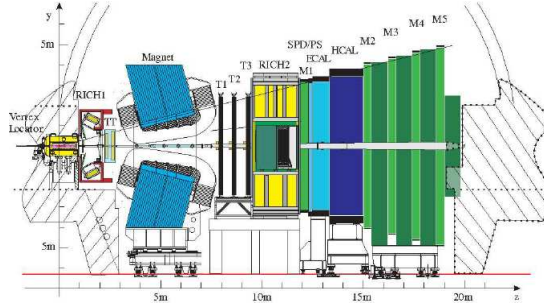


Figure 1: The LHCb detector ⁶⁾.

3 Description of the searched decay

The purpose of presented analysis is to perform both differential branching fraction measurement and angular analysis of the decay $B^0 \rightarrow K^{*0}(\rightarrow K^+\pi^-)\mu^+\mu^-$ in the high $K^+\pi^-$ mass region $1330 \text{ MeV}/c^2 < m_{K\pi} < 1530 \text{ MeV}/c^2$.

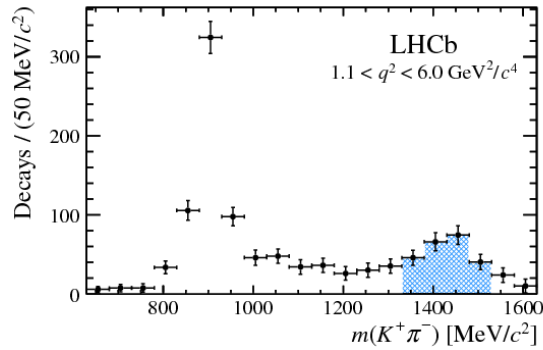


Figure 2: Invariant-mass distribution of the $K^+\pi^-$ system for $B^0 \rightarrow K^{*0}\mu^+\mu^-$ decays in the $1.1 \text{ GeV}^2/c^4 < q^2 < 6.0 \text{ GeV}^2/c^4$ range. The blue area indicates the region of interest ⁵⁾.

Most of the other analyses^{7, 8)} are focused on the $K^*(892)^0$ -resonance mass region, where events come predominantly from the P-wave (Figure 2). However, above this resonance, there is a distinct structure where contributions from S-, P- and D-waves could be found.

The $B^0 \rightarrow K^{*0}(\rightarrow K^+\pi^-)\mu^+\mu^-$ final state, as well as its CP-conjugated decay, is described by the squared invariant mass of the dimuon system q^2 , the three decay angles $\cos\theta_K$, $\cos\theta_\ell$ and ϕ , and by the invariant mass of the $K^+\pi^-$ system. The angle θ_K is the angle between the direction of $K^+(K^-)$ and the direction of $B^0(\bar{B}^0)$ in K^{*0} rest frame, θ_ℓ is the angle between the direction of $\mu^+(\mu^-)$ and the direction opposite to that of the $B^0(\bar{B}^0)$ in the rest frame of the dimuon system and ϕ is the angle between the planes constructed from the $K^+\pi^-$ system and the dimuon pair in the $B^0(\bar{B}^0)$ rest frame (Fig. 3).

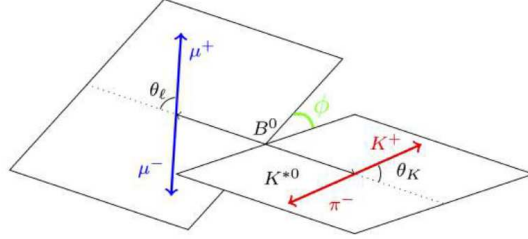


Figure 3: Angle conventions for the $B^0 \rightarrow K^+\pi^-\mu^+\mu^-$ decay.

4 Mass distribution

The fit to $B^0 \rightarrow K^+\pi^-\mu^+\mu^-$ candidates was performed, with the signal distribution modelled as the sum of two Gaussian functions with a common mean, each with a power-law tail on the low-mass side. The combinatorial background was modelled using an exponential function. The results of the fit in the range $1.1 \text{ GeV}^2/c^4 < q^2 < 6.0 \text{ GeV}^2/c^4$ are shown in Fig. 4, with a signal yield of 229 ± 21 candidates.

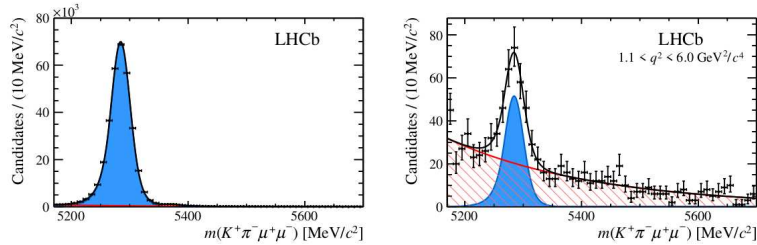


Figure 4: Invariant-mass distribution for the control decay $B^0 \rightarrow J\psi K^{*0}$ (left) and the signal decay $B^0 \rightarrow K^+\pi^-\mu^+\mu^-$ (right) in the $1.1 \text{ GeV}^2/c^4 < q^2 < 6.0 \text{ GeV}^2/c^4$ range. The solid black line represents the total fitted function. The signal is represented by the blue-shaded area, while the combinatorial background is depicted as a red-hatched area.⁵⁾

5 Differential branching fraction

The differential branching fraction $d\mathcal{B}/dq^2$ of the $B^0 \rightarrow K^+\pi^-\mu^+\mu^-$ decay was measured in 5 q^2 -bins in the $1330 \text{ MeV}/c^2 < m_{K\pi} < 1530 \text{ MeV}/c^2$ region:

$$\frac{d\mathcal{B}}{dq^2} = \frac{1}{q_{max}^2 - q_{min}^2} f_{K^*(892)^0} \mathcal{B}(B^0 \rightarrow J/\psi K^{*0}) \mathcal{B}(J/\psi \rightarrow \mu^+\mu^-) \times \mathcal{B}(K^*(892)^0 \rightarrow K^+\pi^-) \frac{N'_{K^+\pi^-\mu^+\mu^-}}{(1 - F_S^{J/\psi K^{*0}}) N'_{J/\psi K^{*0}}}, \quad (1)$$

where $N'_{K^+\pi^-\mu^+\mu^-}$ and $N'_{J/\psi K^{*0}}$ are the acceptance-corrected yields of the $B^0 \rightarrow K^+\pi^-\mu^+\mu^-$ and $B^0 \rightarrow J/\psi K^{*0}$ decays, respectively. The decay $B^0 \rightarrow J/\psi K^{*0}$ was used as a normalization channel and selected in the regions $9.22 \text{ GeV}^2/c^4 < q^2 < 9.96 \text{ GeV}^2/c^4$ and $796 \text{ GeV}^2/c^4 < m_{K\pi} < 996 \text{ MeV}/c^2$. $F_S^{J/\psi K^{*0}}$ is a S-wave fraction, while the fraction $f_{K^*(892)^0}$ was used to scale the value of $\mathcal{B}(B^0 \rightarrow J/\psi K^{*0})$ to the range $796 \text{ MeV}/c^2 < m_{K\pi} < 996 \text{ MeV}/c^2$. The most up-to-date branching fractions required in Eq. 1 were applied; Fig. 5 shows the results of the differential branching fraction measurements.

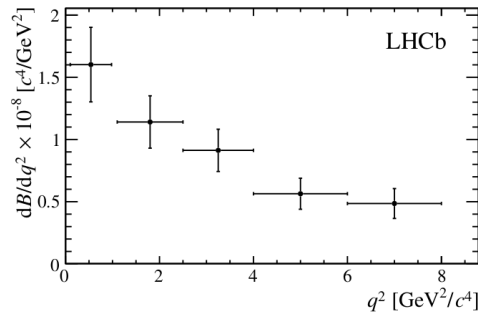


Figure 5: *Differential branching fraction of $B^0 \rightarrow K^+\pi^-\mu^+\mu^-$ decay in 5 bins of q^2 and in the $1330 \text{ MeV}/c^2 < m_{K\pi} < 1530 \text{ MeV}/c^2$ range. The error bars are the sums in quadrature of the statistical and systematic uncertainties.* 5)

6 Angular analysis

The CP-averaged differential decay rate of B^0 and \bar{B}^0 decays with the $K^+\pi^-$ system in S-, P-, and D-wave configurations can be presented as an expansion in an orthonormal basis of the angular functions $f_i(\Omega)$ 9):

$$\frac{d^4\Gamma}{dq^2 d\Omega} \propto \sum_{i=1}^{41} \Gamma_i(q^2) f_i(\Omega), \quad (2)$$

$$\Gamma_i(q^2) = \Gamma_i^L(q^2) + \eta_i^{L \rightarrow R} \Gamma_i^R(q^2),$$

where $d\Omega = d\cos\theta_K d\cos\theta_\ell d\phi$, $f_i(\Omega)$ is constructed out of the spherical harmonics $Y_l^m(\theta_\ell, \phi)$ and reduced spherical harmonics $P_l^m \equiv \sqrt{2\pi} Y_l^m(\theta_K, 0)$. The superscripts L and R stand for left- and right-handed chirality of the dimuon system. The sign of $\eta_i^{L \rightarrow R}$ depends on the f_i 's sign when $\theta_\ell \rightarrow \pi + \theta_\ell$. All 41 moments in an orthonormal basis are shown in Tab.IV of Reference 9). The first moment Γ_1 corresponds to the total decay rate, while 40 normalized moments were calculated as:

$$\bar{\Gamma}_i(q^2) = \frac{\Gamma_i(q^2)}{\Gamma_1(q^2)}. \quad (3)$$

7 Method of moments

In order to calculate the angular observables $\Gamma_i(q^2)$, the method of moments was used⁹⁾. The advantage of this approach is that it can provide good results even for small data samples. The moments in presence of background were estimated as:

$$\Gamma_i = \sum_{k=1}^{n_{sig}} \omega_k f_i(\Omega_k) - x \sum_{k=1}^{n_{bkg}} \omega_k f_i(\Omega_k) \quad (4)$$

where n_{sig} and n_{bkg} are the number of signal and background events, x is the ratio of the estimated number of background candidates in the signal region over the number of candidates in the background region and the weights ω_k are the inverse of the candidates' efficiencies.

Two moments $\bar{\Gamma}_5$ and $\bar{\Gamma}_{10}$ were used to determine the D-wave fraction F_D using following formula:

$$F_D = -\frac{7}{18}(2\bar{\Gamma}_5 + 5\sqrt{5}\bar{\Gamma}_{10}). \quad (5)$$

In Figure 6 all 40 normalized moments are presented and the values of the second and third moment suggest that large interference effects between the S- and P- or D-wave contributions are present. The available data sample allowed only to determine an upper limit for the the D-wave fraction as $F_D < 0.29$ at 95% confidence level, using the approach in Ref. 10).

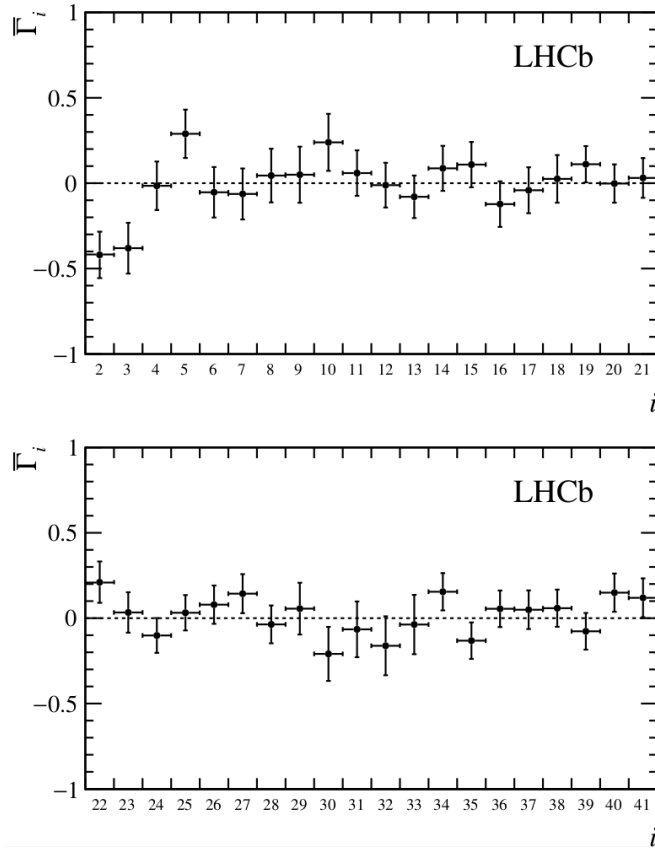


Figure 6: Results of the normalized moments $\bar{\Gamma}_i$ of the $B^0 \rightarrow K^+\pi^-\mu^+\mu^-$ decay rate in the ranges $1.1 \text{ GeV}^2/c^4 < q^2 < 6.0 \text{ GeV}^2/c^4$ and $1330 \text{ MeV}/c^2 < m(K^+\pi^-) < 1530 \text{ MeV}/c^2$. The error bars are the sums in quadrature of the statistical and systematic uncertainties.

8 Summary

The results presented in this talk are based on the analysis of the $B^0 \rightarrow K^+\pi^-\mu^+\mu^-$ decay in the $K^+\pi^-$ invariant mass range $1330 \text{ MeV}/c^2 < m(K^+\pi^-) < 1530 \text{ MeV}/c^2$, as performed by the LHCb collaboration. This analysis' main goal was to measure the differential branching fraction and the angular moments using a data sample consisting of 3 fb^{-1} of pp collisions collected by the LHCb experiment.

In this talk, the Author wanted to announce a new analysis based on almost 6 fb^{-1} of data from the LHCb experiment, which is currently under preparation. The preliminary results show that there are over three times more candidates which will eventually help with obtaining much more accurate results. Hopefully the continuation of FCNC searches will lead to discoveries explaining the already observed deviations from the SM predictions.

9 Acknowledgements

I would like to express my gratitude to colleagues in the CERN accelerator departments for the excellent performance of the LHC. A new project on the $B^0 \rightarrow K^+\pi^-\mu^+\mu^-$ decay analysis is fully funded by the National Science Center, Grant Number UMO-2021/41/N/ST2/03478.

References

1. R. Mann, CRC Press, ISBN 9781420082982 (2009).
2. J. Matias *et al.*, JHEP **04**, 104 (2012).
3. S.L. Glashow *et al.*, Phys. Rev. D **2**, 1285 (1970).
4. M. Alguer *et al.*, Eur. Phys. J. C **79**, 714 (2019).
5. LHCb Collaboration, JHEP **12**, 065 (2016).
6. LHCb Collaboration, JINST **3**, S08005 (2008).
7. LHCb Collaborations, Phys. Rev. Lett. **125**, 011802 (2020).
8. LHCb Collaborations, JHEP **02** 104 (2016).
9. B. Dey, Phys. Rev. D **92**, 033013 (2015).
10. G. J. Feldman and R. D. Cousins, Phys. Rev. D **57**, 3873 (1998).

On the effective lifetime of $B_s \rightarrow \mu\mu\gamma$

Camille Normand

Laboratoire d'Annecy-le-Vieux de Physique Théorique, 9 Chemin de Bellevue, 74941 Annecy-le-Vieux, France
Università degli Studi di Cagliari, Via Università, 40, 09124 Cagliari CA, Italy

Abstract

In this work, we consider the effective lifetime of $B_s^0 \rightarrow \mu\mu\gamma$, and the related CP -phase sensitive quantity $A_{\Delta\Gamma_s}^{\mu\mu\gamma}$, as a new probe of New Physics in $b \rightarrow s$ transitions. We explore its possibility to distinguish different scenarios allowed by present data, taking into account uncertainties coming from both form factors parametrization and charmonium resonances. These scenarios are described by shifts to the Wilson coefficients relevant to the $b \rightarrow s$ discrepancies. We find that, even though the current status of the form factors prevents $A_{\Delta\Gamma_s}^{\mu\mu\gamma}$ to tell apart the considered scenarios, the pollution coming from charmonium resonances modeling is very low (sub-percent level).

1 Introduction

In recent years, consistent deviations from the SM have been observed in heavy flavor physics. Phenomena of particular interest are the $b \rightarrow s\ell\ell$ transitions, in decay channels such as $B \rightarrow K^*\ell\ell$, where the muonic and electronic channels are predicted in the SM to have the same branching fractions (up to QED corrections). This precise aspect, a consequence of the Lepton Flavor Universality of the SM, has been challenged most notably by the LHCb experiment, thanks to measurements of ratios such as R_{K/K^*} ¹⁾ ²⁾ defined as

$$R_H = \frac{\mathcal{B}(B \rightarrow H\mu^+\mu^-)}{\mathcal{B}(B \rightarrow He^+e^-)} . \quad (1)$$

The strong interest into these ratios comes from the reduced theoretical uncertainty from the descriptions of the hadronic matrix elements. Such descriptions need, by their nature, non-perturbative QCD techniques, and thus often suffer from large errors. However, when computing a *ratio* of two wisely chosen observables, the errors coming from the numerator and denominator can partially cancel and thus lead to a much smaller theoretical error, even with very conservative assumptions.

In this work, based on a publication in *J. High Energ. Phys.* ³⁾, we present a potential new candidate for such an observable, $A_{\Delta\Gamma_s}^{\mu\mu\gamma}$, which is by definition a ratio observable, and accessible through the measurement of the effective lifetime $\tau_{\text{eff}}^{\mu\mu\gamma}$ of the $B_s^0 \rightarrow \mu\mu\gamma$ channel. This decay channel is also a probe of $b \rightarrow s$ transitions, and is interestingly sensitive to a wider set of Wilson coefficients (WCs) than its non-radiative counterpart, $B_s^0 \rightarrow \mu\mu$. When a measurement of the branching fraction gives access to the norm of the WCs or differences of weak phases, the measurement of the effective lifetime allows us to constrain the imaginary parts of the WCs, i.e. phases not aligned with the SM. This type of New Physics (NP) would give rise to non-SM-like CP violation, meaning not emerging from the CKM matrix, a quite under-explored area of potential NP in the $b \rightarrow s$ transitions.

In the second section, we describe the $B_s^0 \rightarrow \mu\mu\gamma$ decay and its amplitude. We will put particular emphasis on the high- q^2 region of the phase space (q^2 being the dilepton invariant mass). In the third section we define the effective lifetime, and in the fourth section, we present numerical results, before concluding in the last section.

2 The $B_s^0 \rightarrow \mu\mu\gamma$ decay

In the context of the Weak Effective Theory (WET), the $B_s^0 \rightarrow \mu\mu\gamma$ decay amplitude is given by the sum of two contributions: a ‘‘direct-emission’’ component $\mathcal{A}_{\text{DE}}(\bar{B}_s^0 \rightarrow \mu\mu\gamma)$, and a bremsstrahlung component $\mathcal{A}_{\text{Brems}}$, defined as ^{4) 5)}

$$\begin{aligned} \mathcal{A}_{\text{DE}}(\bar{B}_s^0 \rightarrow \mu\mu\gamma) &= \frac{G_F}{\sqrt{2}} V_{tb} V_{ts}^* \frac{\alpha}{2\pi} \times \\ &\quad \left\{ -\frac{2im_b C_7}{q^2} \langle \gamma(k, \epsilon) | \bar{s} \sigma_{\mu\nu} (1 + \gamma_5) q^\nu b | \bar{B}_s^0(p) \rangle \bar{u}(p_2) \gamma^\mu v(p_1) \right. \\ &\quad + C_9^{\text{eff}} \langle \gamma(k, \epsilon) | \bar{s} \gamma_\mu (1 - \gamma_5) b | \bar{B}_s^0(p) \rangle \bar{u}(p_2) \gamma^\mu v(p_1) \\ &\quad \left. + C_{10} \langle \gamma(k, \epsilon) | \bar{s} \gamma_\mu (1 - \gamma_5) b | \bar{B}_s^0(p) \rangle \bar{u}(p_2) \gamma^\mu \gamma_5 v(p_1) \right\}, \end{aligned} \quad (2)$$

$$\mathcal{A}_{\text{Brems}} = +i \frac{G_F}{\sqrt{2}} V_{tb} V_{ts}^* \frac{\alpha}{2\pi} e X_f f_{B_s} 2m_\mu C_{10} \left\{ \bar{u}(p_2) \left(\frac{\not{\epsilon}^* \not{p}}{t - m_\mu^2} - \frac{\not{p} \not{\epsilon}^*}{u - m_\mu^2} \right) v(p_1) \right\}, \quad (3)$$

where G_F is the Fermi constant, α the fine-structure constant, V_{tq} the relevant CKM matrix elements and m_b the mass of the b quark. The \bar{B}_s^0 decay constant f_{B_s} is defined through

$$\langle 0 | \bar{s} \gamma^\mu \gamma_5 b | \bar{B}_s^0(p) \rangle = ip^\mu f_{B_s} X_f, \quad (4)$$

where $X_f = -1$ as defined in the PDG ⁶⁾ and FLAG ⁷⁾. The matrix elements are parameterized with four form factors function of the dilepton momentum transfer,

$$\begin{aligned} \langle \gamma(k, \lambda) | \bar{s} \gamma^\mu b | \bar{B}_s^0(q+k) \rangle &= e \epsilon^{\mu\lambda^* qk} \frac{F_V(q^2)}{M_{B_s}}, \\ \langle \gamma(k, \lambda) | \bar{s} \gamma^\mu \gamma_5 b | \bar{B}_s^0(q+k) \rangle &= ie (\lambda^{*\mu} qk - k^\mu \lambda^* q) \frac{F_A(q^2)}{M_{B_s}}, \\ \langle \gamma(k, \lambda) | \bar{s} \sigma^{\mu\nu} b q_\nu | \bar{B}_s^0(q+k) \rangle &= ie \epsilon^{\mu\lambda^* qk} F_{TV}(q^2, 0), \\ \langle \gamma(k, \lambda) | \bar{s} \sigma^{\mu\nu} \gamma_5 b q_\nu | \bar{B}_s^0(q+k) \rangle &= e (\lambda^{*\mu} qk - k^\mu \lambda^* q) F_{TA}(q^2, 0), \end{aligned} \quad (5)$$

with the shorthand $\epsilon^{\mu\lambda^* qk} \equiv \epsilon^{\mu\alpha\beta\delta} \lambda^{*\alpha} q^\beta k^\delta$. The amplitude for $B_s^0 \rightarrow \mu\mu\gamma$ can be obtained by substituting the CKM matrix elements and Wilson coefficients with their complex conjugate, and the form factors

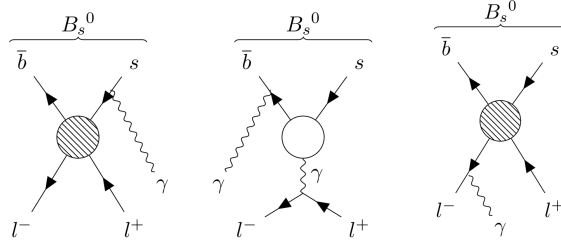


Figure 1: *Diagrams mediating the $B_s^0 \rightarrow \mu\mu\gamma$ decay. The two diagrams on the left are a sample for the “direct-emission” component, and the one on the right shows the bremsstrahlung component. Hatched circle is C_9/C_{10} , empty circle is C_7 .*

following

$$F_{V(TV)} \rightarrow -e^{-i\phi_{\text{CP}}} F_{V(TV)} , \quad F_{A(TA)} \rightarrow +e^{-i\phi_{\text{CP}}} F_{A(TA)} . \quad (6)$$

Finally, $C_9^{\text{eff}}(q^2)$ is defined by 8)

$$C_9^{\text{eff}}(q^2) = C_9(q^2) - \frac{9\pi}{\alpha^2} \bar{C} \sum_V |\eta_V| e^{i\delta_V} \frac{\hat{m}_V \mathcal{B}(V \rightarrow \mu^+\mu^-) \hat{\Gamma}_{\text{tot}}^V}{\hat{q}^2 - \hat{m}_V^2 + i\hat{m}_V \hat{\Gamma}_{\text{tot}}^V} . \quad (7)$$

$\mathcal{B}(V \rightarrow \mu^+\mu^-)$ and $\hat{\Gamma}_{\text{tot}}^V$ are respectively the branching fraction to two muons and total decay width of a vector meson V , and m_V their masses. The vector mesons under consideration are $\psi(2S)$, $\psi(3770)$, $\psi(4040)$, $\psi(4160)$ and $\psi(4415)$. These resonances are parameterized by a normalization factor $|\eta_V|$ and a phase δ_V to be varied later on, and $\bar{C} = C_1 + C_2/3 + C_3 + C_4/3 + C_5 + C_6/3$. A sample of the diagrams for each component is given in fig. 1.

We first consider Eqs. 2 and 3. The first remark of importance is that, when talking about the $B_s^0 \rightarrow \mu\mu\gamma$ decay, the amplitude of interest is the “direct-emission” contribution (Eq. 2). The reason is that the bremsstrahlung contribution is part of the $B_s^0 \rightarrow \mu\mu$ observable, after being resummed to all orders. Thus, when talking about “the $B_s^0 \rightarrow \mu\mu\gamma$ observable”, one really talks about the amplitude \mathcal{A}_{DE} . Of course, this requires to neglect the interference between the two amplitudes, but it has been proven to be several orders of magnitude smaller, and thus this assumption is perfectly safe⁹⁾. Second remark is that we do see a larger set of WCs related to $b \rightarrow s$ anomalies being probed compared to $B_s^0 \rightarrow \mu\mu$, C_9 and C_7 . The third remark is a trade-off: the additional photon lifts the helicity suppression of $B_s^0 \rightarrow \mu\mu$, thus partially compensating for the additional QED interactions. The differential and integrated branching fraction are thus not as small as two orders of magnitude lower than the $B_s^0 \rightarrow \mu\mu$ ones. However, this additional photon also adds a unavoidable and quite challenging task: the form factors associated to the $B_s^0 \rightarrow \gamma$ transition. In fact, one important aspect of the $B_s^0 \rightarrow \mu\mu$ decay is that it is a clean observable, with low uncertainty, but $B_s^0 \rightarrow \mu\mu\gamma$ does not benefit from such a “cleanliness”, because of the presence of such form factors, that are by nature functions emerging from non-perturbative QCD, and thus suffering from large errors in the absence of a sufficiently accurate method to calculate the relevant matrix elements non-perturbatively. Another source of hadronic uncertainty of great importance is contained in eq. 7. This shift to C_9 encapsulates the effect of charmonium resonances. In certain regions of the phase-space, the contribution to the amplitude from four quark operators are kinematically enhanced due to resonant states at particular q^2 values. These resonances are typically modeled by a sum over the considered states of Breit-Wigner poles, with two parameters η_V and δ_V that are poorly known, again due to the intrinsic

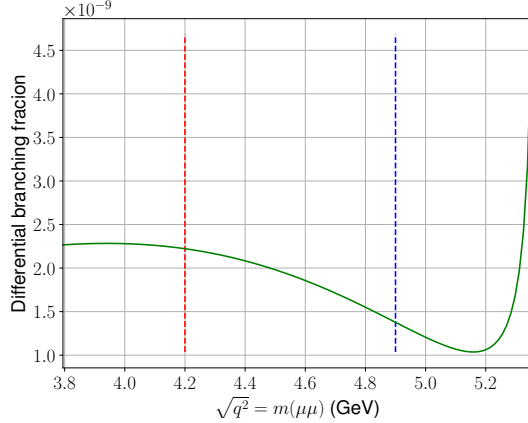


Figure 2: $B_s \rightarrow \mu\mu\gamma$ differential branching fraction with the dimuon mass $\sqrt{q^2} = M_B\sqrt{\hat{s}}$. Blue line: $q_{\min}^2 = (4.9 \text{ GeV})^2$ from the recent $B_s^0 \rightarrow \mu\mu$ analysis, red line: possible experimental limit at $q_{\min}^2 = (4.2 \text{ GeV})^2$. Theoretical prediction from `flavio` ¹³).

QCD nature of these phenomena. Both of these sources of uncertainties will be referred to as “hadronic uncertainties”.

The differential branching fraction (differential in q^2) of $B_s^0 \rightarrow \mu\mu\gamma$ is represented in fig. 2. We identify a peak close to the B_s^0 mass, corresponding to the bremsstrahlung component, and a component increasing when q^2 decreases which is the direct-emission component, and thus the one of interest. The form factors parametrization used here comes from a quark model ¹⁰). The blue vertical line at 4.9 GeV represents the lower mass cut in the dilepton invariant mass for the experimental analysis published by LHCb ¹¹) ¹²). This limit gives an integrated branching fraction of $\mathcal{B}(B_s^0 \rightarrow \mu\mu\gamma)_{[4.9;6.0]\text{GeV, DE}} = 1.92 \times 10^{-10}$, to be compared with the recent LHCb upper limit of $\mathcal{B}(B_s^0 \rightarrow \mu\mu\gamma)_{[4.9;6.0]\text{GeV, DE}} < 2.0 \times 10^{-9}$, an order of magnitude above. Thus, interestingly, the sensitivity is closing in on the SM prediction, and a measurement seems very likely with Run 3 data. Moreover, a dedicated analysis of $B_s^0 \rightarrow \mu\mu\gamma$ with a lower mass cut (represented by the red vertical line) would probe a much larger fraction of the phase-space, and thus the likeliness of measuring a signal.

With the context set up, we can now discuss the effective lifetime of a decay channel.

3 Effective lifetime, general case

3.1 Definition of the effective lifetime

First, we introduce the notations of the $B_s^0 - \bar{B}_s^0$ mixing,

$$|B_{L,H}\rangle = p|B_s^0\rangle \pm q|\bar{B}_s^0\rangle, \quad \Delta M_s = M_H - M_L, \quad \Gamma_s = \frac{\Gamma_H + \Gamma_L}{2}, \quad \Delta\Gamma_s = \Gamma_L - \Gamma_H, \quad (8)$$

with $M_{H,L}$ and $\Gamma_{L,H}$ the mass and total decay width of the $B_{L,H}$ states, $|q|^2 + |p|^2 = 1$. Considering the decay of a B_s^0 or \bar{B}_s^0 to a non-flavor specific final state f , a natural observable is the untagged decay rate

defined as

$$\langle \Gamma(B_s(t) \rightarrow f) \rangle \equiv \Gamma(B_s^0(t) \rightarrow f) + \Gamma(\bar{B}_s^0(t) \rightarrow f) = \int_{\text{PS}} (|\mathcal{A}_f(t)|^2 + |\bar{\mathcal{A}}_f(t)|^2) . \quad (9)$$

with $\Gamma(\overset{(-)}{B}_s^0(t) \rightarrow f)$ the time-dependent decay width of a B -meson which was a $\overset{(-)}{B}_s^0$ at $t = 0$, and $\overset{(-)}{A}_f(t)$ the corresponding time-dependent amplitudes, and where

$$\int_{\text{PS}, \mu\mu\gamma} = \frac{M_{B_s}}{2^8 \pi^3} \int_{\hat{s}_{\min}}^{\hat{s}_{\max}} \int_{\theta} f(\hat{s}, \hat{m}_\mu^2) d\hat{s} d\cos\theta, \quad \text{with } f(\hat{s}, \hat{m}_\mu^2) \equiv \frac{1 - \hat{s}}{2} \sqrt{1 - \frac{4\hat{m}_\mu^2}{\hat{s}}} . \quad (10)$$

This untagged decay rate is referred to as ‘‘natural’’ because it does not require tagging of the initial state, which can be a challenging task. It is related to the effective lifetime as

$$\tau_{\text{eff}}^f \equiv \frac{\int_0^\infty t \langle \Gamma(B_s(t) \rightarrow f) \rangle dt}{\int_0^\infty \langle \Gamma(B_s(t) \rightarrow f) \rangle dt} . \quad (11)$$

Working out the expression of $\langle \Gamma(B_s(t) \rightarrow f) \rangle$ as a function of the instantaneous amplitudes gives

$$\langle \Gamma(B_s(t) \rightarrow f) \rangle \propto \left[\cosh\left(\frac{y_s t}{\tau_s}\right) + A_{\Delta\Gamma_s}^f \sinh\left(\frac{y_s t}{\tau_s}\right) \right], \quad (12)$$

with $A_{\Delta\Gamma_s}^f$ defined as:

$$A_{\Delta\Gamma_s}^f = - \frac{\int_{\text{PS}} \text{Re}\left(q/p \bar{\mathcal{A}}_f \mathcal{A}_f^*\right)}{\int_{\text{PS}} |\mathcal{A}_f|^2}, \quad (13)$$

$y_s \equiv \Delta\Gamma_s / (2\Gamma_s) \approx 0.06$, $\overset{(-)}{A}_f$ the instantaneous amplitudes of decay of $\overset{(-)}{B}_s^0$.

Finally, $A_{\Delta\Gamma_s}^f$ is related to the effective lifetime τ_{eff}^f by

$$\tau_{\text{eff}}^f = \frac{\tau_s}{1 - y_s^2} \left(\frac{1 + 2A_{\Delta\Gamma_s}^f y_s + y_s^2}{1 + A_{\Delta\Gamma_s}^f y_s} \right) . \quad (14)$$

Thus, τ_{eff}^f is related to the quantity $A_{\Delta\Gamma_s}^f$ via eq. 14, and we will use $A_{\Delta\Gamma_s}^f$ in place of τ_{eff}^f in the rest of this work by using eq. 13, which immediately gives $A_{\Delta\Gamma_s}^f$ as a function of the instantaneous amplitudes.

3.2 Motivation for studying $A_{\Delta\Gamma_s}^{\mu\mu\gamma}$

We will now fix $f = \mu\mu\gamma$ and discuss eq. 13 to justify several points that were anticipated in the introduction. First, $A_{\Delta\Gamma_s}^{\mu\mu\gamma}$ is *by definition* a ratio-of-amplitudes observable, for the numerator and denominator are phase-space integrated ‘‘squares of amplitudes’’, which leads to expecting a partial cancellation of the theoretical errors. Then, the dependencies on the amplitudes are different between numerator and denominator; $|\mathcal{A}_f|^2$ is proportional to $|C_9|^2$ or $|C_{10}|^2$, whereas $\mathcal{A}_f \bar{\mathcal{A}}_f^*$ is proportional to $(C_9)^2$ and $(C_{10})^2$. Then, if one or several WCs have a complex phase, the latter will manifest itself in the numerator and not in the denominator. Knowing that in the SM the WCs are real numbers, a deviation of $A_{\Delta\Gamma_s}^{\mu\mu\gamma}$ from the SM prediction would indicate non-standard CP violation in the form of complex phases of the WCs. Finally, it is worth mentioning that the complex phase of the CKM matrix elements that would appear in the product $\mathcal{A}_f \bar{\mathcal{A}}_f^*$ cancels with the complex conjugate phases coming from the ratio q/p , which confirms that a complex phase emerging in this ratio *has to* come from non-standard CP violation.

Now that the observable $A_{\Delta\Gamma_s}^{\mu\mu\gamma}$ has been defined and discussed, we can turn to the numerical analysis. In this work we will focus on the high- q^2 region.

4 Numerical results for $A_{\Delta\Gamma_s}^{\mu\mu\gamma}$ in the high- q^2 region

4.1 Method

The objective of this section is to study the sensitivity of $A_{\Delta\Gamma_s}^{\mu\mu\gamma}$ to different NP scenarios currently allowed by data. Equally, we expect the errors to be “scenario-dependent”. To do so, several benchmark points are obtained by performing global fits to current data.

Scenario	C_9^{NP}	C_{10}^{NP}
SM	0	0
C_9	$-1.0 - 0.9i$	0
C_{10}	0	$1.0 + 1.4i$
C_{LL}	$-0.7 - 1.4i$	$0.7 + 1.4i$
SM values	$C_9 = 4.327$	$C_{10} = -4.262$

(15)

Each point corresponds to a “NP scenario”, meaning a single coefficient is left free in the fit (for example, in the C_9 scenario, C_9 is the only free coefficient), with the C_{LL} scenario having the constraint $C_9^{\text{NP}} = -C_{10}^{\text{NP}}$. An important note here is that each WC corresponds to *two parameters*; real and imaginary parts.

With these given scenarios, we can obtain the central value of $A_{\Delta\Gamma_s}^{\mu\mu\gamma}$ for each scenario using eq. 13. Now we discuss the computation of the hadronic uncertainties.

Concerning the form factors, in this work, we use the recent parametrization ¹⁴⁾, published with central values, errors and correlations for each of the four form factors $F_{V,A,TV,TA}$. We sample errors in the given interval for each form factor and compute $A_{\Delta\Gamma_s}^{\mu\mu\gamma}$, before taking the 3σ error.

Concerning the charmonium resonances, we conservatively perform a scan in the two intervals $|\eta_V| \in [1, 3]$ and $\delta_V \in [0, 2\pi)$ with a flat distribution. The former interval is chosen to encapsulate $|\eta_V| = 1$ (which is the naive factorization result) and $|\eta_V| = 2.55$ which was seen to describe well the $b \rightarrow s\ell\ell$ transitions ¹⁵⁾. The latter reflects the poor knowledge of the phases of such resonances ¹⁶⁾ and is therefore scanned over all possible values in the most conservative way.

4.2 Numerical results

We now turn to the numerical results on fig. 3. We compute $A_{\Delta\Gamma_s}^{\mu\mu\gamma}$ as a function of the lower bound of integration \hat{s}_{\min} as defined in the phase-space integral in eq. 10 (with \hat{s}_{\max} set to 1). The blue band corresponds to the 3σ uncertainty coming from form factors parametrization, and the yellow band from the modeling of charmonium resonances. The immediate conclusion is that the uncertainty due to form factors is still quite large: we don’t observe a cancellation as efficient as can be seen in other ratio-of-amplitudes squared observables. However, the uncertainty coming from the charmonium resonances is safely well below 1%, which can be traced back to two factors: first, because we are talking about resonances, by definition they are located in a limited kinematic region of the spectrum, and thus have less influence on phase-space integrated quantities. The second factor is a bit more subtle, the shift from eq. 7 leads to a cancellation of this error because the kinematic structures in front of said shift are similar between numerator and denominator. This particular feature resembles the origin of the cancellation in R_{K/K^*} , and boils down to the ratio-of-amplitudes squared property of $A_{\Delta\Gamma_s}^{\mu\mu\gamma}$. This cancellation is very welcome, since progress on the form factors can be made (most notably from Lattice QCD), but the same progress is unrealistic in the description of charmonium resonances. Thus, having such a small influence from the latter with very conservative assumptions is a particularly nice property. Finally, even though

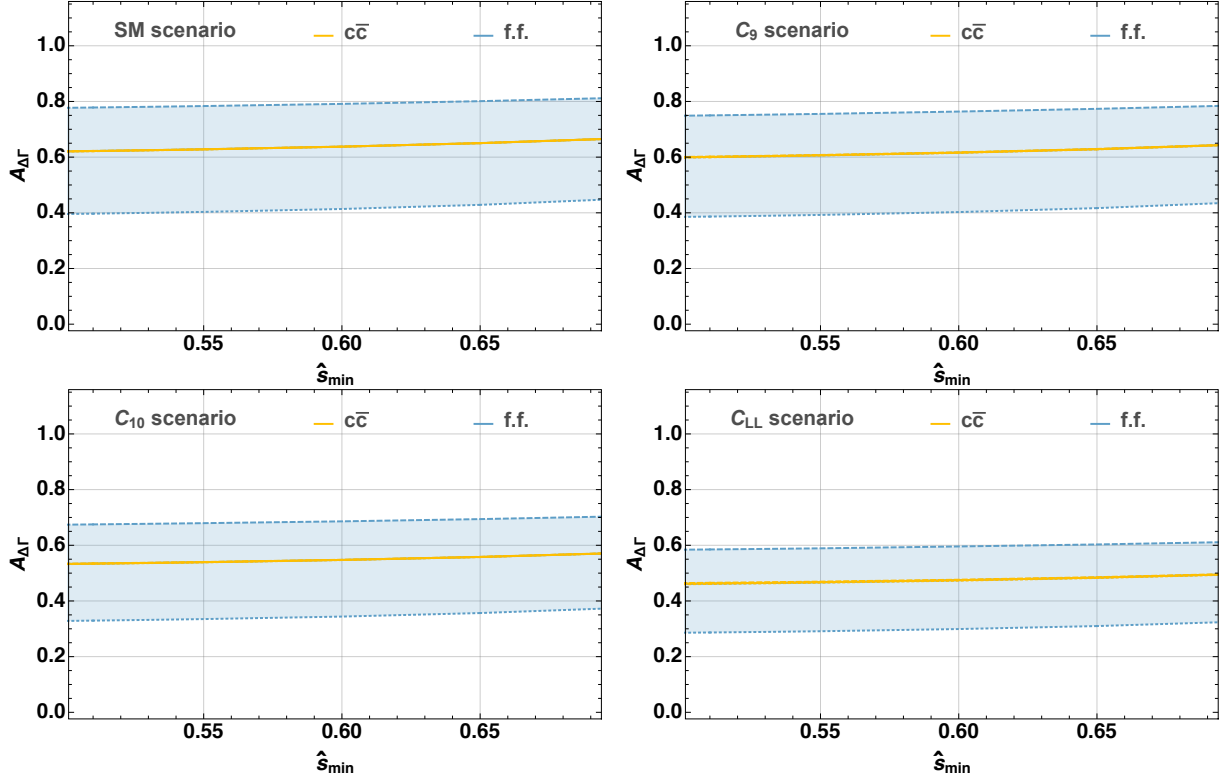


Figure 3: $A_{\Delta\Gamma_s}^{\mu\mu\gamma}$ prediction in the kinematic interval $[\hat{s}_{\min}, 1]$. The blue vs. yellow bands refer to the f.f. error, and respectively on the uncertainty associated to the modelling of broad-charmonium resonances. Each plot correspond to a scenario mentioned in the upper left corners.

the current status disallows one to distinguish between the scenarios, we see that, for example between the SM and C_{LL} scenarios, the central values are separated enough that reduced form factor uncertainties can rapidly reach a 3σ discrepancy between them.

5 Conclusion

This work puts into light a new observable, the effective lifetime $\tau_{\text{eff}}^{\mu\mu\gamma}$ of the $B_s^0 \rightarrow \mu\mu\gamma$ decay, related to ratio-of-amplitudes squared observable noted $A_{\Delta\Gamma_s}^{\mu\mu\gamma}$. This observable is sensitive to an under-explored area of possible NP, which is non-standard CP violation i.e. not aligned with the SM. After setting 4 benchmark scenarios, we evaluate the sensitivity of $A_{\Delta\Gamma_s}^{\mu\mu\gamma}$ to not be enough to distinguish these scenarios looking at the current status of the form factors uncertainty. However, a very potent cancellation of the charmonium resonances uncertainties takes effect in this ratio, where progress would be the most difficult. Finally, we stress that LQCD has taken an interest in the computation of radiative form factors of heavy mesons decays in the high- q^2 region, which coincides with the region of experimental interest. These two coinciding aspects make the future of this type of decay and of observable quite interesting.

6 Acknowledgements

The author would like to thank Diego Guadagnoli for a careful reading of this manuscript, as well as for his guidance during this work. A special thank is also owed to the organizing committee of the XX

Bruno Touschek Summer School at LNF for the opportunity to share this work.

References

1. R. Aaij et al., *Nature Phys.* 18 (2022) 277. doi: 10.1038/s41567-021-01478-8. arXiv: 2103.11769 [hep-ex]
2. R. Aaij et al., *Phys. Rev. Lett.* 128 (2022) 191802. doi: 10.1103/PhysRevLett.128.191802. arXiv: 2110.09501 [hep-ex]
3. A. Carvunis, F. Dettori, S. Gangal, D. Guadagnoli and C. Normand, *J. High Energ. Phys.* 2021, 12 (2021). doi: 10.1007/JHEP12(2021)078. arXiv: 2102.13390 [hep-ph]
4. D. Guadagnoli, M. Reboud and R. Zwicky, *J. High Energ. Phys.* 2017, 184 (2017). doi: 10.1007/JHEP11(2017)184. arXiv: 1708.02649 [hep-ph].
5. A. Kozachuk, D. Melikhov and N. Nikitin, *Phys. Rev. D* 97 (2018) 053007. doi: 10.1103/PhysRevD.97.053007. arXiv: 1712.07926 [hep-ph].
6. Particle Data Group collaboration, P. A. Zyla et al., *PTEP* 2020 (2020) 083C01. doi: 10.1093/ptep/ptaa104
7. Flavour Lattice Averaging Group collaboration, S. Aoki et al., *Eur. Phys. J. C* 80 (2020) 113. doi: 10.1140/epjc/s10052-019-7354-7. arXiv: 1902.08191 [hep-lat].
8. F. Kruger and L. M. Sehgal, *Phys. Lett. B* 380 (1996) 199–204. doi: 10.1103/PhysRevD.97.053007. arXiv: 9603237 [hep-ph]
9. F. Dettori, D. Guadagnoli and M. Reboud, *Phys. Lett. B* 768 (2017) 163–167. doi: 10.1016/j.physletb.2017.02.048. arXiv: 1610.00629 [hep-ph].
10. F. Kruger and D. Melikhov, *Phys. Rev. D* 67 (2003), p. 034002. doi: 10.1103/PhysRevD.67.034002. arXiv: hep-ph/0208256 [hep-ph]
11. R. Aaij et al., *Phys. Rev. Lett.* 128 (2022) 191802. doi: 10.1103/PhysRevLett.128.041801. arXiv: 2108.09284 [hep-ex]
12. R. Aaij et al., *Phys. Rev. D* 105 (2022) 012010. doi: 10.1103/PhysRevD.105.012010. arXiv: 2108.09283 [hep-ex]
13. D. M. Straub, arXiv: 1810.08132 [hep-ph]
14. T. Janowski, B. Pullin and R. Zwicky, *J. High Energ. Phys.* 2021, 8 (2021). doi: 10.1007/JHEP12(2021)008. arXiv: 2106.13616 [hep-ph]
15. J. Lyon and R. Zwicky, arXiv: 1406.0566 [hep-ph].
16. BES collaboration, M. Ablikim et al., *eConf C070805* (2007) 02. arXiv: 0705.4500 [hep-ex].

STRANGE PARTICLE PRODUCTION IN p Pb COLLISIONS AT THE LHCb EXPERIMENT

Clara Landesa Gómez
IGFAE USC, Xoaquín Díaz de Rábago, 15782, Santiago de Compostela, Spain

Abstract

The study of strangeness in high-energy collisions is of great interest, as the enhanced production of strange quarks is one of the possible signatures of the formation of a Quark Gluon Plasma. In small systems, such as proton-lead collisions, there are other mechanisms that might lead to this enhancement. By studying p Pb collisions we can gain insight into both initial-state and final-state effects that may affect the formation of hadrons with strange quarks. This work uses LHC data from p Pb collisions at 5.02 TeV collected at the LHCb experiment. The LHCb acceptance allows exploring strange particle production in unexplored kinematic regimes. The first object of study will be the ϕ meson on grounds of its inherent interest as a probe for QCD phases and its relatively high-production rate.

1 Introduction

The study of high-energy heavy ion collisions is primarily motivated by the search for a rare state of matter known as the Quark Gluon Plasma (QGP). In this state the individual components of mesons and baryons, quarks and gluons, manifest as free particles. Theoretical predictions ¹⁾ and experimental observations ^{2, 3)} seem to agree that it is possible to reach this colour deconfinement in the laboratory when colliding large systems, such as Pb ions, due to the high temperatures and densities reached. The study of heavy-ion collisions at LHC energies provides new opportunities to determine the properties of the QGP ⁴⁾. The interest in the QGP resides largely in the fact that it is predicted to have been formed microseconds after the Big Bang and to constitute the inner core of neutron stars ⁵⁾.

The enhancement of the production of hadrons with strange valence quarks with respect to light hadrons in heavy-ion collisions has long been considered a probe of the QGP ⁶⁾. Only in collisions with a high number of participating nucleons (participants) is the density high enough to produce the

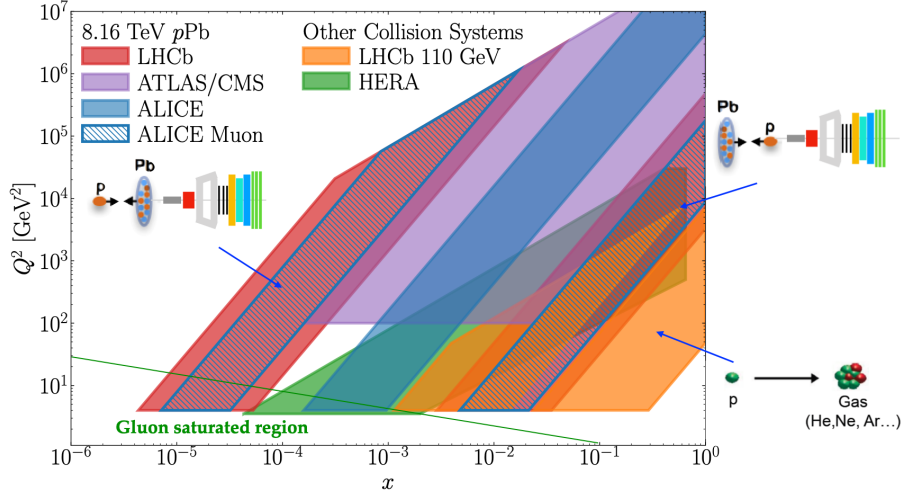


Figure 1: *Kinematic coverage of LHCb and other experiments for forward and backward collisions in terms of the fractional momentum, x , of the nucleon in the target and the squared parton-parton invariant mass, Q^2 . The LHCb acceptance in fixed target mode, where the proton beam collides with ions of a gas at rest in the laboratory, is also included in the figure for completeness.*

QGP. In a collision of two heavy ions, the charged particle multiplicity is highly correlated to the number of participants ⁷⁾, so a strangeness enhancement with multiplicity can be associated with plasma production.

However, in recent experimental results, this enhancement has been observed in smaller collision systems such as proton-Lead (pPb) and proton-proton (pp) ⁸⁾, in which the reached energy density is not expected to be sufficient to give rise to a QGP. Other possible mechanisms, such as string fusion ⁹⁾ or colour reconnection ¹⁰⁾, might explain the increase in strange-particle production. This puts into question whether the strangeness enhancement previously observed in AuAu and PbPb collisions at SPS, RHIC and LHC ^{11, 12, 13, 14)} can be fully justified with plasma formation. In fact, modern rope hadronisation models have achieved to reproduce this strangeness enhancement behaviour in all kinds of collision systems ¹⁵⁾.

One of the goals of this work is to measure the evolution of strangeness with multiplicity in LHCb for pPb collisions. These measurements would be complementary to those of the ALICE collaboration for pPb collisions ^{16, 17)}, that cover a different kinematic regime. While ALICE has only got coverage for the measurement of most strange particles at mid-rapidity, the LHCb experiment has a very unique geometry, measuring in the high pseudorapidity region $2 < \eta_{\text{lab}} < 5$. In pPb collisions, if the proton beam points towards the LHCb arm the collision is called *forward*. If the Lead does, it is called *backward*. Following the usual convention, the forward configuration is taken as positive values of pseudorapidity in the nucleon-nucleon centre of mass system, η_{cms} . Different pseudorapidity regions correspond to different values of fractional momentum $x \sim Q^2 \cdot e^{-\eta} / \sqrt{s_{\text{NN}}}$, where Q^2 is the square of the exchanged momentum between the incoming and outgoing parton. In Figure 1 the kinematic coverage of LHCb for both configurations is shown in the (x, Q^2) plane. Measuring a strangeness enhancement at forward rapidities ($\eta_{\text{cms}} > 2$) that is universal across collision systems could also contribute to solve the *Muon Puzzle* in cosmic-ray induced showers ¹⁸⁾.

By studying $p\text{Pb}$ collisions we can also obtain information about the differences between the properties of nuclear matter and those of non-interacting baryons. Since the QGP is not expected, any differences with pp should be explained through the so-called Cold Nuclear Matter (CNM) effects. In the forward low- x region, a CNM effect known as nuclear shadowing¹⁹⁾ is expected to be at play according to predictions based on nuclear parton distribution functions as nCTEQ15²⁰⁾. Consequently, a deficit of s quarks produced with respect to pp collisions should be observed. In the backward region, the opposite effect, nuclear anti-shadowing, is predicted, resulting in an excess of strangeness with respect to pp .

The $\phi(1020)$ meson will be the first particle object of study. It is abundantly produced in hadronic collisions as it is the lightest bound state of strange quarks, with $s\bar{s}$ valence quarks. This will allow for good accuracy in its measurements. Besides, the differences in production mechanisms between regular hadronic matter and QGP make it a perfect QGP probe. In elementary collisions, its production is suppressed because of the Okubo-Zweig-Iizuka (OZI) rule.¹ In a QGP, ϕ mesons can be produced through the coalescence of s quarks, bypassing the OZI rule²¹⁾.

2 The LHCb experiment and its heavy ion physics programme

The LHCb experiment was conceived to study heavy flavour physics at the LHC²²⁾. Its main goal is to look for indirect evidence of new physics in CP violation and rare decays of beauty and charm hadrons. It is a single-arm spectrometer with a forward angular coverage from approximately 10 to 300 mrad in the bending plane (10 to 250 mrad in the non-bending plane).

LHCb is composed of several subdetectors. The LHCb tracking system consists of the VERteX LOcator system (VELO) and four planar tracking stations. The VELO provides precise measurements of track coordinates close to the interaction region. Particle identification in LHCb is provided by four different detectors: the calorimeter system, the two RICH stations (that use Cherenkov radiation) and the muon stations.

Heavy ion physics was not among the original purposes of the experiment. However, the features of the detector make it exceptionally suitable also for this field²³⁾: the forward acceptance, complementary to other LHC experiments; the excellent reconstruction performance for exclusive heavy flavour states down to almost null transverse momentum, distinguishing particles produced in the primary vertex from those coming from hadron decays; and the possibility to operate the detector in fixed target mode, for which the forward geometry of the detector is very well suited.

3 Objectives

In the following, the observables to be used in order to characterise strangeness productions in $p\text{Pb}$ collisions are described. The goal is to obtain them for all the particles of interest, starting with the ϕ mesons. It would also be interesting to extend the analysis to additional strange hadrons, such as $K^*(892)^0$ meson and Λ , Ξ and Ω baryons.

The nuclear modification factor is the most common variable used to study the production differences between pp and $p\text{Pb}$ and therefore calibrate CNM effects²⁴⁾. In terms of the centre-of-mass

¹The OZI rule states that processes with disconnected quark lines in the initial and final state are suppressed. In other words, if a certain process can be cut in two by slicing only gluonic lines (and not cutting open any external particles), the process is suppressed. This rule also explains why the ϕ meson's preferred decay channel is the $\phi \rightarrow K^+K^-$.

pseudorapidities η_{cms} and the transverse momenta p_T , it is defined as

$$R_{p\text{Pb}}(\eta_{\text{cms}}, p_T) = \frac{1}{A} \frac{d^2\sigma_{p\text{Pb}}}{d\eta_{\text{cms}}dp_T} / \frac{d^2\sigma_{pp}}{d\eta_{\text{cms}}dp_T}, \quad (1)$$

where $A = 208$ is the mass number of lead and $d^2\sigma_{p\text{Pb}(pp)}/dp_Td\eta$ are the production double differential cross-sections for the particle of study in $p\text{Pb}$ (pp) collisions. They can be obtained as

$$\frac{d^2\sigma}{dp_Td\eta_{\text{cms}}} = \frac{1}{\mathcal{L}} \frac{N_S(\eta_{\text{cms}}, p_T)}{\Delta p_T \Delta \eta_{\text{cms}}}, \quad (2)$$

where N_S is the number of strange particles produced in a given range of (η_{cms}, p_T) . Δp_T and $\Delta \eta_{\text{cms}}$ are the sizes of the bins, and \mathcal{L} is the integrated luminosity value of the corresponding data set.

The forward-backward ratio,

$$R_{\text{FB}}(|\eta_{\text{cms}}|, p_T) = \frac{d^2\sigma_{p\text{Pb}}}{d\eta_{\text{cms}}dp_T} / \frac{d^2\sigma_{\text{Pb}p}}{d|\eta_{\text{cms}}|dp_T}, \quad (3)$$

does not require the pp data in order to be calculated. Here, $\sigma_{p\text{Pb}}$ and $\sigma_{\text{Pb}p}$ represent the forward and backward cross-sections, respectively. The ratio is obtained for the double differential cross sections in pseudorapidity bins with the same module and opposite signs. It measures the consequences of CNM effects on rapidity regions that would be geometrically equivalent in symmetric collisions. This quantity is relevant at non-central rapidities.

In order to study the evolution of strangeness production with multiplicity the following yields are calculated

$$\text{Yield}(N_{\text{VELO}}, \eta_{\text{cms}}, p_T) = N_{\text{ev}}^{-1} \frac{N_S(\eta_{\text{cms}}, p_T)}{\Delta p_T \Delta \eta_{\text{cms}}}, \quad (4)$$

where N_{VELO} are the number of tracks reconstructed by the VELO detector, used to measure multiplicity, and N_{ev} is the number of events within a multiplicity bin. One of the main challenges of this analysis is to find a proxy for the charged particle multiplicity of the collision, which is necessary to measure the evolution of strangeness with multiplicity. As a first approach, N_{VELO} were used, as in ²⁵⁾, because of the VELO's high tracking efficiency ²⁶⁾. However this variable is not perfect as some tracks reconstructed by the VELO come from secondary interactions with the detector. An in-depth study of the charged particle multiplicity determination is necessary to guarantee that the results are universal and can be compared to other collaborations as well as phenomenological predictions.

4 Analysis strategy

The $p\text{Pb}$ collision data used for this analysis were taken at a centre of mass energy $\sqrt{s_{\text{NN}}} = 5.02$ TeV and acquired at the end of the LHC Run 1 in February 2013. The average instantaneous luminosity during the data taking was $\mathcal{L} = 3 \cdot 10^{27} \text{ cm}^{-2} \text{ s}^{-1}$ and the corresponding total integrated luminosity, calculated by integrating in time, was $\int \mathcal{L} = 1.7 \text{ nb}^{-1}$.

The first particle chosen for this analysis is the lightest of the hidden-flavour vector mesons, the ϕ meson. The mass and width of the ϕ resonance, as tabulated by the PDG ²⁷⁾, are $M_\phi = (1019.461 \pm 0.016) \text{ MeV}/c^2$ and $\Gamma_\phi = (4.249 \pm 0.013) \text{ MeV}/c^2$.

Since it is a neutral short-lived resonance, the reconstruction of the ϕ meson signal is done by identifying its decay products. To profit from a large amount of data, this is done through the preferred decay channel $\phi \rightarrow K^+K^-$, which has the most significant branching ratio $\text{BR}_{K^+K^-} = 49.2 \pm 0.5\%$ ²⁷⁾. The kaon pair's response in the detector results in two oppositely-charged tracks.

The data considered for the study of the ϕ mesons were collected from a minimum bias sample² in order to measure the forward-backward ratio (Eq. 3). This sample is divided into bins of N_{VELO} for the multiplicity-dependent measurement (Eq. 4). With the purpose of identifying the ϕ meson-candidates from all the combinations of two charged tracks, some selections are implemented. The tracks are required to be reconstructed with a certain fit quality and to fulfil some kinematic requisites. Besides, a particle identification selection is performed through a variable that identifies kaons using machine learning techniques²⁸). This variable takes values from 0 to 1, with 1 being the highest likelihood for the track to be a kaon. For the construction of this variable, the information recorded by all the LHCb subdetectors is fed to a deep neural network algorithm. In the measurement of the forward-backward ratio, the candidates are divided into bins of p_{T} and η_{cms} .

Following the selection, the production rate of the ϕ mesons is measured by performing a simple fit to the invariant mass of the K^+K^- candidates. The invariant mass of the correlated kaon pairs coming from a ϕ is distributed in a Breit-Wigner signal with mean value and width equal to the mass and the width of the ϕ meson. Uncorrelated kaons and misidentified particles (mostly pions and protons) will form a combinatorial background dominated by the two-particle Lorentz invariant phase space. After determining the signal and applying corrections that account for effects such as the inefficiency of the detector and its limited acceptance, the final number of produced particles (N_S) is obtained. With it, other observables can be measured.

So far there has been some progress in the study of the forward-backward ratio and the production with multiplicity. For the latter, three different multiplicity classes, or N_{VELO} bins, were considered: low, with 70% of minimum bias events with the lower number of N_{VELO} tracks; medium, with 15% of events, and high multiplicity, with 5% of events. For forward (backward) collisions, these classes are equivalent to the following N_{VELO} intervals: [19,126] ([16,156]), [127,186] ([157,250]), [187,1238] ([251,1584]).

Several important tasks are presently ongoing to complete this analysis. For instance, further improvement of the selection requirements will be necessary to get rid of the contribution from non-prompt ϕ mesons. Prompt particles are those particles generated directly from the partons of the nuclear matter and are the main interest, while non-prompt mainly come from decays. In addition, all the possible sources of systematic errors have to be accounted for.

5 Conclusion and future prospects

The study of the production of ϕ mesons seems promising based on the data sample size. Aside from the aforementioned necessary tasks that ought to be carried out to obtain final results, there are other observables of interest to characterise the strangeness production in $p\text{Pb}$ collisions. Measuring the nuclear modification factor $R_{p\text{Pb}}$, which requires the study of the pp data sample, would contribute to probing into CNM effects such as nuclear shadowing.

In order to complete the characterisation of the strangeness evolution with multiplicity, an alternative to the number of VELO tracks as a proxy for the number of charged particles could be considered. Measuring particles with different levels of strangeness (strange valence quarks) and computing production ratios would also help quantify a strangeness enhancement with multiplicity. The $K^*(892)^0$ meson, with $d\bar{s}$ valence quarks, has a considerably shorter lifetime, so it is expected that its decay products will be more affected by re-scattering in the medium. Comparing the production to ϕ mesons can help gain

²A minimum bias sample goes through a filter that reduces the amount of data but aims at not having any preferred event feature, selecting every event where a $p\text{Pb}$ interaction occurs. A minimal event selection is implemented by requiring a single reconstructed primary vertex.

an understanding of the extension of the hadronic fireball created in the p Pb collision²⁹). The $\Omega^-/\bar{\Omega}^+$ baryon ($sss/\bar{s}\bar{s}\bar{s}$) is of considerable interest as it has the highest level of strangeness. The $\Lambda/\bar{\Lambda}$ ($uds/\bar{u}\bar{d}\bar{s}$) and $\Xi^-/\bar{\Xi}^+$ ($dss/\bar{d}\bar{s}\bar{s}$) baryons could also be studied for completeness. If a measurement of charged pions were performed in parallel, the ratio of yields to pions would be the most suitable observable to analyse.

References

1. L. D. McLerran, Rev. Mod. Phys. **58**, 1021-1064 (1986)
2. D. Teaney, J. Lauret and E. V. Shuryak, Phys. Rev. Lett. **86**, 4783-4786 (2001)
3. E. V. Shuryak, Nucl. Phys. A **750**, 64-83 (2005)
4. Z. Citron *et al*, Report from Working Group 5: Future physics opportunities for high-density QCD at the LHC with heavy-ion and proton beams, in: HL/HE-LHC Workshop, CERN Yellow Rep. Monogr. **7**, 1159-1410 (2019)
5. K. Rajagopal and F. Wilczek, The Condensed matter physics of QCD, in: At The Frontier of Particle Physics: Handbook of QCD (In 3 Volumes) 2061-2151 (2001)
6. P. Koch *et al* Phys. Rept. **142**, 167-262 (1986)
7. M. L. Miller *et al* Ann. Rev. Nucl. Part. Sci. **57**, 205-243 (2007)
8. The ALICE Collaboration, Nature Phys. **13** 553–539 (2017)
9. N. Armesto, M. A. Braun, E. G. Ferreira and C. Pajares, Phys. Lett. B **344**, 301-307 (1995)
10. J. R. Christiansen and P. Z. Skands, JHEP **08**, 003 (2015)
11. F. Becattini and J. Manninen, J. Phys. G **35**, 104013 (2008)
12. The PHENIX Collaboration, Nucl. Phys. A **757**, 184-283 (2005)
13. The STAR Collaboration, Nucl. Phys. A **757**, 102-183 (2005)
14. The ALICE Collaboration, Phys. Lett. B **728**, 216-227 (2014) [erratum: Phys. Lett. B **734**, 409-410 (2014)]
15. C. Bierlich *et al* “Strangeness enhancement across collision systems without a plasma,” [arXiv:2205.11170 [hep-ph]] (2022)
16. The ALICE Collaboration, Phys. Lett. B **758**, 389-401 (2016)
17. The ALICE Collaboration, Phys. Lett. B **728**, 25-38 (2014)
18. J. Albrecht *et al*. Astrophys. Space Sci. **367** no.3, 27 (2022)
19. N. Armesto, J. Phys. G **32**, R367-R394 (2006)
20. K. Kovarik, A. Kusina, T. Jezo, D. B. Clark, C. Keppel, F. Lyonnet, J. G. Morfin, F. I. Olness, J. F. Owens and I. Schienbein, *et al*. Phys. Rev. D **93**, no.8, 085037 (2016)
21. A. Shor, Phys. Rev. Lett. **54**, 1122-1125 (1985)

22. The LHCb Collaboration, JINST **3**, S08005 (2008)
23. O. Boente García, Results from proton-lead and fixed-target collisions at LHCb, in: 27th International Workshop on Deep Inelastic Scattering and Related Subjects (Torino, Italy, April 8-12, 2019) PoS DIS2019 **352** (2019)
24. The LHCb Collaboration *et al*, Phys. Rev. Lett. **128** no.14, 142004 (2022)
25. The LHCb Collaboration, Phys. Rev. Lett. **126** no.9, 092001 (2021)
26. The LHCb Collaboration, JINST **9**, P09007 (2014)
27. P.A. Zyla *et al.* (Particle Data Group), Prog. Theor. Exp. Phys. **2020**, 083C01 (2020)
28. D.Derkach *et al*, Machine-Learning-based global particle-identification algorithms at the LHCb experiment, in: 18th International Workshop on Advanced Computing and Analysis Techniques in Physics Research (Seattle, WA, USA, August 21-25, 2017) J. Phys.: Conf. Ser. **1085** 042038
29. The ALICE collaboration, Eur. Phys. J. C **76**, no.5, 245 (2016)

STRANGENESS PRODUCTION IN THE NA61/SHINE EXPERIMENT AT THE CERN SPS ENERGY RANGE

Yuliia Balkova for the NA61/SHINE collaboration
University of Silesia, 12 Bankowa str., 40-007 Katowice, Poland

Abstract

NA61/SHINE is a multi-purpose fixed-target experiment located at the CERN Super Proton Synchrotron. One of the main goals of the experiment is to study the phase transition between the hadronic gas and quark-gluon plasma and search for the critical point of the strongly interacting matter. To study the phase diagram of strongly interacting matter, the NA61/SHINE experiment performed the two-dimensional scan in collision energy and system size.

In turn, strangeness production is a well-known valuable probe for understanding particle production in high-energy physics because of the absence of the strange valence quarks in the initial state of the collision. The talk will emphasize the importance of measuring the strangeness production for the discussion concerning the onset of deconfinement and present the general strategy of the analysis.

1 Introduction

For decades now, the main motivation driving the high-energy heavy-ion physics community, which is present at various accelerators across the world (e.g. Super Proton Synchrotron, Relativistic Heavy Ion Collider and Large Hadron Collider), is the study of properties of quark-gluon plasma (QGP). It is a deconfined state of strongly interacting matter consisting of quasi-free quarks and gluons, which is believed to exist just microseconds after the Big Bang. Hence, recreating this state in the laboratory is of great importance in order to understand the evolution of the Early Universe. The phase diagram of strongly interacting matter summarising the theoretical predictions and experimental results is shown in Figure 1 in terms of baryonic chemical potential and temperature.

An idea of strangeness enhancement indicating the phase transition between the hadron gas and quark-gluon plasma was formulated a long ago ²⁾. Models assuming the occurring phase transition, particularly the Statistical Model of the Early Stage ³⁾, predicted a sharp maximum in the ratio of the multiplicities of strange hadrons the ones of pions, as shown in Figure 2. Typically, the multiplicity

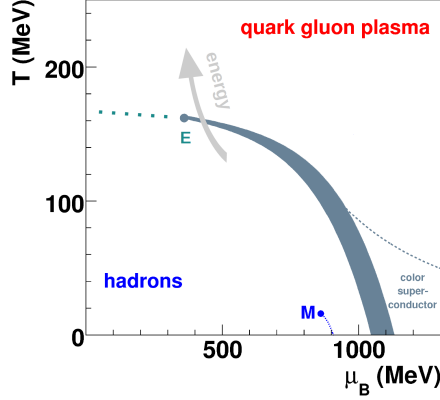


Figure 1: *Phases of strongly interacting matter. Point M is the critical point of the nuclear liquid-gas phase transition. The shaded band shows the 1st order phase boundary between the hadron and quark-gluon plasma phase, which is expected to end in a critical endpoint E. At point E, the sharp phase transition turns into a rapid crossover, indicated as the dotted line ¹⁾.*

of strange hadrons is experimentally described as the multiplicity of positively charged kaons, as it is assumed that up to half of the strangeness produced in the course of the collision is carried by the kaons. However, the assumption needs to be verified by measurement of other hadrons containing the strange quark, namely Λ and $\bar{\Lambda}$ hyperons.

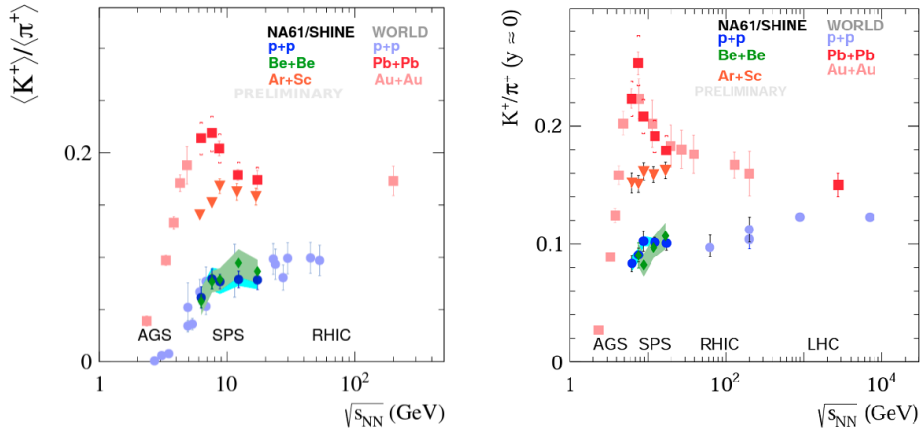


Figure 2: *$\langle K^+ \rangle / \langle \pi^+ \rangle$ ratio in full 4π phase space (left) and the $\langle K^+ \rangle / \langle \pi^+ \rangle$ ratio at mid-rapidity (right) as a function of collision energy for $p+p$, $Be+Be$, $Ar+Sc$ and $Pb+Pb/Au+Au$ collisions ⁴⁾.*

2 NA61/SHINE detector

NA61/SHINE is a fixed-target experiment situated at the H2 beamline of the CERN North Area and takes its beams from the CERN Super Proton Synchrotron (SPS) ⁵⁾. It is one of the experiments aiming at investigating the onset of deconfinement. The experimental tool to study this effect is the

two-dimensional scan of the collision energy and system size performed by the NA61/SHINE. The layout of the NA61/SHINE detector is shown in Figure 3.

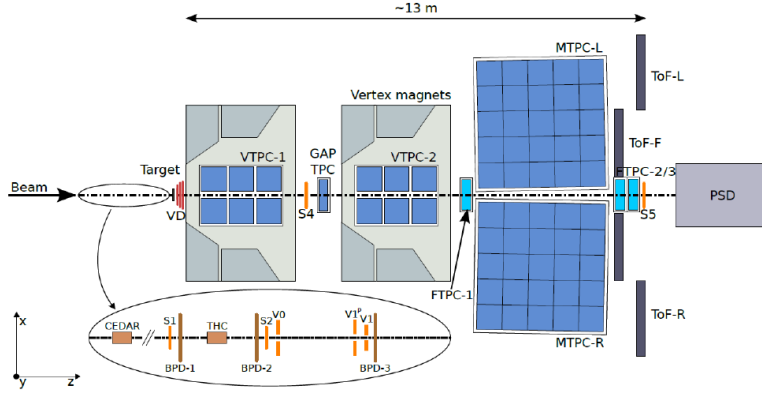


Figure 3: *Schematic view of the NA61/SHINE detector system.*

A set of beam position detectors upstream of the target provides precise information about the trajectory and composition of incoming beam particles. Charged particle identification and momentum measurements are then performed by a set of Time Projection Chambers, two of which are located in the magnetic field of super-conducting dipole magnets, and a set of Time-of-Flight detectors. Particularly, the particle identification performed in the TPCs is based on measurements of the specific energy loss (dE/dx) in the chamber gas. The Projectile Spectator Detector (PSD), a high-resolution forward calorimeter, measures the energy of spectators, which is related to the centrality of a collision.

3 Analysis strategy and expected outcome

3.1 General research plan

The proposed project aims to extend the study of strange hyperon production to the Ar+Sc and Xe+La collisions at $40 - 150A$ GeV/c based on data recorded by the NA61/SHINE collaboration. The analysis of Λ and $\bar{\Lambda}$ production at this energy range was not studied before, and the proposed project is the first one with high-quality data sets where such measurement can be performed.

The identification of Λ ($\bar{\Lambda}$) will be performed via the decay to charged final state particles: $\Lambda \rightarrow p + \pi^-$ ($\bar{\Lambda} \rightarrow \bar{p} + \pi^+$) as shown in Figure 4. It is the most populated decay channel as its branching ratio is $(63.9 \pm 0.5)\%$ ⁶.

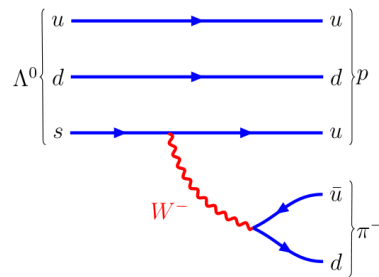


Figure 4: *A Feynman diagram showing the decay channel $\Lambda^0 \rightarrow p\pi^-$.*

3.2 Analysis workflow

The general analysis workflow is shown in Figure 5. The raw measured data is processed by the reconstruction chain, where trajectories and momenta of tracks are reconstructed as well as the position of the main vertex. More details on the track and vertex reconstruction can be found in ⁷⁾. Then all V^0 candidates are searched for in the dedicated module. In the first stage of the search, the tracks are backwards extrapolated in the magnetic field with a fixed approximation step of 2 cm, and the distance-of-closest-approach (DCA) is calculated for each pair of oppositely charged tracks in the event. If the DCA is smaller than the defined value, then the z-axis position (along the beam) of the smallest DCA is saved together with the tracks as daughter tracks of the V^0 candidate. In the second stage of the search, the momenta of both daughter tracks are recalculated together with the position of the V^0 vertex by performing a nine-parameter fit, where the daughter tracks are treated as a pair coming from the same vertex. The quality and centrality event selection is subsequently performed (typically, 10% most central events are chosen). Further analysis is limited to a specific kinematic region in the rapidity-transverse momentum ($y - p_T$) phase space divided into bins, which is driven by the statistics available for a given dataset. Reconstructed V^0 candidates can be real V^0 particles or combinatorial background, and the real V^0 particles will generate a peak in the invariant mass spectra. The decay products of V^0 candidates are identified through a specific energy loss (dE/dx) measured in the TPC, which should be within $\pm 3\sigma$ range within the nominal Bethe-Bloch value for a given particle (e.g. proton or pion). The analysis procedure is optimised in such a way as to reduce as much background as possible taking into account signal reduction. The performance of the cuts is verified through the plotting of signal significance $\frac{S}{\sqrt{S+B}}$ simultaneously with normalised signal reduction for different cut values. Additionally, the Armenteros-Podolanski plot ⁸⁾ is used to check the quality of the applied cut combination. The resulting invariant mass spectra in each $y - p_T$ bin are then fitted with a sum of a Lorentz distribution describing the signal and a polynomial function describing the background. The obtained signal yields are normalised to the number of analysed events and area of a single $y - p_T$ bin. The generated simulation data undergo the same reconstruction and analysis procedure in order to correct for the losses caused by limited detector acceptance, reconstruction efficiency etc. The quality of the analysis procedure is additionally checked through the Monte-Carlo closure test and mean lifetime measurement. More details on the procedure performed in a similar analysis in proton-carbon collisions can be found in ⁹⁾.

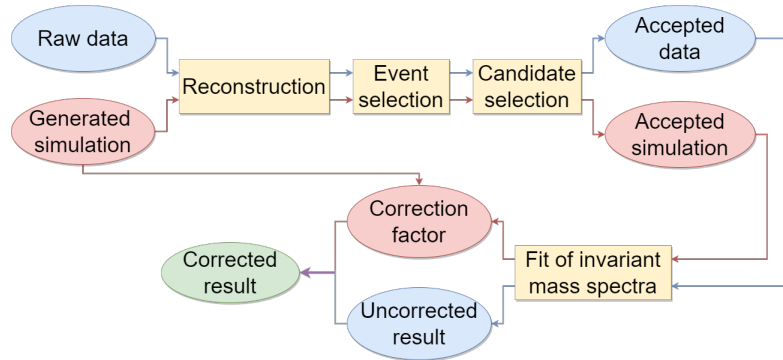


Figure 5: *Workflow of the analysis.*

3.3 Expected outcome

The amount of collected data for the mentioned reactions should allow for the measurement of two-dimensional spectra in a wide $y-p_T$ range. One-dimensional p_T spectra will be fitted with an exponential function in order to obtain the inverse slope parameter T and extrapolate spectra to the unmeasured high p_T region. Obtained one-dimensional rapidity spectra will be fitted with a sum of Gaussian distributions in order to obtain total mean multiplicity $\langle\Lambda\rangle$ and $\langle\bar{\Lambda}\rangle$.

The results of the analysis will be compared to different particle production models such as EPOS 1.99 [10], UrQMD 3.4 [11, 12], AMPT 1.26 [13, 14, 15], SMASH 1.6 [16, 17] and PHSD [18, 19], all of which differ by the physics mechanism used to describe heavy ion interactions. This comparison will help to understand the mechanism of strange baryon production in nucleus-nucleus collisions. These new results will bring us closer to understanding the properties of the onset of deconfinement.

4 Conclusions

Strangeness production is a well-known valuable probe for understanding particle production in high-energy physics because of the absence of the strange valence quarks in the initial state of the collision. The proposed project aims to extend the study of strangeness production, namely the production of Λ and $\bar{\Lambda}$ hyperons in Ar+Sc and Xe+La collisions in the CERN SPS energy range. These measurements will complement already existing and future results on meson production in the mentioned collision systems. Overall, the results will shed light on possible quark-gluon plasma formation in medium size systems and will help to understand how it depends on system size.

5 Acknowledgements

This work was supported by the funds granted under the Research Excellence Initiative of the University of Silesia in Katowice and by the Polish Minister of Education and Science (contract No. 2021/WK/10).

References

1. M. Gazdzicki et al., *Acta Phys. Pol. B* **42**, 307 (2011).
2. J. Rafelski and B. Muller, *Phys. Rev. Lett.* **48**, 1066 (1982). [Erratum: *Phys. Rev. Lett.* **56**, 2334 (1986)].
3. M. Gazdzicki, M.I. Gorenstein, *Acta Phys. Pol. B* **30**, 2705 (1999).
4. A. Aduszkiewicz [NA61/SHINE Collab.], *Tech. Rep. CERN-SPSC-2017-038. SPSC-SR-221* (2017).
5. N. Abgrall et al. [NA61/SHINE Collab.], *JINST* **9**, P06005 (2014).
6. P. A. Zyla et al [Particle Data Group], *Prog. Theor. Exp. Phys.* **2020**, 083C01 (2020).
7. N. Abgrall et al. [NA61/SHINE Collab.], *Eur. Phys. J. C* **74**, 2794 (2014).
8. J. Podolanski and R. Armenteros. *The London, Edinburgh, and Dublin Philosophical Magazine and Journal of Science*, **45**, 13–30 (1954).
9. N. Abgrall et al. [NA61/SHINE Collab.], *Eur. Phys. J. C* **76**, 84 (2016).

10. K. Werner, Nucl. Phys. Proc. Suppl. **175-176**, 81–87 (2008).
11. S. Bass et al., Prog. Part. Nucl. Phys. **41**, 255–369 (1998).
12. M. Bleicher et al., J. Phys. **G25**, 1859–1896 (1999).
13. Z.-W. Lin et al., Phys. Rev. C **72**, 064901 (2005).
14. Z.-W. Lin, Phys. Rev. C **90**, 014904 (2014).
15. B. Zhang et al., Phys. Rev. C **61**, 067901 (2000).
16. J. Mohs et al., J. Phys. **G47**, 065101 (2020).
17. J. Weil et al., Phys. Rev. C **94**, 054905 (2016).
18. W. Cassing et al., Nucl. Phys. A **831**, 215–242 (2009).
19. W. Cassing et al., Phys. Rev. C **78**, 034919 (2008).

New Small Wheel Micromegas trigger simulation analysis

F. Montekali^{a,b} on behalf of the ATLAS Muon Collaboration

^a*Dipartimento di Matematica e Fisica, Università degli Studi Roma Tre,*

^b*INFN Sezione di Roma Tre,*

Via della Vasca Navale 84, Roma, Italia

Abstract

During the Long Shutdown 2, the most important upgrade of the ATLAS experiment was the first muon station in the high-rapidity region with the New Small Wheels (NSW) installation. These new detector structures utilize two innovative detector technologies: the small strip Thin Gap Chambers (sTGC) and the Micromegas (MM) for trigger and precision tracking at the high particle rates expected for the Run-3 and High-Luminosity LHC phases. The simulation of both sTGC and MM trigger was implemented and performance evaluated in different configurations, serving as a crucial input for the optimization and hardware implementation of the trigger logic.

This work presents the results from the Micromegas trigger simulation analysis. It includes the study of angular variable reconstruction, the definition and description of Region-of-Interest (RoI) and segment output parameters for the coincidences with other stations of the spectrometer, and the validation of the correct trigger operation finding possible errors or bugs.

1 The ATLAS detector

The ATLAS detector ¹⁾ is a general purpose particle detector at the Large Hadron Collider (LHC). It is the largest particle detector ever built, with a length of 44 m, a diameter of 25 m and a weight of 7000 tons. The detector is structured in three concentric cylindrical sub-detector systems at the centre of which lies the interaction point (IP), which is the intersection between two beam pipes, that contain beams of protons travelling at near light-speed in opposite directions. The protons collide with a centre of mass energy of approximately 13.6 TeV.

Close to the beam line, there is the Inner Detector (ID), that allows to reconstruct the tracks and measure the momentum of the charged particles produced in collisions. It provides also the identification of the interaction vertices. The calorimeter system is placed around the ID and it is composed by an

electromagnetic calorimeter (ECAL), dedicated to the identification of electromagnetic showers, and a hadronic calorimeter (HCAL), needed to identify and measure the energy of hadronic jets. Lastly, the Muon Spectrometer (MS), located in the outermost region of the detector, is dedicated to the identification and high precision measurement of muons and their momentum.

These sub-detectors are divided longitudinally in three regions, the central part, called barrel and the two edges of the cylinder, called end-caps. The geometric acceptance is close to 4π sr in solid angle.

Two separate magnetic systems produce the magnetic fields that allow the measurement of the momentum of the charged particles by curving their trajectory: a 2 T solenoid magnet surrounds the Inner Detector, while a 8-coil toroidal magnetic system (0.1-3 T) plays the same role for the Muon Spectrometer.

In this work, the coordinate system follows the ATLAS convention: it is a xyz right-handed reference system centered in the nominal interaction point of the beams, where the z -axis is defined along the beam direction, the x -axis points towards the center of the LHC ring and the y -axis is pointing upwards. The detector part in the positive z -direction is called side A, the part in the negative z -direction side C.

This reference system is usually defined by cylindrical coordinates: the radial coordinate R , the distance from the beam line in the x - y plane, the azimuth angle ϕ , measured around the beam, and the polar angle θ , measured with respect to the beam axis. The pseudo-rapidity is defined as $\eta = -\log(\tan(\theta/2))$.

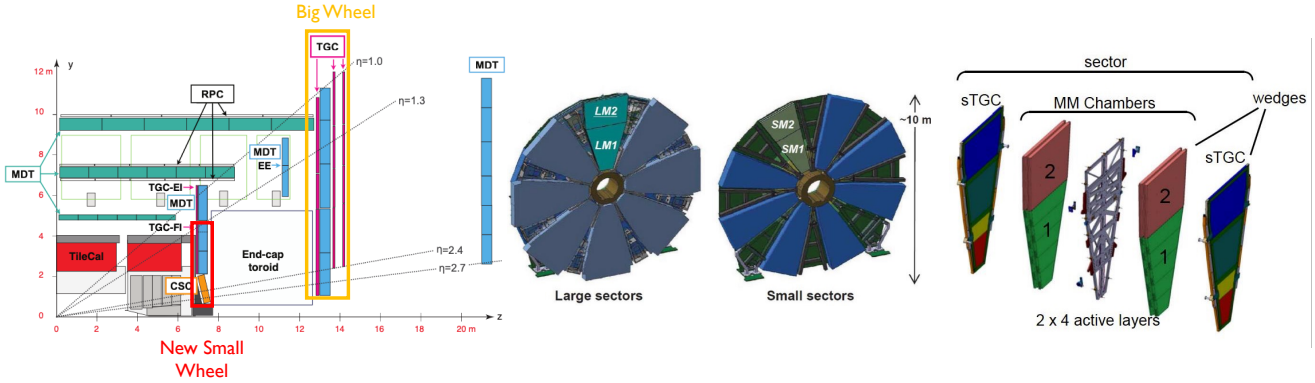


Figure 1: *Left to Right: a z - y view of $1/4$ of the detector: the arrangement of the two Muon Spectrometer detector groups and the regions of the Big Wheel and where the New Small Wheel has been installed (CSCs are completely removed) are visible³⁾. Wheel-like structure of the NSW highlighting the 4 MM modules of the Large and Small sectors (LM 1-2, SM 1-2)⁴⁾. The position of MM and sTGC chambers⁵⁾.*

2 New Small Wheels

In Run-1 and Run-2, the Muon Spectrometer was composed by two specific groups of detectors, Fig. 1: the first one consisting of the Resistive Plate Chambers (RPC) and the Thin Gap Chambers (TGC), that cover the barrel and endcap regions respectively which have a high timing resolution, allowing to identify the collision of the detected muon. The second group detectors are Monitored Drift Tubes (MDT) and the Cathode Strip Chambers (CSC), that have high position resolution and they are used for precise tracking at a later stage of the muon trigger and in the offline analysis. In the end-caps, $1.0 < |\eta| < 2.7$, the detectors are placed in three wheels orthogonal to the z -axis, the Small Wheel (SW) before the end-cap toroids, the Big Wheel (BW) after the toroids, and the Outer Wheel at ~ 6 m after the Big Wheel.

In order to exploit the high luminosity (up to $5 - 7 \times 10^{34} \text{cm}^{-2} \text{s}^{-1}$) performance expected in Run-3 and

High Luminosity LHC (HL-LHC) the first station of the muon end-cap system, the Small Wheel, have been replaced during the Long Shutdown 2 by the New Small Wheels (NSW) ²). The huge increase of particle rates would have resulted in a loss in efficiency of the Small Wheel, affecting the trigger and tracking performances due to the presence of many fake non-prompt muons and more background.

The ATLAS New Small Wheels utilize two innovative detector technologies: small-strip Thin Gap Chambers (sTGC) and Micromegas (MM) both for trigger and tracking, providing excellent performances thanks to the high spatial resolution, that in particular for MM is $< 100 \mu\text{m}$ for small angles and $72 \mu\text{m}$ for perpendicular tracks. This allows to confirm, at high expected rates, whether a particle originated from the interaction point and to reduce unwanted background events and thus a better efficiency.

Each wheel, side A and side C, is composed of 16 sectors, 8 small and 8 large ones. Each sector is composed by two sTGC wedges enclosing two MM wedges, as visible from Fig. 1. Each sector is composed of two sTGC wedges and two MM wedges. The sTGC wedges are made of three quadruplets modules, each composed of four sTGC layers. The MM wedges are, instead, made of two quadruplet modules, made by 2 precision (X) and 2 stereo (U/V) strip layers, with the readout strips tilted by respectively $+1.5^\circ$ and -1.5° providing second coordinate information.

Both the sTGC and MM chamber technologies contribute to the Level-1 muon end-cap trigger.

3 Micromegas Level-1 trigger algorithm

The Micromegas Level-1 (L1) trigger algorithm is known as *DiamondRoads algorithm*, that consists of the segmentation of the RZ space in roads (Fig. 2), that point back to the pp interaction point, of 8 strips ($\sim 3.5 \text{ mm}$) depending on the $\text{slope} = \frac{\text{strip}R}{\text{strip}Z}$. The road size has been optimised to reject background coincidences.

The trigger coincidence logic requires the presence of hits in at least 3X and 3U/V layer roads. The intersection in one point of X, U, V roads geometrically forms a diamond, middle picture of Fig. 2.

Roads have overlap regions, as shown in Fig. 2, for muons passing at the boundary with the neighboring road, and the size of the overlap is determined by the position resolution.

The coincidence logic is verified using the roads triggered in a sliding timing window of 4 bunches crossing (BC) within a 8 BCs range.

Due to both the road overlap and the sliding window, there is the possibility of having multiple triggers for the same track and thus the best candidate has to be chosen, at the moment taking the one with more planes.

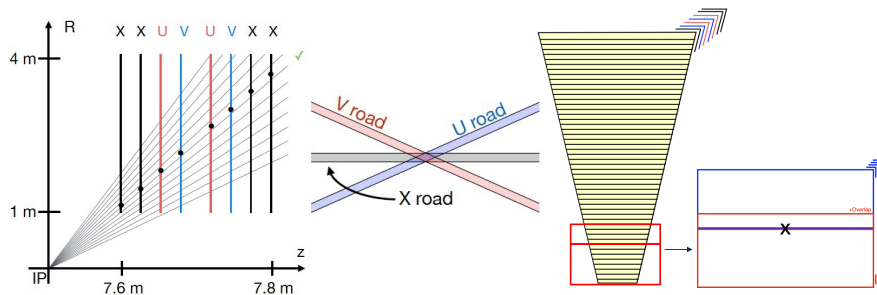


Figure 2: Left to right: the segmentation of the RZ space in roads. The diamond formed by the intersection of the X, U, V roads. The schematic diagram of multiple X-U-V strip layers and of a muon hit on the boundary of two roads, triggered thanks to the road overlap.

4 NSW Trigger Processor

Micromegas and sTGC triggers are stand-alone triggers, each using its 8 detector layers in each NSW sector. Trigger algorithm finds trigger candidates and provides a segment identifying a Region-of-Interest (RoI). On every bunch crossing, the NSW trigger processors (one for each sector) send to the Sector Logic up to 8 unique track segment that point to the Big Wheel: Micromegas can provide up to 8 segments per sector but a merging is done with sTGC segments to select the final 8 segments (4 MM and 4 sTGC) per sector per BC.

If the Sector Logic receives a NSW track segment that matches a Big Wheel track segment, it sends the transverse momentum p_T and RoI information of the segment with a “NSW” flag to the Muon-to-Central Trigger Processor Interface (MUCTPI), that combines the number of muon candidates, provided also by the barrel MS trigger, and makes the final decision of the muon trigger.

The local segment output parameters that define the RoI are R_{id} , ϕ_{id} and $\Delta\theta_{id}$. The R -indices are a range of radii along the radial axis of symmetry of the sector and can be extrapolated in the plane at $|z| = 7177$ mm and at $|z| = 7641$ mm (coordinates evaluated at the double wedge center), for small and large sectors respectively. The range of R in this plane is $900 < R < 5000$ mm and the R -index, encoded by an integer between 0-255, increasing in the outward radial direction, gives R with 16 mm resolution. The ϕ -index is defined locally with $\phi = 0$ along the radial axis of symmetry of each sector (clockwise). The ϕ -range of a large MM sector spans $\pm 16^\circ$ and for a small MM sector $\pm 11^\circ$, corresponding to a integer ϕ_{id} between 0-31 and 5-27 respectively, with 9 mrad resolution.

$\Delta\theta$ is the angular deviation of the segment from the infinite momentum track, i.e. the straight track passing through the interaction point to the radial position in the NSW. This parameter is important because it is used to discard background tracks and secondary tracks not coming from the IP: all segments with $|\Delta\theta| \geq 15$ mrad are discarded by electronics. $\Delta\theta_{id}$ gives $\Delta\theta$ with a 1 mrad resolution as an integer number between 0-31 (± 15 mrad).

5 Results and conclusions

The results of this work are obtained using di-muon samples with no background, flat in $p_T \in [10, 100]$ GeV and in η , assuming nominal detector conditions.

MM trigger algorithm reconstructed segments are used to evaluate the trigger algorithm performances. The angular variable θ residuals of the triggered segments with the corresponding truth muon track is shown in Fig. 3. The angular resolution is evaluated by a double gaussian fit obtaining an excellent resolution $\sigma_{core} = 1.1$ mrad, in line with what expected from the NSW design for the angular reconstruction at Level-1 trigger (~ 1 mrad)².

The MM trigger efficiency is evaluated as a function of angular variable ϕ and η and shown in the 2D histogram right plot of Fig. 3. It is mostly close to one in the two NSWs projections and it drops in the gap between MM modules at $|\eta| < 2$ and between sectors at $|\eta| > 2$. By investigating the efficiency on the x - y plane for the two separated wheels, left plots of Fig. 4, it is possible to see that the inefficiency at large $|\eta|$, the blue radial segments visible at wheels' centre, is due to detector active area passivations. Different passivations are applied to the two wheels and are implemented in the detector geometry. The results are in qualitative agreement (to be further validated) with geometry simulation, as it can be seen comparing the plots of Fig. 4. The three RoI identifiers, R_{id} , ϕ_{id} and $\Delta\theta_{id}$, are evaluated from the segment's direction and angle. Combining the R_{id} and ϕ_{id} information the typical shapes of large and small sectors are obtained and shown in Fig. 5.

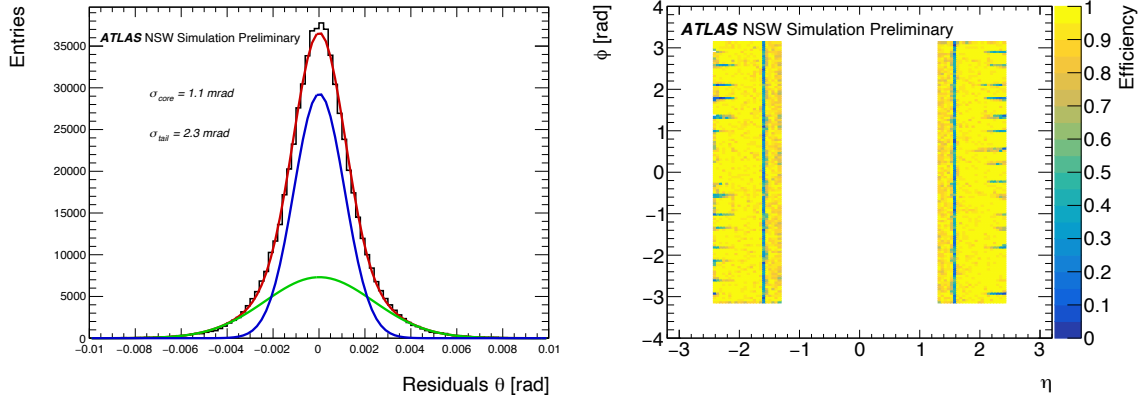


Figure 3: *Left: Residuals distribution of the θ coordinate. The resolutions are extracted performing a double Gaussian fit. Right: the MM trigger efficiency as function of angular variable ϕ and η ⁶⁾.*

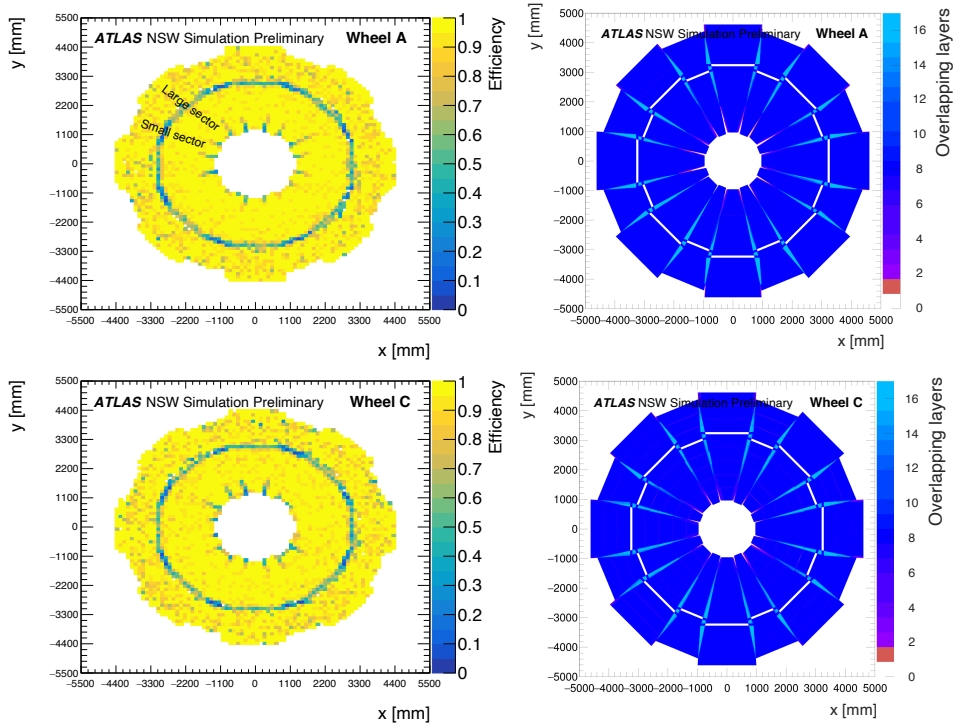


Figure 4: *Left: MM trigger efficiency as a function of x and y spatial coordinates is shown for both the Wheel A and C. Right: visualization of actual geometrical passivation for both the wheels ⁶⁾.*

The $\Delta\theta_{id}$ distribution is also displayed in Fig. 5. The plot shows how the NSW stand-alone triggered muons are reconstructed as infinite momentum track since the distribution has a peak at the center, as expected for the simulated muons coming from the IP.

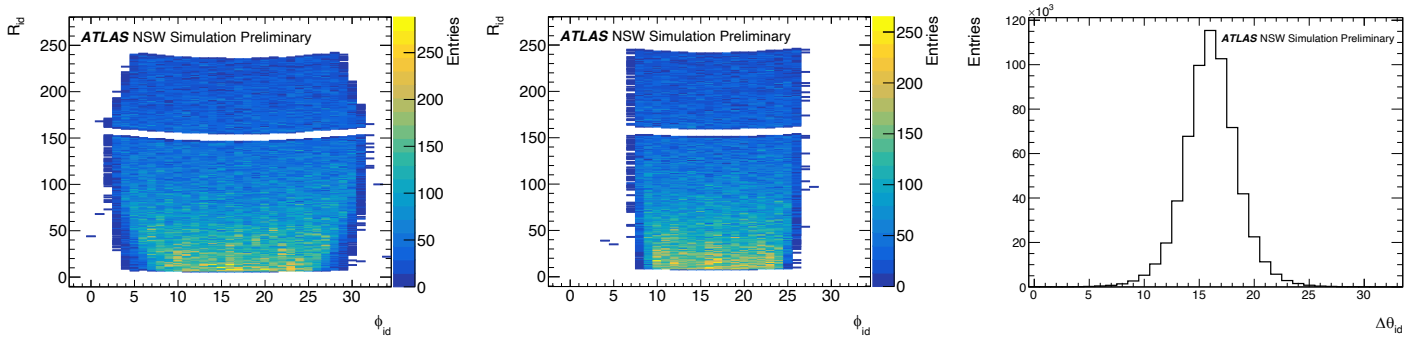


Figure 5: Distributions of the local segment output parameters: R_{id} , ϕ_{id} and $\Delta\theta_{id}$. The typical shapes of large and small sectors are visible thanks to the combination of R_{id} and ϕ_{id} information ⁶⁾.

Since in the NSW the MM trigger processor allows to send out at most 8 MM segments per BCID and sector, this limit should be taken into account. For each event the number of segments is evaluated and the duplicate segments with same RoI indices, BCID and sector are identified. Currently the BCID segment is calculated as the mean BCID of the hits entering the diamond for each timing window.

Duplicates arise from the combination of hits entering in the sliding timing window, which can result in multiple segments with same RoI identifiers and same assigned BCID. The number of triggered segments and duplicates for each BC and sector is show in Fig. 6. Such duplicates can be removed from the MM trigger processor if they have exactly the same identifiers and BCID. The total number of MM segments can be reduced in such a way below the limit of 8 segments per BC and sector, having in $\gtrsim 60\%$ of the cases a one-to-one correspondance simulated/reconstructed muon.

In conclusion, an excellent θ resolution and angular efficiency are obtained. An in-depth study of the

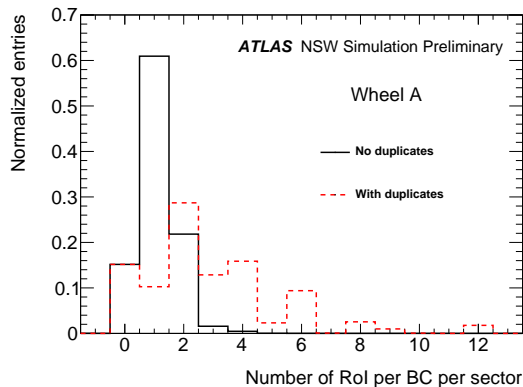


Figure 6: Number of RoI per BC per sector for the Wheel A is shown. A normalization by the total number of histogram entries is applied. The red dashed line indicates the case where there are duplicates of the reconstructed muon while the black solid line the case where the hardware can remove them ⁶⁾.

output segment parameters to identify duplicates and candidates with different RoI, useful for hardware duplicate removal implementation and rate reduction for background, is proposed. Future analysis will be based on the evaluation of trigger rates by using Monte Carlo samples including pile-up and cavern background simulation, $Z \rightarrow \mu^+ \mu^-$ sample and implementing realistic timing resolution.

References

1. G. Aad *et al.* [ATLAS], JINST **3** (2008), S08003 DOI:10.1088/1748-0221/3/08/S08003.
2. T. Kawamoto, S. Vlachos, L. Pontecorvo, J. Dubbert, G. Mikenberg, P. Iengo, C. Dallapiccola, C. Amelung, L. Levinson and R. Richter, *et al.* CERN-LHCC-2013-006.
3. G. Aad *et al.* [ATLAS], JINST **15** (2020) no.09, P09015 DOI:10.1088/1748-0221/15/09/p09015 arXiv:2004.13447 [physics.ins-det].
4. T. Alexopoulos, M. Alviggi, M. Antonelli, F. Anulli, C. Arcangeletti, P. Bagnaia, A. Baroncelli, M. Beretta, C. Bini and J. Bortfeldt, *et al.* Nucl. Instrum. Meth. A **955** (2020), 162086 DOI:10.1016/j.nima.2019.04.040 arXiv:1808.09752 [physics.ins-det].
5. I. Manthos, I. Maniatis, I. Maznas, M. Tsopoulou, P. Paschalias, T. Koutsosimos, S. Kompogiannis, C. Petridou, S. E. Tzamarias and K. Kordas, *et al.* AIP Conf. Proc. **2075** (2019) no.1, 080010 DOI:10.1063/1.5091211 arXiv:1901.03160 [physics.ins-det].
6. F. Montereali, S. Angelidakis, *Micromegas trigger simulation plots*.

CROSS-SECTION MEASUREMENT OF $VH \rightarrow b\bar{b}$ PROCESS AT CMS EXPERIMENT

Saswat Mishra
Rudjer Boskovic Institute

Abstract

An overview of the measured $VH \rightarrow b\bar{b}$ cross-section is presented. The measurement is performed using dataset collected during 2016-2018 by the CMS experiment from LHC p-p collisions at $\sqrt{s} = 13$ TeV corresponding to a total integrated luminosity of 138 fb^{-1} . The analysis searches for one Standard Model Higgs boson at $m_{H} = 125$ GeV decaying into a pair of b-quarks and a W or Z boson that decays into lepton final states with 0, 1, or 2 electrons or muons. The Higgs boson is reconstructed from two resolved b-tagged jets or from a single large-radius jet containing the decay products of two b-jets at large momenta. The cross-section measurement is performed differentially in bins of transverse momentum of the W or Z boson.

1 Introduction

In Standard Model, the Brout-Englert-Higgs mechanism allows electroweak gauge bosons to acquire mass via electroweak symmetry breaking which has been observed with the mass measurements of the W^{\pm} and the Z bosons. This led to the prediction of a new massive scalar boson, i.e. the Higgs boson which was subsequently discovered in 2012 jointly by the CMS and the ATLAS collaborations. Ten years after its discovery the mass of the Higgs boson is now most precisely measured by CMS experiment to be $m_H = 125.35 \pm 0.15$ GeV with a precision level of 0.12% [1]. ATLAS also measured $m_H = 124.94 \pm 0.18$ GeV but with a slightly lower precision of 0.14% [2]. Besides that, all observed couplings and properties of the Standard Model Higgs boson are consistent with theoretical predictions.

The Standard Model Higgs boson has a branching fraction of 58% when decaying into a pair of b-quarks making it the most dominant Higgs boson decay and this decay was observed by the CMS experiment in 2018 with an observed (expected) significance of 5.6σ (5.5σ)[3] and by ATLAS experiment with an observed (expected) significance of 5.4σ (5.5σ)[4]. In Hbb process, majority of Higgs bosons

produced at CMS are via gluon-fusion mechanism (78%), precise measurements in this production channel has not been possible due to overwhelming multi-jet background events. ZH & WH production mode, on the other hand, is more efficient in terms of precise measurements of the Higgs boson. This is because of the ability to exploit leptonic signatures which are the decay products of the Z or W boson in the event.

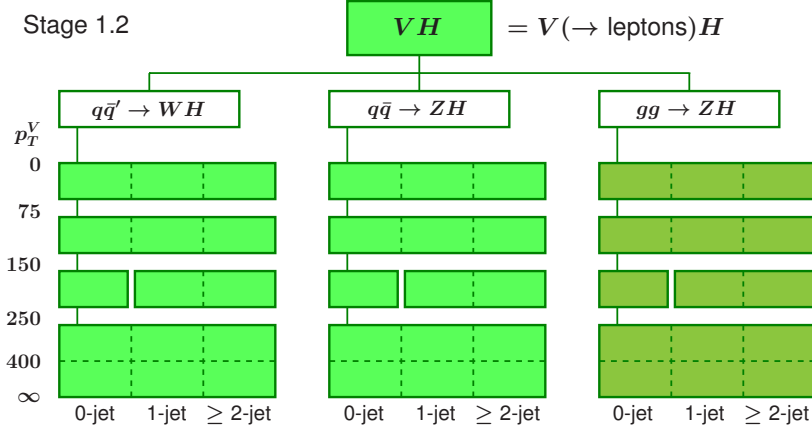


Figure 1: Stage 1.2 of STXS categorization for the $VH, H \rightarrow b\bar{b}$ process.

Simplified Template Cross-section (STXS) framework is a widely adopted framework used for measuring differential cross-sections in CMS, ATLAS and theory communities of LHC [5]. For the VH production mode where the vector boson decays leptonically, the STXS analysis is performed in bins of $p_T(V)$ but also in number of additional jets (N_{aj}). The signal is partitioned using MC-truth and the analysis is performed in the equivalent reconstructed categories. In our analysis, we use stage 1.2 of the prescribed STXS categorization in order to finely bin certain regions to gain better insight while merging/ignoring certain other regions which lack sensitivity. Fig. 1 shows an overview of STXS categories for $VH, H \rightarrow b\bar{b}$ process.

2 Signal and Background Processes

The signal processes contain Higgs bosons, with $m_H = 125$ GeV, produced in association with W or Z bosons. In this analysis, only the leptonic decays of the W or Z boson are considered. Although quark-induced ZH and WH processes contribute mostly to the overall VH signal, a minor contribution from gluon-induced ZH process is also accounted for in the total signal. For backgrounds, various processes having similar signature as signal are considered. $t\bar{t}$, V +jets and diboson processes, that consisting in ZZ , WZ and WW decay modes, are some of the major background processes of this analysis. Different channels in the analysis get different background enrichment depending on the overall final state of the vector boson in that channel. Hence, separate channel-based background modeling is performed to accurately determine the background in each channel.

3 Event Reconstruction

The analysis searches for two b-quarks in form of b-jets as decay products of the Higgs boson and leptons coming from the decay of the Z or W boson. Based on the leptons from the vector boson, The analysis

uses three categories based on the number of leptons of the vector boson decay, i.e. 0-lepton where the Z boson decays into pair of neutrinos which is measured in the detector in form of large missing transverse energy (MET), 1-lepton where the W boson decays into a lepton and a neutrino and 2-leptons channel where the Z boson decays into pair of same flavor leptons. Channel based selections and treatments are implemented because each channel has different decay products from the vector boson. This is performed to ensure signal purity and proper background estimation in their respective channels.

3.1 Boosted Analysis

When the Higgs boson is produced with a large Lorentz boost, the b-jets produced from its decay are collimated resulting in a single merged jet with a large cone radius:

$$\Delta R_{b,\bar{b}} \approx \frac{2}{\gamma} = \frac{2m_H}{E} > \frac{2m_H}{p_T}. \quad (1)$$

Using equation 1, it is seen that the angular separation (ΔR) between the b-jets reduces to less than unity for p_T values larger than 250 GeV. To account for boosted phase space in b-jets, a dedicated boosted analysis is performed which searches for a single fat jet of larger cone radius of 0.8 compared to nominal resolved analysis, which looks for two separate b-jets of cone radius of 0.4. A dedicated selection is applied to select boosted Higgs boson events. Both resolved and boosted analyses are statistically combined in the final fit to maximize sensitivity in high $p_T(V)$ (>250 GeV) STXS bins.

3.2 Identification of b-jets

As mentioned in previous section, the Higgs boson candidates in this analysis are pairs of b-jets. Therefore accurate clustering and identification of b-jets is an important step and contributes heavily towards precision of the measurement. First of all, every jet in an event is reconstructed using dedicated jet clustering algorithm. This analysis uses Anti-kT algorithm [6] for jet clustering. In resolved analysis, jets are clustered with a cone radius of 0.4 while in boosted analysis the clustering is performed with a wider jet cone of 0.8. The clustered jets in resolved and boosted analysis are called AK4 and AK8 jets respectively for convenience. Reconstructed jets are then passed through a b-tagging algorithm which distinguishes jets from b hadrons to light flavored jets. The b-jets identified in resolved analysis are tagged using DeepCSV [7] algorithm while merged b-jets in boosted analysis are tagged using DeepAK8 algorithm [8]. Both DeepCSV and DeepAK8 are Deep Neural Network(DNN) based algorithms which exploits difference in kinematic information of b-jets and light flavor jets. Deep Charged Secondary Vertex or DeepCSV relies on secondary vertex and impact parameter information of b-jets while DeepAK8 is designed to identify large cone jets originating from b-hadrons using jet substructure information.

3.3 Lepton Identification

Presence of isolated leptons or large MET which is signature in the 0-lepton channel along with a pair of b-tagged jets are the primary signature of this analysis. Electrons are preselected by requiring $p_T > 7$ GeV, $|\eta| < 2.4$, $d_{xy} < 0.05$ cm, $d_z < 0.2$ cm and a relative isolation smaller than 0.4. Following this, a multi-variate (MVA) based identification is applied and two different working points are selected based on the expected electron identification efficiency of either 80% (loose working point) or 90% (tight working point). The tight working point with a p_T threshold of 30 GeV is used to select events in 1-lepton channel. For the 2-leptons channel, the thresholds are 25 GeV and 17 GeV for the two electrons. Muons are preselected by requiring the following: $p_T > 5$ GeV, $|\eta| < 2.4$, $d_{xy} < 0.5$ cm, $d_z < 1.0$ cm, and a

relative isolation below 0.4. The muon p_T threshold in 1-lepton channel is 25 GeV and for 2-leptons channel, these thresholds are 25 GeV and 15 GeV for the two muons.

4 Analysis Strategy

4.1 Event Selection

Events are selected by applying kinematic based selections to categorize them in various regions. Each STXS bin in each channel is broadly divided into one signal region and 3 associated control regions. The signal regions are enriched in signal process and serve as the primary region for signal extraction. The 3 control regions namely, $t\bar{t}$, V+ heavy flavor and V+ light flavor are constructed and their selections are kinematically orthogonal to the signal region. Control regions are used for constraining the respective backgrounds using data driven predictions. A cut on $N_{aj} \geq 2$ differentiates $t\bar{t}$ CR from signal region, while events that fail to pass the cut on DeepCSV (DeepAK8 in boosted) score fall in the V+ light flavor region. The V+ heavy flavor region is classified as the side-band region of the m_H window which is [90,150] GeV.

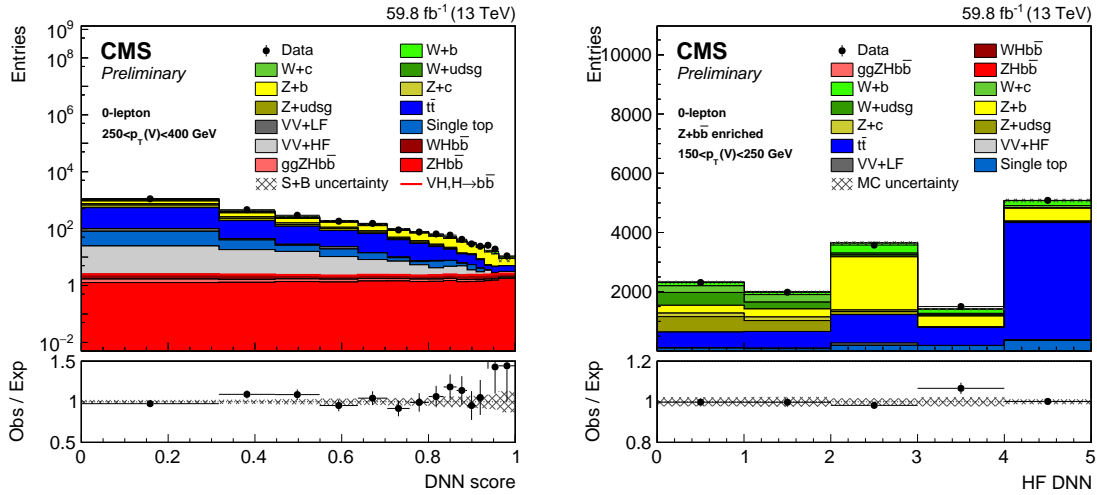


Figure 2: *Deep Neural Network template in signal region (left) and V+ Heavy flavor region of 0-lepton channel show excellent data Mont-Carlo agreement*

4.2 Multi-variate Methods

In order to improve the separation between signal and background, deep neural network (DNN) based classification is constructed in signal region for each lepton channel. DNN is a machine learning technique widely used in high energy physics community for classification purposes. The algorithm consists of layers of intertwined nodes, which can be tuned based on desired classification. DNN used in this analysis, is trained on Monte-Carlo samples and based on the evaluation, each event gets a DNN score that denotes whether the DNN is signal-like (DNN score 1) or background-like (DNN score 0). (Fig.2 left). In boosted analysis signal regions, training is performed using Boosted Decision Trees (BDT) instead of DNN. In the V+HF (heavy flavor) control region for the 0 and 1-lepton channels, a multi-class classifier is trained

to separate the different V +jets components (vector boson production associated to light-flavor, c , and b -jets), single top quark, and $t\bar{t}$ backgrounds (Fig.2 right).

The input features used in the DNN training encompass the kinematical properties of the final state: masses, momenta, and angles of the dijet system, of the jets, of the vector boson candidate, and of the leptons. The additional reconstructed jet multiplicity is also used. These variables are chosen via an iterative optimization procedure, starting from a large number of potentially discriminating variables. The modeling of these variables in data, before a fit to data is performed, is also inspected.

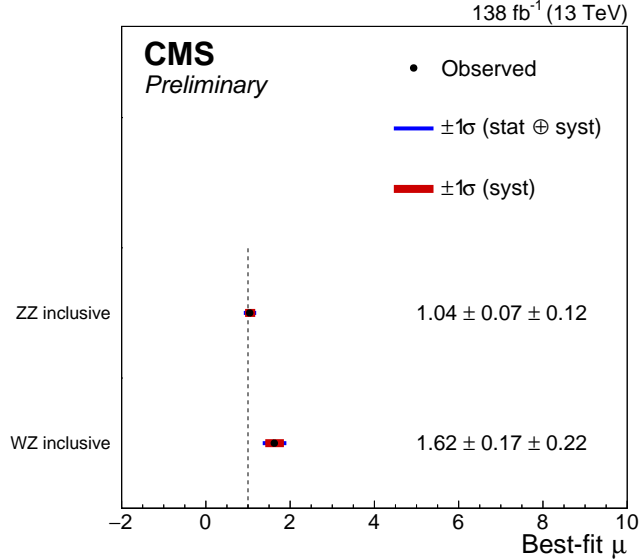


Figure 3: Result of the VZ , $Z \rightarrow b\bar{b}$ channel analysis using the full Run 2 dataset for both the WZ and ZZ production modes

5 Result

Signal is extracted in each STXS bin of the signal region by performing a binned maximum likelihood fit by performing simultaneous fit to data in all signal and control regions based on the template detailed in Table 1. The analysis regions are partitioned in categories targeting specific STXS bins, in order to maximize the sensitivity to the different STXS bin signals. The output of the maximum-likelihood fit is signal strength (μ) which is the ratio of observed signal yield to expected Standard Model yield for a certain region. Therefore, $\mu = 1$ represents the Standard Model prediction.

5.1 VZ , $Z \rightarrow b\bar{b}$ cross-check analysis

For validating the analysis, the VH , $H \rightarrow b\bar{b}$ process is replaced by the VZ , $Z \rightarrow b\bar{b}$ by altering the mass window to include the Z boson mass. Dedicated MVAs are trained for the VZ , $Z \rightarrow b\bar{b}$ keeping the fit strategy the same as the main analysis. The extracted signal strengths for the ZZ and WZ processes are reported in Fig. 3 for all channels when using the 2016–2018 dataset. The inclusive observed VZ , $Z \rightarrow b\bar{b}$ signal strength is $\mu = 1.16 \pm 0.13$ corresponding to an observed and expected significances well above 5 standard deviations.

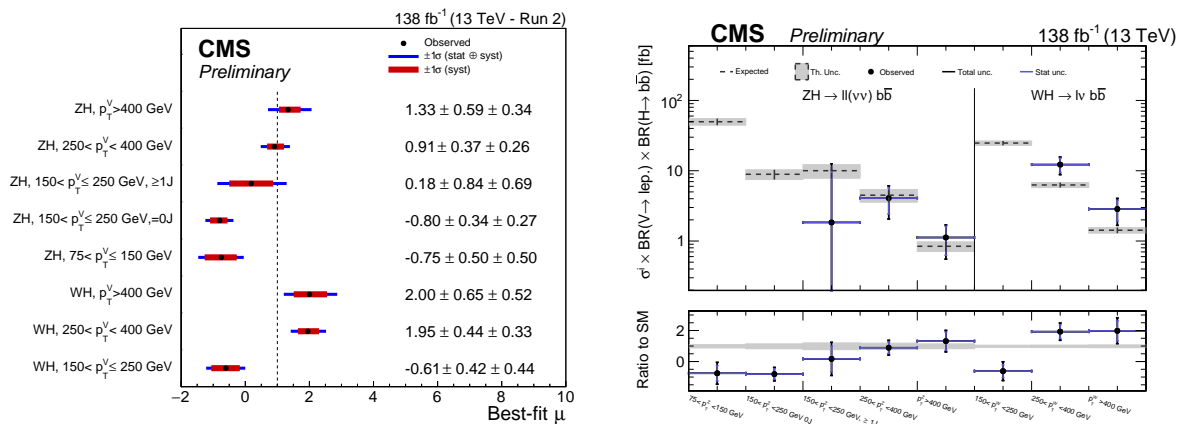


Figure 4: Measured STXS signal strengths from the fit (left). Measured values of $\sigma \times \mathcal{B}$ in the same STXS bins as for the signal strengths, combining all years (right).

Table 1: Discriminating variables fitted in each signal and control region.

	SR	$t\bar{t}$ CR	V+LF CR	V+HF CR
0-lepton, resolved	DNN	$p_T(V)$	$p_T(V)$	HFDNN
0-lepton, boosted	BDT	DeepAK8 score	DeepAK8 score	DeepAK8 score
1-lepton, resolved	DNN	$p_T(V)$	$p_T(V)$	HFDNN
1-lepton, boosted	BDT	DeepAK8 score	DeepAK8 score	DeepAK8 score
2-leptons, resolved	DNN	$p_T(V)$	$p_T(V)$	DeepCSV score
2-leptons, boosted	BDT	DeepAK8 score	DeepAK8 score	DeepAK8 score

5.2 $VH, H \rightarrow b\bar{b}$ STXS Measurement

The $VH, H \rightarrow b\bar{b}$ signal is extracted in each STXS bin from the fit combining datasets from 2016-2018. The inclusive signal strength with respect to Standard Model ($\mu = 1$) is measured to be $\mu = 0.58^{+0.19}_{-0.18}$ corresponding to an observed (expected) significance of 3.3 standard deviations (5.2 standard deviations). Fig. 4 (left) shows the measured signal strengths in each STXS bins. These results are further interpreted as VH production cross sections multiplied by the branching fraction ($\sigma \times \mathcal{B}$) of $V \rightarrow \text{leptons}$ and $H \rightarrow b\bar{b}$ in Fig. 4 (right). To represent the results as production cross sections, theoretical uncertainties that modify the overall cross section of the individual STXS bins, or the inclusive cross section, are removed from the fit.

6 Summary

Measurements of the Standard Model Higgs boson production cross section, where the Higgs boson is produced in association with a vector boson and decays to bottom quark pairs and the vector boson decays into electrons, muons, or neutrinos, have been presented. Proton-proton collision data collected by the CMS experiment during 2016, 2017, and 2018 at $\sqrt{s} = 13$ TeV were used, corresponding to an integrated luminosity of 138 fb^{-1} .

7 Acknowledgments

This analysis would not have been possible without sincere cooperation and help from the CMS group in Zagreb led by Dr. Vuko Brigljevic. I also would like to thank the members of $VH, H \rightarrow b\bar{b}$ analysis working group in CMS and finally each member of CMS collaboration whose collective efforts towards the collaboration made this analysis a success. This work has been supported in part by the Croatian Science Foundation under the project IP-2016-06-3321.

References

1. CMS Collaboration, Phys. Lett. B **805** (2020) 135425.
2. ATLAS Collaboration, arXiv: 2207.00320
3. CMS Collaboration, Phys. Rev. Lett. **121** (2018) 121801.
4. ATLAS Collaboration, Phys. Lett. B **786** (2018) 59-86.
5. LHC Higgs Cross Section Working Group Collaboration, Handbook of LHC Higgs Cross Sections: 4. Deciphering the Nature of the Higgs sector, technical report, (2016).
6. M. Cacciari *et. al* JHEP **04** (2008) 063
7. CMS Collaboration, JINST **13** (2018)
8. CMS Collaboration, CMS Detector Performance Note CMS-DP-2020-025, 2020.

Extraction of $|V_{ub}|$ from $B \rightarrow \pi\ell\nu$ modes.

Ipsita Ray

Indian Institute of Technology Guwahati, Guwahati 781039, Assam, India

Abstract

The Cabibbo-Kobayashi-Maskawa (CKM) element V_{ub} , which is the least precisely known element till date is an important input parameter for the theoretical predictions of several observables in the flavor sector and it is responsible for the CP violating phase within the Standard Model. There exists a long standing tension between the tree-level determinations from the inclusive $B \rightarrow X_u\ell\nu$ decays (where X_u refers to sum over all final state hadrons containing an up quark) and exclusive decays like $B \rightarrow \pi\ell\nu$. We have re-analyzed all the available inputs (data and theory) on the $B \rightarrow \pi\ell\nu$ decays including the newly available inputs on the form-factors from light cone sum rule (LCSR) and Lattice QCD approach. We have compared the results with the procedure taken up by the Heavy Flavor Averaging Group (HFLAV), while commenting on the effect of outliers on the fits. Our best results for $|V_{ub}|^{exc.}$ are consistent with the most recent estimate for $|V_{ub}|^{inc.}$ from Belle-II within 1σ confidence interval.

1 Introduction

The tree level semileptonic $b \rightarrow u\ell\nu_\ell$ ($\ell = e, \mu$) decays are useful probes for extracting the CKM element $|V_{ub}|$. In this regard, both exclusive decays ($B \rightarrow \pi\ell\nu$), and inclusive decays ($B \rightarrow X_u\ell\nu_\ell$) play important roles. At present, the extracted values as given in [1] are in mutual disagreement (by $\sim 2.2\sigma$). Unlike the inclusive determination of $|V_{cb}|$ from $B \rightarrow X_c\ell\nu_\ell$, the inclusive determination of $|V_{ub}|$ is not clean. The large background from the $b \rightarrow c\ell\nu$ decays necessitates experimental cuts to distinguish $b \rightarrow u$ from $b \rightarrow c$ transitions which forces us to a corner of the phase-space region where usual OPE cannot be applied. One has to rely on the non-perturbative QCD shape functions instead of the heavy quark expansion parameters which complicates the theoretical interpretation of the measurement. These shape functions are modelled using various approaches which renders the extracted values of $|V_{ub}|$ model dependent. In a very recent analysis of the inclusive spectra with hadronic-tagging, Belle has extracted the value of $|V_{ub}|$

by four different methods. By taking an arithmetic average of these four different values from the four different methods, they obtain $|V_{ub}|^{inc.} = (4.10 \pm 0.09 \pm 0.22 \pm 0.15) \times 10^{-3}$ which is the most precise measurement till date.

The extraction of $|V_{ub}|$ from $B \rightarrow \pi l \nu$ is also not very clean. The methodology adopted by the Heavy Flavor Averaging Group (HFLAV) involves a two-stage procedure for the extraction of $|V_{ub}|^{exc.}$. In the first stage, using the available data on the differential $B \rightarrow \pi l \nu$ decay rates from BaBar(11) [2], Belle(11) [3], BaBar(12) [4], and Belle(13) [5], they obtain an average squared four-momentum transfer (q^2) spectrum from a binned maximum-likelihood fit. As presented in their review [6], the quality of this fit is not good, and the p -value is around 6%. In the second fit, this average q^2 spectrum along with the lattice and LCSR (at $q^2 = 0$) inputs had been used to extract $|V_{ub}|$ which is a reasonably good fit with p -value $\sim 47\%$. After repeating a similar fit mentioned above to obtain the average q^2 spectrum, we have arrived at an even worse quality of fit with a p value $< 1\%$. In any case, a frequentist fit of probability $< 5\%$ is usually considered to be of negligible significance and any further fit (in the second stage), using the outcome of this very low-significance fit may lead to biased predictions for $|V_{ub}|$. It thus becomes essential to reconsider other possible ways of analyzing the available data and pin-point the source of tension in the fits and also the reason for the discrepancy between exclusive and inclusive determinations.

2 Motivation

2.0.1 Theoretical Background

The differential decay width w.r.t. q^2 for a pseudoscalar to pseudoscalar semileptonic decay for eg. $\bar{B}^0 \rightarrow \pi^+ l^- \bar{\nu}_l$ is a function of the form factors $f_{+,0}(q^2)$ ¹:

$$\frac{d\Gamma}{dq^2} (\bar{B}^0 \rightarrow \pi^+ l^- \bar{\nu}_l) = \frac{G_F^2 |V_{ub}|^2}{24\pi^3 m_{B^0}^2 q^4} (q^2 - m_l^2)^2 |p_\pi(m_{B^0}, m_{\pi^+}, q^2)| \times \left[\left(1 + \frac{m_l^2}{2q^2} \right) m_{B^0}^2 |p_\pi(m_{B^0}, m_{\pi^+}, q^2)|^2 |f_+(q^2)|^2 + \frac{3m_l^2}{8q^2} (m_{B^0}^2 - m_{\pi^+}^2)^2 |f_0(q^2)|^2 \right]. \quad (1)$$

where $|p_\pi(m_B, m_\pi, q^2)| = \sqrt{\lambda(m_B, m_\pi, q^2)}/2m_B$ with $\lambda(m_B, m_\pi, q^2) = ((m_B - m_\pi)^2 - q^2)((m_B + m_\pi)^2 - q^2)$. Therefore, to extract $|V_{ub}|$, we need information on the form-factors at different values of q^2 which are obtained from non-perturbative techniques like lattice-QCD and LCSR. At present the lattice estimates are available on $f_{+,0}(q^2)$ at zero and non-zero recoils [7, 8]. While RBC-UKQCD [7] provides synthetic data points for $f_{+,0}(q^2)$ with full covariance matrices (both systematic and statistical) at $q^2 = 19, 22.6, 25.1 \text{ GeV}^2$, Fermilab-MILC [8] only provides the fit-results for their coefficients. Using the results of the ‘only lattice’ fit, we generate correlated synthetic data-points at exactly the same q^2 values as RBC-UKQCD, with an extra point for f_+ at $q^2 = 20.5 \text{ GeV}^2$. There is also a recent update on the values of these form-factors at zero and non-zero values of q^2 [9]. The form factors serve as major sources of uncertainties in the extraction of $|V_{ub}|$. To get the shape of the decay rate distribution, one needs to know the shape of the corresponding form-factors in the whole q^2 region. Thus, it is crucial to have a parametrization of $f_{+,0}(q^2)$ that satisfies real analyticity in the complex q^2 plane. For the form-factor parametrization, we have followed two different approaches which are known as Bourrely-Caprini-Lellouch (BCL) [10] and Bharucha-Straub-Zwicky (BSZ) [11] parametrization and compared their results.

¹The corresponding charged B will decay to a neutral pion and hence will be scaled by a factor of $1/2$ at the decay width level since $\pi^0 = \frac{u\bar{u} - d\bar{d}}{\sqrt{2}}$

According to BCL, f_+ and f_0 are as follows:

$$f_+(z) = \frac{1}{1 - q^2/m_{B^*}^2} \sum_{n=0}^{N_z-1} b_n^+ [z^n - (-1)^{n-N_z} \frac{n}{N_z} z^{N_z}], \quad f_0(z) = \sum_{n=0}^{N_z-1} b_n^0 z^n. \quad (2)$$

Here, $b_n^{0/+}$ are the coefficients of the expansion which are free parameters and they obey the unitarity constraint as can be seen from [8], [10]. The conformal map from q^2 to z is given by: $z(q^2) = \frac{\sqrt{t_+ - q^2} - \sqrt{t_+ - t_0}}{\sqrt{t_+ - q^2} + \sqrt{t_+ - t_0}}$ where $t_{\pm} \equiv (m_B \pm m_{\pi})^2$ and $t_0 \equiv t_+(1 - \sqrt{1 - t_-/t_+})$. t_0 is a free parameter that governs the size of z in the semileptonic phase space. For BSZ, the parametrization of any form-factor reads:

$$f_i(q^2) = \frac{1}{1 - q^2/m_{R,i}^2} \sum_{k=0}^N a_k^i [z(q^2) - z(0)]^k, \quad (3)$$

where $m_{R,i}$ denotes the masses of sub-threshold resonances compatible with the quantum numbers of the respective form factors and a_k^i s are the coefficients of expansion. The details are provided in [11].

In BSZ, the kinematical constraint $f_+(q^2 = 0) = f_0(q^2 = 0)$ directly leads to the relation $a_0^+ = a_0^0$ between the coefficients, whereas in the BCL parametrization, the same kinematic constraint leads to a complex relationship between the expansion coefficients: $b_3^0 = 45.70(b_0^+ - b_0^0) - 12.78b_1^0 - 3.58b_2^0 + 12.85b_1^+ + 3.44b_2^+ + 1.21b_3^+$. Here, we have replaced b_3^0 in terms of the other coefficients in the fit. This helps us reduce one parameter from the fit.

2.0.2 Comparison with existing literature

As discussed in the introduction, we have repeated the binned maximum-likelihood fit to obtain the average q^2 -spectrum, which is consistent with that from HFLAV within 1σ . However, our fit quality is about 1 % while that for HFLAV is about 6 %. This difference in the fit quality could be due to the non-availability of the information on the shared systematic uncertainties between measurements (like continuum subtraction, tracking efficiency, etc.) as used by HFLAV in their analysis. Thus, in order to look for a possibility of improvement in the fit-quality, one should carefully inspect all the datasets. A closer look at the data shows that BaBar(11) untagged analysis of the $B^{0,+}$ modes [2] have much lower statistics/yield (almost half) than the one published in the next year: BaBar(12) [4]. Also, in 2011, the event selection has been optimized over the signal-enhanced region instead of the entire fit region and this analysis uses only a subset of the full BaBar data-set. The analysis method in BaBar(11) is also considerably different from the analyses by Belle. Therefore, we drop the BaBar(11) datapoints in 6 q^2 -bins as a first attempt to look for the possibility of improvement while extracting the average partial branching fraction in each q^2 interval from a binned maximum-likelihood fit to data, leading to an improvement in the fit quality from 1% to 24.8%. This reinforces the fact that the data from BaBar (11) is quite at odds with all other data-sets (Please refer to ref [12] for more details.)

3 Main results

To understand the effect of the inconsistency in data on the decay rate distributions, we have derived the $B \rightarrow \pi \ell \nu$ decay rate distributions using the form-factors extracted only from the LCSR and lattice inputs in both the BSZ [11] and BCL [10] expansions. We have truncated both f_0 and f_+ at $N = 3$, thus leading to seven parameters (4 for f_+ and 3 for f_0). We have used the latest $|V_{ub}|^{inc}$ value from Belle to get the shape and height of the distribution which will help us understand the reason for the discrepancy between the inclusive and exclusive determinations. Using the fit results for the parameters and $|V_{ub}|$

from different inclusive estimates, if we calculate the theoretical predictions of the binned branching fractions, then any large deviation of the predictions from the actual measurements could potentially diagnose the source of the apparent tension between $|V_{ub}|^{\text{inc.}}$ and $|V_{ub}|^{\text{exc.}}$. From figure 1, we observe that the q^2 distribution of the differential branching fraction in both the form-factor parametrizations can explain almost all the available data except a few which are lying entirely outside of the theoretical C.I. bands. For more details, the interested reader is referred to [12].

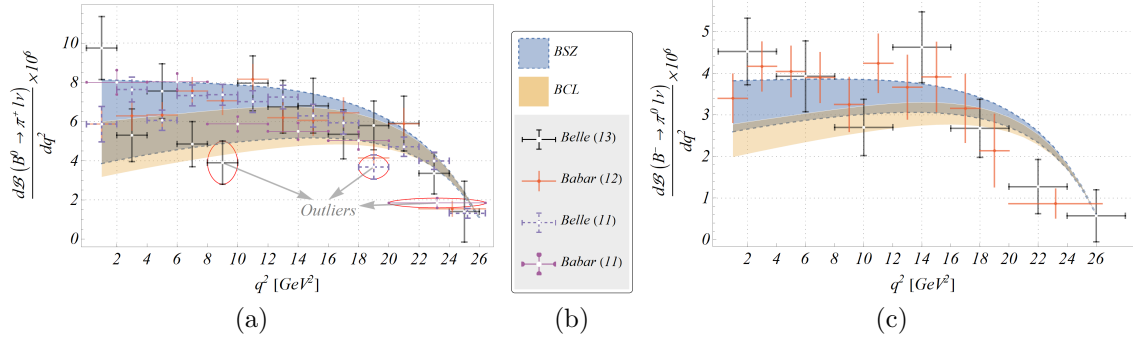


Figure 1: Differential branching fraction plots superposed on experimental data-points, with form factors fitted from lattice and LCSR, and $|V_{ub}|$ corresponds to that obtained from the latest Belle Inclusive Measurement [13].

In our opinion, instead of extracting $|V_{ub}|$ through a two-stage procedure for which the first fit is of very poor quality, we should directly use the individual data-points for a simultaneous extraction of $|V_{ub}|$ and the parameters corresponding to the chosen form-factor parametrization. This provides us with a single value for the fit probability to draw our inference from instead of a two stage fit. The different fit scenarios are as given below:

- **Fit 1:** B^0 decays from Belle (2011) and Belle (2013); B^- decays from Belle(2013); the combined modes from BaBar (2011) and BaBar (2012).
- **Fit 2:** B^0 decays from Belle (2011), BaBar (2012), and Belle (2013); B^- decays from BaBar (2012) and Belle(2013).
- **Fit 3:** The combined modes from BaBar (2011) along with the *Fit 2* dataset.

In table 1, we have shown the extracted values of $|V_{ub}|$ in different fit scenarios with full datasets and also after dropping the data-points having pulls greater than 2, shown in the right panel of the same table. ‘Fit A’s are with experimental data + Lattice inputs, whereas ‘Fit B’s are with experimental data + Lattice + LCSR inputs. As can be seen from table 1, in all the scenarios, the fit quality as well as the extracted $|V_{ub}|$ increases by a considerable amount on dropping a few data-points with pull > 2 . This indicates that the data with large ‘pull’ have an impact on the extracted values of $|V_{ub}|$ too. Fig 1 shows that the partial decay rates $\mathcal{B}(B^0 \rightarrow \pi^-)^{[20,26.4]}$ (BaBar(11)), $\mathcal{B}(B^0 \rightarrow \pi^-)^{[18,20]}$ (Belle(11)) and $\mathcal{B}(B^0 \rightarrow \pi^-)^{[8,10]}$ (Belle(13)) have pull > 2 . However, $\mathcal{B}(B^0 \rightarrow \pi^-)^{[8,10]}$ (Belle(13)) has a rather minor effect on $|V_{ub}|$.

On the basis of these observations, we define a few additional scenarios:

- **Fit 2B-I:** Input used in *Fit 2B* without the data on $\mathcal{B}(B^0 \rightarrow \pi^-)^{[18,20]}$ (Belle 2011).
- **Fit 3B-I:** Input used in *Fit 3B* without the data on $\mathcal{B}(B^0 \rightarrow \pi^-)^{[20,26.4]}$ (BaBar 2011).

BSZ Parametrization								
Run Name	Full				Dropped Pull > 2			
	χ^2_{\min}/DOF	$p\text{-value}(\%)$	$V_{ub} \times 10^3$		χ^2_{\min}/DOF	$p\text{-value}(\%)$	$V_{ub} \times 10^3$	
			Frequentist	Bayesian			Freq.	Bayes
Fit 1A	73.4/56	5.92	3.69(14)	3.67(14)	46.6/52	68.68	3.79(15)	3.77 ($^{15}_{16}$)
Fit 1B	77./65	14.57	3.74(13)	3.73 ($^{13}_{14}$)	49.3/61	85.77	3.83(14)	3.82 ($^{14}_{16}$)
Fit 2A	59.5/61	53.17	3.81(14)	3.79(15)	46./59	89.26	3.86(15)	3.85 ($^{15}_{16}$)
Fit 2B	62./70	74.23	3.85(14)	3.83 ($^{13}_{15}$)	48.3/68	96.63	3.91(14)	3.89 ($^{14}_{15}$)
Fit 3A	82.2/67	9.98	3.70(14)	3.69(14)	53.3/62	77.56	3.76(14)	3.76 ($^{15}_{14}$)
Fit 3B	85.9/76	20.54	3.75(13)	3.74 ($^{13}_{14}$)	62./73	81.79	3.84(14)	3.83(14)

BCL Parametrization								
Run Name	Full				Dropped Pull > 2			
	χ^2_{\min}/DOF	$p\text{-value}(\%)$	$V_{ub} \times 10^3$		χ^2_{\min}/DOF	$p\text{-value}(\%)$	$V_{ub} \times 10^3$	
			Freq.	Bayes			Freq.	Bayes
Fit 1A	73.5/56	5.84	3.69(14)	3.67 ($^{13}_{15}$)	46.7/52	68.34	3.79(15)	3.78(15)
Fit 1B	92.1/65	1.51	3.79(13)	3.78 ($^{13}_{13}$)	63.2/61	39.84	3.89(14)	3.87 ($^{14}_{15}$)
Fit 2A	60.1/61	50.8	3.81(14)	3.81(15)	46.5/59	88.19	3.87(15)	3.85 ($^{14}_{15}$)
Fit 2B	75.9/70	29.42	3.91(14)	3.90(15)	58.3/67	76.64	3.96(14)	3.96 ($^{16}_{14}$)
Fit 3A	82.7/67	9.35	3.70(14)	3.69 ($^{13}_{14}$)	57.8./63	66.09	3.77(14)	3.76(15)
Fit 3B	101.4/76	2.73	3.80(13)	3.79 ($^{13}_{15}$)	76.3/73	37.27	3.90(14)	3.89 ($^{14}_{15}$)

Table 1: Freq. and Bayesian

- **Fit 3B-II**: Input used in *Fit 3B* without the data on $\mathcal{B}(B^0 \rightarrow \pi^-)^{[18,20]}$ (Belle 2011) and $\mathcal{B}(B^0 \rightarrow \pi^-)^{[20,26.4]}$ (BaBar 2011).

Fit Scenario	BSZ				BCL			
	χ^2/DOF	$p\text{-value}(\%)$	$V_{ub} \times 10^3$		χ^2/DOF	$p\text{-value}(\%)$	$V_{ub} \times 10^3$	
			Frequentist	Bayesian			Frequentist	Bayesian
<i>F2B-I</i>	55.4/69	88.14	3.90(14)	3.89 $^{+0.14}_{-0.15}$	68.85/69	48.25	3.96(14)	3.95 $^{+0.14}_{-0.15}$
<i>F3B-I</i>	78.86/75	35.8	3.83(14)	3.83(13)	93.6/75	7.19	3.89(14)	3.89(14)
<i>F3B-II</i>	72.96/74	51.25	3.88(14)	3.87 $^{+0.14}_{-0.15}$	87.2/74	13.99	3.94(14)	3.93 $^{+0.14}_{-0.15}$

Table 2: Final table of comparison for $|V_{ub}|^{exc.}$ obtained in this work.

From table 2, we notice that even in the presence of other outliers, i.e. data-points which do not fit comfortably with other data, the most influential data-points in determining the estimate of $|V_{ub}|^{exc.}$ are the partial branching fractions $\mathcal{B}(B^0 \rightarrow \pi^-)^{[18,20]}$ (Belle(11)) and $\mathcal{B}(B^0 \rightarrow \pi^-)^{[20,26.4]}$ (BaBar(11)).

4 Summary

We have extracted $|V_{ub}|$ analyzing all the available inputs on the exclusive $B \rightarrow \pi l \nu$ decays. This includes the data on the partial branching fractions and inputs from lattice and LCSR. We have commented on some of the issues of the earlier fits carried out by HFLAV. After repeating the analysis similar to HFLAV,

we have arrived at a fit with very low probability for the average q^2 spectrum at the first stage. We have identified BaBar(11) data (at least a part of it) as a probable source of such a bad quality fit. We simultaneously fit all the data (instead of a two-stage fit) after defining different fit scenarios. In this process, we have identified outliers, i.e. data-points inconsistent with the others. The goal is to check if some of these outliers are also influential in the extraction of $|V_{ub}|$. We have found a few data-points that compromise the fit-quality, and at the same time, influence the extraction of $|V_{ub}|$. Our best result $|V_{ub}| = (3.94(14)) \times 10^{-3}$ is consistent with the one extracted from inclusive $B \rightarrow X_u \ell \nu_\ell$ decays from Belle within 1σ .

References

1. “Semileptonic b-hadron decays, determination of V_{cb} , V_{ub} ,” <https://pdg.lbl.gov/2020/reviews/rpp2020-rev-vcb-vub.pdf>.
2. P. del Amo Sanchez *et al.*, “Study of $B \rightarrow \pi \ell \nu$ and $B \rightarrow \rho \ell \nu$ Decays and Determination of $|V_{ub}|$,” *Phys. Rev. D*, vol. 83, p. 032007, 2011.
3. H. Ha *et al.*, “Measurement of the decay $B^0 \rightarrow \pi^- \ell^+ \nu$ and determination of $|V_{ub}|$,” *Phys. Rev. D*, vol. 83, p. 071101, 2011.
4. J. Lees *et al.*, “Branching fraction and form-factor shape measurements of exclusive charmless semileptonic B decays, and determination of $|V_{ub}|$,” *Phys. Rev. D*, vol. 86, p. 092004, 2012.
5. A. Sibidanov *et al.*, “Study of Exclusive $B \rightarrow X_u \ell \nu$ Decays and Extraction of $\|V_{ub}\|$ using Full Reconstruction Tagging at the Belle Experiment,” *Phys. Rev. D*, vol. 88, no. 3, p. 032005, 2013.
6. Y. S. Amhis *et al.*, “Averages of b-hadron, c-hadron, and τ -lepton properties as of 2018,” 9 2019.
7. J. M. Flynn, T. Izubuchi, T. Kawanai, C. Lehner, A. Soni, R. S. Van de Water, and O. Witzel, “ $B \rightarrow \pi \ell \nu$ and $B_s \rightarrow K \ell \nu$ form factors and $|V_{ub}|$ from 2+1-flavor lattice QCD with domain-wall light quarks and relativistic heavy quarks,” *Phys. Rev. D*, vol. 91, no. 7, p. 074510, 2015.
8. J. A. Bailey *et al.*, “ $|V_{ub}|$ from $B \rightarrow \pi \ell \nu$ decays and (2+1)-flavor lattice QCD,” *Phys. Rev. D*, vol. 92, no. 1, p. 014024, 2015.
9. N. Gubernari, A. Kokulu, and D. van Dyk, “ $B \rightarrow P$ and $B \rightarrow V$ Form Factors from B -Meson Light-Cone Sum Rules beyond Leading Twist,” *JHEP*, vol. 01, p. 150, 2019.
10. C. Bourrely, I. Caprini, and L. Lellouch, “Model-independent description of $B \rightarrow \pi \ell \nu$ decays and a determination of $|V_{ub}|$,” *Phys. Rev. D*, vol. 79, p. 013008, 2009, [Erratum: *Phys.Rev.D* 82, 099902 (2010)].
11. A. Bharucha, D. M. Straub, and R. Zwicky, “ $B \rightarrow V \ell^+ \ell^-$ in the Standard Model from light-cone sum rules,” *JHEP*, vol. 08, p. 098, 2016.
12. A. Biswas, S. Nandi, S. K. Patra, and I. Ray, “A closer look at the extraction of $|V_{ub}|$ from $B \rightarrow \pi \ell \nu$,” *JHEP*, vol. 07, p. 082, 2021.
13. L. Cao *et al.*, “Measurements of Partial Branching Fractions of Inclusive $B \rightarrow X_u \ell^+ \nu_\ell$ Decays with Hadronic Tagging,” *Phys. Rev. D*, vol. 104, no. 1, p. 012008, 2021.

MEASUREMENT OF THE HELIUM FLUX IN THE LOW EARTH ORBIT WITH THE ALPHA MAGNETIC SPECTROMETER

Gülce Karagöz on behalf of the AMS Collaboration

Middle East Technical University, Üniversiteler Mahallesi, Dumlupınar Bulvarı No:1 06800 Çankaya Ankara/TURKEY
E-Mail: gulce.karagoz@metu.edu.tr

Abstract

The Alpha Magnetic Spectrometer (AMS) is a state-of-art particle physics detector on the International Space Station (ISS). From 19th May 2011 when it was installed up to now, AMS has collected more than 200 billion cosmic ray events. AMS aims to search for dark matter and anti-matter as well as understand the propagation and acceleration mechanisms of charged cosmic rays, one of which is the helium (He) nucleus. He is the second most abundant nucleus, with an abundance of 12%. Moreover, the interaction cross-section of He with the interstellar medium is remarkably smaller than heavier nuclei, resulting in He travelling much larger distances and reaching us from the far edges of the galaxy. This work presents properties of the time dependence of the He flux and the correlation of the He flux with solar variations.

1 Alpha Magnetic Spectrometer Experiment

The Alpha Magnetic Spectrometer (AMS) is a particle physics detector in space with a high precision and accuracy. The minimal material usage in the detector prevents the detector from becoming a large angle scattering source. One of the physical objectives of AMS is reaching a sensitivity in ratio of He/anti-He $> 10^{10}$ for anti-matter search. As far as dark matter is concerned, AMS provides a sensitive research in the positron channel with a 10^6 proton rejection power ¹⁾. AMS consists of different sub-detectors, each of which has its functionalities, which are Transition Radiation Detector (TRD), Time of Flight (ToF), Silicon Tracker (ST), Ring Image Cherenkov detector (RICH) and Electromagnetic CALorimeter (ECAL), which can be seen in Figure 1. TRD uses the phenomenon which is called *Transition Radiation (TR)* in which x-rays are emitted when a charged particle crosses between two mediums with different dielectric constants ²⁾. Light charged particles, such as electrons and positrons in the momentum range 10 – 300 GeV/c, have a higher chance of emitting a TR photon when compared with protons and anti-protons, which enables the separation of electrons and positrons from protons and anti-protons ³⁾. ToF

detector is responsible for measuring the charge and velocity of the particle. It also provides a fast trigger to the detector and consists of four layers of scintillator counters, two of which are located between TRD and ST (*Upper ToF*) and the other two are located between ST and RICH (*Lower ToF*). By combining the signals coming from upper and lower planes, ToF can measure the time of flight of the particle $\Delta(t)$ and the trajectory length of the particle $\Delta(s)$ coming from ST. By using $\beta = \frac{\Delta(s)}{c\Delta(t)}$ the velocity of the particle can be determined ⁴⁾. ST determines the trajectory of the particle. It consists of nine layers. *Layer1 (L1)* and *Layer9 (L9)* are called *external layers* since they are located externally and layers from *Layer2 (L2)* to *Layer8 (L8)* are called *inner tracker layers*. ST measures the *rigidity* of the particle, which is denoted as $R = p/Z$ where p is the momentum of the particle and Z is the charge of the particle. In addition to measurement of rigidity, ST can also identify elements by using the energy deposition $\frac{dE}{dt}$ of the particle ⁵⁾. RICH detector is located between lower ToF and ECAL. It employs the *Cherenkov radiation* phenomena. According to this, when a charged particle with velocity v enters a medium with index n , it emits a radiation if its velocity is $v > \frac{c}{n}$, where c is the speed of light. RICH is responsible for measuring the charge and velocity of the particle ⁶⁾. Lastly, ECAL is responsible for measuring the energy of the particle and thanks to its granular structure it can separate positrons from protons in the GeV-TeV energy region. Also, it can provide a direct measurement for high-energy photons ⁷⁾.

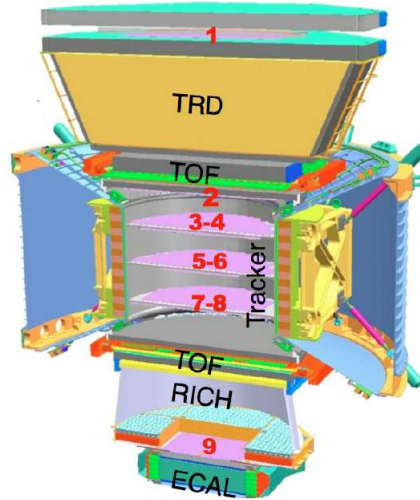


Figure 1: Display of AMS Subdetectors

In the full span configuration L9 is also included in the analysis and the maximum detectable rigidity configuration is reached. In this configuration, helium enters the detector from L1 and moves through the whole detector. Inside the inner tracker it bends due to the magnetic field applied and before quitting the detector it also hits L9. By reconstruction, one can identify the trajectory of helium in the detector.

2 Solar Modulation

Sun has a magnetic field that is called *solar magnetic field*, and this field is created by the continual generation of energy and heating, which results in convection and differential rotation of the outer plasma. Changes in the solar magnetic field and the field itself are the reasons for the *active solar regions*, *flares*, *jets* and *coronal mass ejections (CMEs)*. Figure 2 shows the structure of the Sun. In the regions *core* and *radiative zone*, the Sun rotates like a rigid body. In the *convection zone*, the Sun rotates faster

at the equator than at the poles, which results in a differential rotation. Since the plasma around the equator tends to move faster than the rest, the probability of occurrence of the active regions at mid-latitudes is higher. The Sun returns the same solar magnetic field configuration about every 22 years; this periodicity is one of the major ones. A solar minima occur when the solar magnetic field axis is

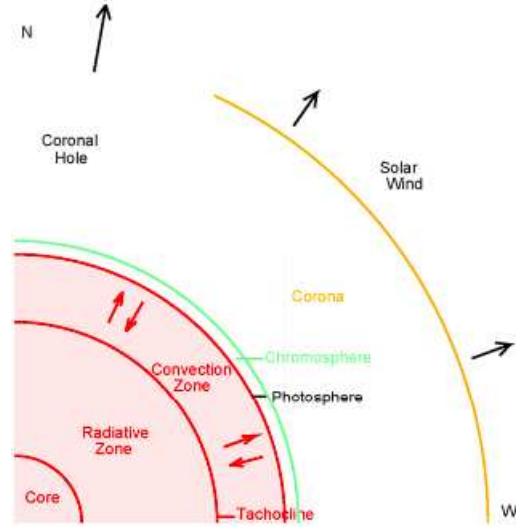


Figure 2: Structure of the Sun

aligned with the solar rotation axis. In the times between these periods, solar maxima occur. When the Sun is at its maxima, the number of CMEs ejected is increased, which blocks and decreases the *Galactic Cosmic Rays (GCRs)* entering the heliosphere⁸⁾. The decrease of the GCR observed from the Earth is called the *Forbush decrease*. Variations that resulted in the Forbush decrease can be either recurrent or non-recurrent variations. The *Heliospheric Current Sheets (HCSs)* and high-speed plasma flow from coronal holes are examples of these recurrent variations, whereas CMEs are examples of non-recurrent variations in the interplanetary medium⁹⁾.

3 Helium Flux Measurement

For He flux calculation, the first step is the selection of the data samples. Only those acquired when AMS is in normal operating conditions are considered for the analysis. The detector should be pointing 40° of the local zenith, and ISS should be outside the South Atlantic Anomaly¹⁰⁾. After this general selection process, selections specified for the relevant nuclei are applied, and the sample to be analyzed is obtained. With these choices, Helium flux Φ_i in the corresponding time binnings can be expressed as equation 1

$$\Phi_i = \frac{N_i}{A_i \epsilon_i T_i \Delta R_i} \quad (1)$$

where i denotes the i^{th} rigidity bin in the rigidity interval $(R_i, R_i + \Delta R_i)$, N_i denotes the number of helium events selected, A_i is the effective acceptance, ϵ_i is the trigger efficiency and T_i is the time that detector collected events. Remembering that the short-scale variations are either recurrent or non-recurrent, it is expected that this behaviour should be clearly visible for the low-energy helium flux. The non-recurrent variations resulting from CMEs increase towards the solar maxima since the number of

CMEs is also increasing. The recurrent variations due to the synodic solar rotation are with a period of 27 days and its multiple frequencies such as 13.5 and 9 days. Recurrent variations are related to the passage of *Corotating Interaction Regions (CIRs)*. Daily helium flux exhibits variations and the relative magnitude of these variations decreases with increasing rigidity and low rigidities; recurrent variations are visible 11).

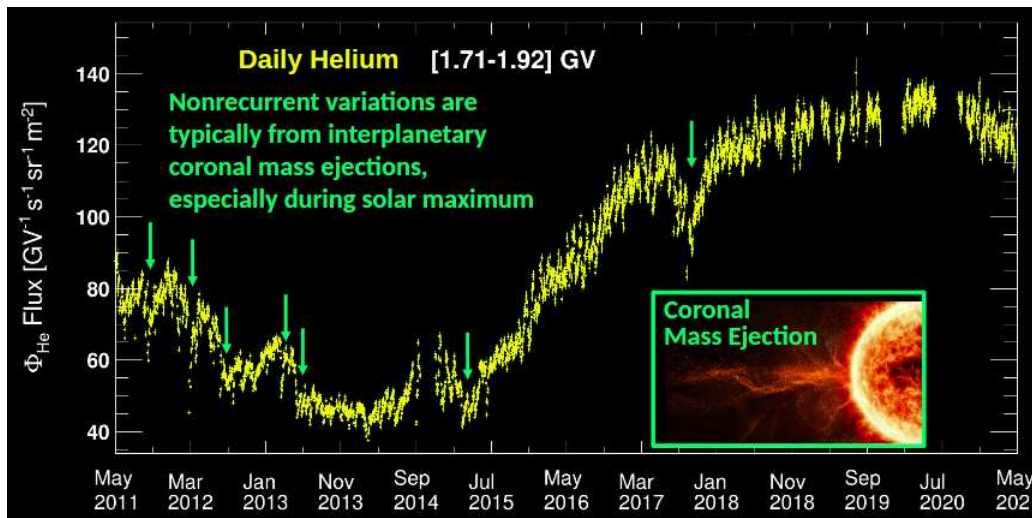


Figure 3: Effect of non-recurrent variations for helium flux in the rigidity bin 1.71-1.92GV

From figure 3 one can see the effect of CMEs indicated with green arrows on the helium flux data. Since the number of CMEs increases towards the solar maximum, we expect a more significant impact on the flux during these periods. We can see that towards the solar maximum, which occurred in April 2014, the effects of CMEs are bigger than ones close to the solar minima.

During the gradual increase in the flux from July 2015 to March 2017 one sees the effect of recurrent variations, which is due to the passage of CIRs, that is related to the synodic motion of the Sun. CIRs are produced by interacting fast solar wind with a slower speed solar wind. The strength of periodicities is time and energy-dependent.

As the Forbush effect suggests, when the activity of the Sun increases, the observed flux from the Earth decreases. Since the increase in the activity of the Sun is directly proportional to the sunspot number, the flux and the sunspot number should be anti-correlated. Figure 4 shows the relation in the same energy bins as figure 3 but with the sunspot number overlaid: the anti-correlation between the observed flux and the sunspot number can be seen. The decrease in the helium flux starts from 2011 and it continues until the latest solar maximum that is occurred at 2014 and after that time, the flux starts to increase up to the latest solar minimum occurring at the very beginning of 2021. AMS data correlates very well with the physics expectations.

4 Conclusion

Helium is the second most abundant charged nucleus in the cosmic ray composition and has the smallest interaction cross-section with the interstellar medium, which enables helium to propagate from the far edges of the galaxy. Understanding the source, propagation and acceleration mechanism of helium with AMS, a high precision particle physics detector on ISS, is very important. The outcome is deeply

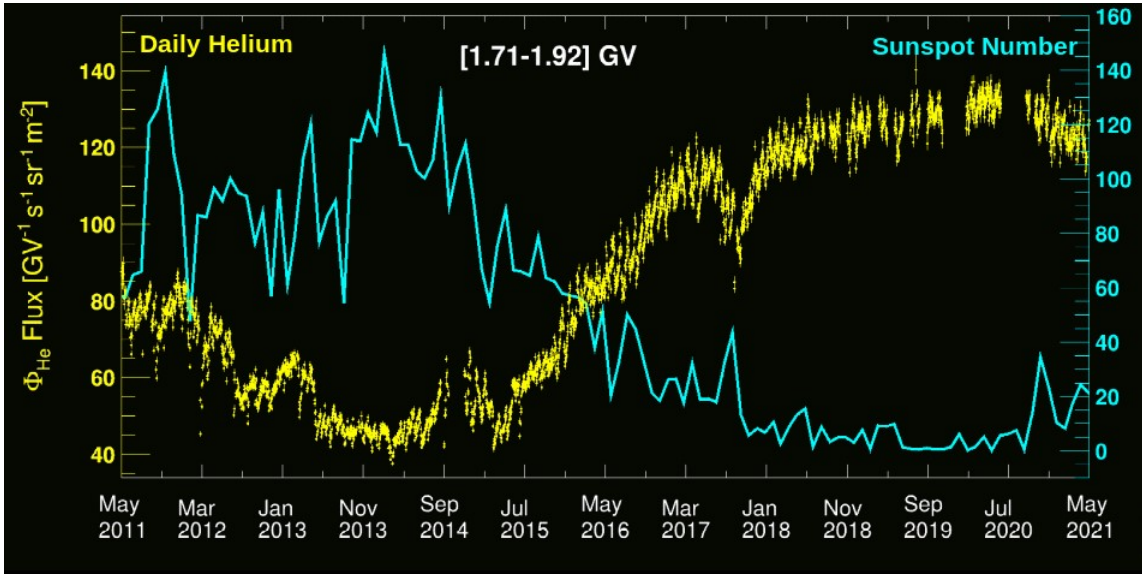


Figure 4: Anti-correlation between sunspot number and the helium flux for the rigidity bin 1.71-1.92GV

correlated with physics phenomena. Observing and predicting solar modulations will benefit both new outcomes in high energy physics and dose predictions for future space missions.

5 Acknowledgements

I would like to express my deep thanks to my advisor Prof.M.Bilge Demirköz for leading to participate in this valuable summer school and for her guidance while preparing this work. I want to thank Prof.Samuel C.C. Ting for letting me be a participant in AMS collaboration. I would like to thank the AMS collaboration, especially to Yi Jia and Cristina Consolandi, for helping me conduct this work. I would like to acknowledge that this work is supported by Turkish Atomic Energy Authority (TAEK) (Grant No:2020TAEK(CERN)A5.H1.F5-26).

References

1. S.Ting, The Alpha Magnetic Spectrometer on the International Space Station, Nuclear Physics B - Proceedings Supplements **243–244**, 12-24, (2013).
2. V.L.Ginzburg, Transition Radiation and Transition Scattering, Physica Scripta **T2A**, 182-191, (1982).
3. F.Hauler et al., The AMS-02 TRD for the international space station, IEEE Transactions on Nuclear Science **51**, 1365-1372, (2004).
4. V.Bindi et al., The AMS-02 time of flight (TOF) system: construction and overall performances in space., Conference: 33rd International Cosmic Ray Conference, Rio de Janeiro 2013 The Astroparticle Physics Conference, (2013).
5. D.Haas, The Silicon Tracker of AMS02, Nuclear Instruments and Methods in Physics Research Section A: Accelerators, Spectrometers, Detectors and Associated Equipment, **530**, 173-177, (2004).

6. F.Giovacchini et al., The AMS-02 RICH detector: Status and physics results, Nuclear Instruments and Methods in Physics Research Section A: Accelerators, Spectrometers, Detectors and Associated Equipment, **952**, 161797, (2020).
7. M.Vecchi et al., The electromagnetic calorimeter of the AMS-02 experiment, (2012)
8. D.V.Reames, Solar Energetic Particles II, A Modern Primer on Understanding Sources, Acceleration and Propagation, Second Edition, (2020).
9. A.V.Belov et al., What Determines the Magnitude of Forbush Decreases?, Advances in Space Research, **27**, 625-630, (2001).
10. M.Aguilar et al., Precision Measurement of the Helium Flux in Primary Cosmic Rays of Rigidities 1.9 GV to 3 TV with the Alpha Magnetic Spectrometer on the International Space Station, Physical Review Letters, **115**, (2015)
11. M.Aguilar et al., Properties of Daily Helium Fluxes, Physical Review Letters, **128**, (2022)

GAUGING THE BARYONIC AND LEPTON FAMILY NUMBERS WITH HARMLESS WESS-ZUMINO TERM

Claudio Toni

*Physics Department and INFN Sezione di Roma La Sapienza,
Piazzale Aldo Moro 5, 00185 Roma, Italy*

Abstract

We show how to devise an anomaly-free UV completion for the gauging of the Standard Model accidental symmetries with mostly chiral heavy fermions such that anomalous Wess-Zumino terms are suppressed in the IR. This relaxes would-be strong bounds from the longitudinal emission of light vectors coupled to non-conserved currents. We report the results of ¹⁾, where we classify such scenarios and show that they will be extensively probed at the high-luminosity phase of the LHC via the measurement of the $h \rightarrow Z\gamma$ rate and the direct search for non-decoupling charged leptons.

1 Introduction

The physics of light spin-1 dark bosons has raised an increased interest in the recent years, both from a theoretical and phenomenological point of view. A theoretically motivated model is provided by the gauging of a new abelian symmetry. In a minimal scenario with the assumption that all SM Yukawa operators are allowed in the quark sector at the renormalizable level, the most general abelian symmetry we can write is a linear combination of the accidental global symmetries of the SM, that is baryon number $U(1)_B$ and family lepton number $U(1)_{L_i}$ (with $i = e, \mu, \tau$).

Within the SM field content, the only anomaly free combinations turn out to be $L_i - L_j$ ^{2, 3, 4}. Hence, in order to consistently gauge a general linear combination

$$X = \alpha_B B + \sum_{i=e, \mu, \tau} \alpha_i L_i, \quad (1)$$

one requires new fermions, also known as *anomalous*, which cancel the anomalies of the new $U(1)_X$ factor, also in combination with the electroweak gauge group. Here, we will discuss a UV completion able to

avoid the strong bounds of Refs. ^{5, 6)} and still be compatible with the measurements in the Higgs decay channels. We finally discuss direct searches at the LHC for such new fermions.

2 Wess-Zumino term and FCNC interactions

Barring the cases of $B/3 - L_i$ and linear combinations thereof, some of the anomalous need to be charged under the electroweak gauge group (henceforth indicated more precisely as electroweak anomalous). We usually assume such new fermions to be heavier than the electroweak scale, due to the fact they have not been observed at colliders so far. Consequently, their effects on the physics of the light vector boson associated with the $U(1)_X$ gauge symmetry, here denoted as \mathcal{X} , can be described within an effective field theory (EFT) approach. In particular, after integrating out the new heavy fermions at one loop, one generates dimension-4 Wess-Zumino (WZ) terms, schematically of the form $\mathcal{X}(W\partial W + WWW)$ and $\mathcal{X}B\partial B$ (with W and B denoting $SU(2)_L$ and $U(1)_Y$ gauge bosons). These contact interactions match, in the EFT without electroweak anomalous, the chiral anomaly coming from the UV fermions we are integrating out from the theory (see e.g. ^{7, 8, 9, 10)}).

Upon integrating out the electroweak anomalous at one loop one finds in the EFT given by the SM and the light vector \mathcal{X}

$$\begin{aligned} \mathcal{L}_{\text{EFT}}^{U(1)_X} \supset & g_X g^2 \frac{C_{BB}}{24\pi^2} \epsilon^{\alpha\mu\nu\beta} \mathcal{X}_\alpha B_\mu \partial_\beta B_\nu + g_X g^2 \frac{C_{ab}}{24\pi^2} \epsilon^{\alpha\mu\nu\beta} \mathcal{X}_\alpha W_\mu^a \partial_\beta W_\nu^b \\ & + g_X g g' \frac{C_{aB}}{24\pi^2} \epsilon^{\alpha\mu\nu\beta} \mathcal{X}_\alpha W_\mu^a \partial_\beta B_\nu + g_X g g' \frac{C_{Ba}}{24\pi^2} \epsilon^{\alpha\mu\nu\beta} \mathcal{X}_\alpha B_\mu \partial_\beta W_\nu^a \end{aligned} \quad (2)$$

where $a, b = 1, 2, 3$ and we neglected non-abelian W terms scaling with an extra gauge coupling g .

As it was emphasized more recently in Refs. ^{5, 6)}, WZ terms display an axion-like behavior (as can be understood by applying the equivalence theorem to the longitudinal component of \mathcal{X}) and lead to amplitudes that grow with the energy. The anomalous $\mathcal{X}W\partial W$ vertex can be dressed with SM flavor-violating interactions leading to loop-induced flavour changing neutral current (FCNC) processes, while the anomalous $\mathcal{X}B\partial B$ vertex is responsible for $Z \rightarrow \gamma\mathcal{X}$ decays at the tree level (see also ^{11, 12, 13, 14)}). For instance, upon integrating out the W boson, the $\mathcal{X}WW$ operator in Eq. (2) yields the effective interaction

$$g_{\mathcal{X}d_i d_j} \bar{d}_j \gamma^\mu P_L d_i X_\mu + \text{h.c.}, \quad (3)$$

where $g_{\mathcal{X}d_i d_j}$ is the effective coupling. In both cases these processes are enhanced as $(\text{energy}/m_{\mathcal{X}})^2$, thus leading to the typically most stringent bounds on light vectors with no direct couplings to electrons, as e.g. in the case of gauged baryon number.

As known (see e.g. ⁶⁾), in the limit where the anomalous pick up their mass from a SM-preserving vacuum expectation value (VEV), the low-energy coefficients of the WZ terms are entirely fixed by the requirement of canceling the $SU(2)_L^2 U(1)_X$ and $U(1)_Y^2 U(1)_X$ anomalies of the SM sector. On the other hand, if the anomalous pick up a mass contribution from the electroweak VEV then the coefficients of the WZ terms become model-dependent. In particular, in the limit of mostly chiral anomalous, the anomalous couplings of the longitudinal component of \mathcal{X} with SM electroweak gauge bosons goes to zero, thus relaxing the strong bounds of Refs. ^{5, 6)} on light vectors.

3 UV model

The field content of the model is displayed in 1, with the anomalon fields highlighted in color¹, and we also extended the scalar sector of the SM in order to spontaneously break the $U(1)_X$ symmetry. By adding a proper term in the scalar potential, $\Delta V(H, \mathcal{S})$, the following VEV configurations are generated

$$\langle H \rangle = \frac{1}{\sqrt{2}} \begin{pmatrix} 0 \\ v \end{pmatrix}, \quad \langle \mathcal{S} \rangle = \frac{v_X}{\sqrt{2}}, \quad (4)$$

with $v \simeq 246$ GeV and v_X being the order parameter of $U(1)_X$ breaking.

We have also included N copies of chiral SM-singlet fermions ν_R^α ($\alpha = 1, \dots, N$) which allow to have more freedom for the cancellation of $U(1)_X$ and $U(1)_X^3$ anomalies (as well as provide a seesaw setup for neutrino masses), but whose presence does not impact the calculation of the electroweak WZ terms.

Field	Lorentz	$SU(3)_C$	$SU(2)_L$	$U(1)_Y$	$U(1)_X$
q_L^i	$(\frac{1}{2}, 0)$	3	2	1/6	$\alpha_B/3$
u_R^i	$(0, \frac{1}{2})$	3	1	2/3	$\alpha_B/3$
d_R^i	$(0, \frac{1}{2})$	3	1	-1/3	$\alpha_B/3$
ℓ_L^i	$(\frac{1}{2}, 0)$	1	2	-1/2	α_i
e_R^i	$(0, \frac{1}{2})$	1	1	-1	α_i
H	$(0, 0)$	1	2	1/2	0
\mathcal{L}_L	$(\frac{1}{2}, 0)$	1	2	$\mathcal{Y} - 1/2$	$X_{\mathcal{L}_L}$
\mathcal{L}_R	$(0, \frac{1}{2})$	1	2	$\mathcal{Y} - 1/2$	$X_{\mathcal{L}_R} + 3\alpha_{B+L}$
\mathcal{E}_L	$(\frac{1}{2}, 0)$	1	1	$\mathcal{Y} - 1$	$X_{\mathcal{L}_L} + 3\alpha_{B+L}$
\mathcal{E}_R	$(0, \frac{1}{2})$	1	1	$\mathcal{Y} - 1$	$X_{\mathcal{L}_L}$
\mathcal{N}_L	$(\frac{1}{2}, 0)$	1	1	\mathcal{Y}	$X_{\mathcal{L}_L} + 3\alpha_{B+L}$
\mathcal{N}_R	$(0, \frac{1}{2})$	1	1	\mathcal{Y}	$X_{\mathcal{L}_R}$
ν_R^α	$(0, \frac{1}{2})$	1	1	0	$X_{\nu_R^\alpha}$
\mathcal{S}	$(0, 0)$	1	1	0	$X_{\mathcal{S}}$

Table 1: Anomaly-free field content of our model. Here $\alpha_{B+L} \equiv \alpha_B + (\alpha_e + \alpha_\mu + \alpha_\tau)/3$. The parameters \mathcal{Y} and $X_{\mathcal{L}}$ are not fixed by the anomaly cancellation requirement.

By construction, the electroweak anomalons pick up their mass from the VEV of H , through the Yukawa Lagrangian

$$-\mathcal{L}_Y = y_1 \bar{\mathcal{L}}_L \mathcal{E}_R H + y_2 \bar{\mathcal{L}}_R \mathcal{E}_L H + y_3 \bar{\mathcal{L}}_L \mathcal{N}_R \tilde{H} + y_4 \bar{\mathcal{L}}_R \mathcal{N}_L \tilde{H} + \text{h.c.}, \quad (5)$$

with $\tilde{H} = i\sigma_2 H^*$. Extra Yukawas of the type²

$$-\Delta \mathcal{L}_Y = y_{\mathcal{L}} \bar{\mathcal{L}}_L \mathcal{L}_R \mathcal{S}^* + y_{\mathcal{E}} \bar{\mathcal{E}}_L \mathcal{E}_R \mathcal{S} + y_{\mathcal{N}} \bar{\mathcal{N}}_L \mathcal{N}_R \mathcal{S} + \text{h.c.}, \quad (6)$$

are excluded for $X_{\mathcal{S}} \neq X_{\mathcal{L}_R} - X_{\mathcal{L}_L}$, thus the anomalon masses are completely chiral. Additionally, for specific values of $U(1)_Y$ and $U(1)_X$ charges, the electroweak anomalons can mix with the SM leptons at the renormalizable level.

¹Similar setups for anomaly cancellation were considered e.g. in Refs. [15, 16].

²The case $\mathcal{S} \rightarrow \mathcal{S}^*$ is trivially obtained by replacing $X_{\mathcal{S}} \rightarrow -X_{\mathcal{S}}$.

4 Higgs physics

The new chiral fermions we introduced modify the SM prediction of the Higgs decay rates. In the SM, the $h \rightarrow \gamma\gamma$ and $h \rightarrow \gamma Z$ amplitudes are dominated by the loop of the W gauge boson interfering negatively with the loop of the top quark and they amount to $\mathcal{A}_{\gamma\gamma}^{\text{SM}} \approx -6.5$ and $\mathcal{A}_{\gamma Z}^{\text{SM}} \approx 5.7$ at leading order. In the presence of a single Higgs doublet, the new physics contribution yields $\mathcal{A}_{\gamma\gamma}^{\text{NP}} \approx \frac{8}{3}(1 - 2\mathcal{Y} + 2\mathcal{Y}^2)$. Writing the modified Higgs width to photons as

$$R_{\gamma\gamma} = \frac{|\mathcal{A}_{\gamma\gamma}^{\text{SM}} + \mathcal{A}_{\gamma\gamma}^{\text{NP}}|^2}{|\mathcal{A}_{\gamma\gamma}^{\text{SM}}|^2}, \quad (7)$$

a recent ATLAS analysis found $R_{\gamma\gamma} = 1.00 \pm 0.12$ ¹⁷⁾. A possibility to have a SM-like prediction is that the new physics contribution interferes negatively with the SM amplitude, namely $\mathcal{A}_{\gamma\gamma}^{\text{NP}} \approx -2\mathcal{A}_{\gamma\gamma}^{\text{SM}} \approx 13.0$. This is obtained either for $\mathcal{Y} \approx 2$ ($1.93 \lesssim \mathcal{Y} \lesssim 2.03$ [2σ range]) or $\mathcal{Y} \approx -1$ ($-1.03 \lesssim \mathcal{Y} \lesssim -0.93$ [2σ range]), both yielding $\mathcal{A}_{\gamma\gamma}^{\text{NP}}(\mathcal{Y} = 2) = \mathcal{A}_{\gamma\gamma}^{\text{NP}}(\mathcal{Y} = -1) \approx 13.3$. Then, for such values of \mathcal{Y} , a correlated shift in the γZ channel $\mathcal{A}_{\gamma Z}^{\text{NP}} \approx -\frac{2}{3}c_W[1 - (3 - 8\mathcal{Y} + 8\mathcal{Y}^2)t_W^2]$ leads to a large deviation from the SM prediction. At the moment, the γZ decay channel of the Higgs has not been observed yet and HL-LHC is expected to measure $\kappa_{\gamma Z}$ within 10% precision¹⁸⁾ and hence test the consistency of our model.

5 Anomalon direct searches

Direct searches at high-energy particle colliders depend on whether the exotic leptons mix with the SM leptons. We discuss the two possible different scenarios corresponding to $\mathcal{Y} \approx 2, -1$, but $\mathcal{Y} \neq 2, -1$, (stable charged leptons) and $\mathcal{Y} = 2, -1$ (unstable charged leptons).

5.1 Stable charged leptons

For $\mathcal{Y} \approx 2, -1$, but $\mathcal{Y} \neq 2, -1$, the exotic leptons do not mix the SM ones and the lightest state of the spectrum is electrically charged and stable due to exotic lepton number. Charged relics are cosmologically dangerous and largely excluded. To avoid cosmological problems one has to invoke low-scale inflation, such that charged relics are either diluted by inflation or never thermally produced. On the other hand, stable charged particles yield striking signatures at colliders in the form of charged track, anomalous energy loss in calorimeters, longer times of flight, etc. Applying the experimental limits of¹⁹⁾ at 13 TeV LHC with the leading-order Drell-Yann cross-sections rescaled for $|Q| = 2$ (see also²⁰⁾), Ref.²¹⁾ obtained $m_{\mathcal{N}, \mathcal{E}} \gtrsim 800$ GeV. Since $m_{\mathcal{N}, \mathcal{E}} = y_{\mathcal{N}, \mathcal{E}} v / \sqrt{2}$, direct searches imply Yukawa couplings, $y_{\mathcal{N}, \mathcal{E}} \approx 4.6$, at the boundary of perturbative unitarity (see e.g.^{22, 23)}).

5.2 Unstable charged leptons

For $\mathcal{Y} = 2, -1$ the electroweak anomalous have electric charge $Q = 2, -1$ (\mathcal{N} components) and $Q = 1, -2$ (\mathcal{E} components). The $|Q| = 2$ states can decay into a W and a $|Q| = 1$ fermion, while the latter can mix with SM leptons through the operators shown in Table 2 and decay into $Z\ell$ or $h\ell$. Signatures of this type were previously studied in Ref.²⁴⁾, which estimated a mass reach at the LHC 14 up to $m_{\mathcal{N}, \mathcal{E}} \sim 800$ GeV (depending on the integrated luminosity). To our knowledge, however, such an analysis has never been performed by the experimental collaborations. However, the bounds appear to be of the same order of those obtained in the case of stable charged leptons.

Mixing operator	$U(1)_Y$	$U(1)_X$
$\bar{\ell}_L^i (\mathcal{E}_L)^c H$	$\mathcal{Y} = 2$	$X_{\mathcal{L}_L} = -\alpha_i - 3\alpha_{B+L}$
$\bar{\ell}_L^i \mathcal{N}_R H$	$\mathcal{Y} = -1$	$X_{\mathcal{L}_L} = \alpha_i$
$\bar{\mathcal{L}}_L e_R^i \tilde{H}$	$\mathcal{Y} = -1$	$X_{\mathcal{L}_L} = \alpha_i$
$\bar{\mathcal{L}}_R (e_R^i)^c H$	$\mathcal{Y} = 2$	$X_{\mathcal{L}_L} = -\alpha_i - 3\alpha_{B+L}$
$\bar{\mathcal{E}}_R (e_R^i)^c \mathcal{S}$	$\mathcal{Y} = 2$	$X_{\mathcal{L}_L} = -\alpha_i + X_S$
$\bar{\mathcal{N}}_L e_R^i \mathcal{S}$	$\mathcal{Y} = -1$	$X_{\mathcal{L}_L} = \alpha_i + X_S - 3\alpha_{B+L}$

Table 2: Renormalizable operators leading to a mixing between electroweak anomalous and SM leptons (first column) and $U(1)_X$ charges (third column) for the phenomenological important case $\mathcal{Y} = 2, -1$. Mixing operators via \mathcal{S}^* are trivially obtained by flipping the sign of X_S in the third column.

6 Conclusion

In this work, we provided a UV completion including electroweak anomalous $\mathcal{L} + \mathcal{E} + \mathcal{N}$ (cf. Table 1) to cancel $U(1)_X$ anomalies in combination with electroweak gauge factors and RH neutrinos to take care of $U(1)_X$ anomalies in isolation when the lepton number generators are gauged. We discussed how to avoid the bound of Refs. ^{5, 6)} by allowing the electroweak anomalous to pick mass only from the SM Higgs and how to simultaneously evade $h \rightarrow \gamma\gamma$ bounds within the UV completion we have chosen. In the model we propose, however, the $h \rightarrow \gamma Z$ channel differs $\mathcal{O}(1)$ from the SM and it will be possible to test this scenario at the HL-LHC. Direct searches of anomalous, whose signatures depend on whether the electroweak anomalous mix or not with the SM leptons, are also very stringent and they practically push the Yukawas of the exotic fermions to the boundary of perturbativity.

Acknowledgments

The work of the author was supported in part by MIUR under contract PRIN 2017L5W2PT.

References

1. L. Di Luzio, M. Nardecchia, and C. Toni, “Light vectors coupled to anomalous currents with harmless Wess-Zumino terms,” *Phys. Rev. D* **105** no. 11, (2022) 115042, [arXiv:2204.05945 \[hep-ph\]](#).
2. R. Foot, “New Physics From Electric Charge Quantization?,” *Mod. Phys. Lett. A* **6** (1991) 527–530.
3. X. G. He, G. C. Joshi, H. Lew, and R. R. Volkas, “New Z-prime Phenomenology,” *Phys. Rev. D* **43** (1991) 22–24.
4. X.-G. He, G. C. Joshi, H. Lew, and R. R. Volkas, “Simplest Z-prime model,” *Phys. Rev. D* **44** (1991) 2118–2132.
5. J. A. Dror, R. Lasenby, and M. Pospelov, “New constraints on light vectors coupled to anomalous currents,” *Phys. Rev. Lett.* **119** no. 14, (2017) 141803, [arXiv:1705.06726 \[hep-ph\]](#).
6. J. A. Dror, R. Lasenby, and M. Pospelov, “Dark forces coupled to nonconserved currents,” *Phys. Rev. D* **96** no. 7, (2017) 075036, [arXiv:1707.01503 \[hep-ph\]](#).

7. E. D'Hoker and E. Farhi, "Decoupling a Fermion Whose Mass Is Generated by a Yukawa Coupling: The General Case," *Nucl. Phys. B* **248** (1984) 59–76.
8. E. D'Hoker and E. Farhi, "Decoupling a Fermion in the Standard Electroweak Theory," *Nucl. Phys. B* **248** (1984) 77.
9. J. Preskill, "Gauge anomalies in an effective field theory," *Annals Phys.* **210** (1991) 323–379.
10. F. Feruglio, A. Masiero, and L. Maiani, "Low-energy effects of heavy chiral fermions," *Nucl. Phys. B* **387** (1992) 523–561.
11. A. Ismail and A. Katz, "Anomalous Z' and diboson resonances at the LHC," *JHEP* **04** (2018) 122, [arXiv:1712.01840 \[hep-ph\]](#).
12. L. Michaels and F. Yu, "Probing new $U(1)$ gauge symmetries via exotic $Z \rightarrow Z'\gamma$ decays," *JHEP* **03** (2021) 120, [arXiv:2010.00021 \[hep-ph\]](#).
13. J. Davighi, "Anomalous Z' bosons for anomalous B decays," *JHEP* **08** (2021) 101, [arXiv:2105.06918 \[hep-ph\]](#).
14. G. D. Kribs, G. Lee, and A. Martin, "Effective Field Theory of Stückelberg Vector Bosons," [arXiv:2204.01755 \[hep-ph\]](#).
15. M. Duerr, P. Fileviez Perez, and M. B. Wise, "Gauge Theory for Baryon and Lepton Numbers with Leptoquarks," *Phys. Rev. Lett.* **110** (2013) 231801, [arXiv:1304.0576 \[hep-ph\]](#).
16. M. Duerr and P. Fileviez Perez, "Baryonic Dark Matter," *Phys. Lett. B* **732** (2014) 101–104, [arXiv:1309.3970 \[hep-ph\]](#).
17. **ATLAS** Collaboration, G. Aad *et al.*, "Combined measurements of Higgs boson production and decay using up to 80 fb^{-1} of proton-proton collision data at $\sqrt{s} = 13 \text{ TeV}$ collected with the ATLAS experiment," *Phys. Rev. D* **101** no. 1, (2020) 012002, [arXiv:1909.02845 \[hep-ex\]](#).
18. M. Cepeda *et al.*, "Report from Working Group 2: Higgs Physics at the HL-LHC and HE-LHC," *CERN Yellow Rep. Monogr.* **7** (2019) 221–584, [arXiv:1902.00134 \[hep-ph\]](#).
19. **CMS** Collaboration, V. Khachatryan *et al.*, "Search for long-lived charged particles in proton-proton collisions at $\sqrt{s} = 13 \text{ TeV}$," *Phys. Rev. D* **94** no. 11, (2016) 112004, [arXiv:1609.08382 \[hep-ex\]](#).
20. L. Di Luzio, R. Gröber, J. F. Kamenik, and M. Nardecchia, "Accidental matter at the LHC," *JHEP* **07** (2015) 074, [arXiv:1504.00359 \[hep-ph\]](#).
21. Q. Bonnefoy, L. Di Luzio, C. Grojean, A. Paul, and A. N. Rossia, "The anomalous case of axion EFTs and massive chiral gauge fields," *JHEP* **07** (2021) 189, [arXiv:2011.10025 \[hep-ph\]](#).
22. L. Di Luzio, J. F. Kamenik, and M. Nardecchia, "Implications of perturbative unitarity for scalar di-boson resonance searches at LHC," *Eur. Phys. J. C* **77** no. 1, (2017) 30, [arXiv:1604.05746 \[hep-ph\]](#).
23. L. Allwicher, P. Arnan, D. Barducci, and M. Nardecchia, "Perturbative unitarity constraints on generic Yukawa interactions," *JHEP* **10** (2021) 129, [arXiv:2108.00013 \[hep-ph\]](#).

24. T. Ma, B. Zhang, and G. Cacciapaglia, “Doubly Charged Lepton from an Exotic Doublet at the LHC,” *Phys. Rev. D* **89** no. 9, (2014) 093022, [arXiv:1404.2375 \[hep-ph\]](#).

Neutrino Mixing and Leptogenesis in a $L_e - L_\mu - L_\tau$ model

Simone Marciano

*Dipartimento di Matematica e Fisica, Università di Roma Tre,
Via della Vasca Navale 84, 00146, Roma, Italy
INFN, Sezione di Roma Tre*

Abstract

We present a simple extension of the Standard Model with three right-handed neutrinos in a SUSY framework, with an additional $U(1)_F$ abelian flavor symmetry with a non standard leptonic charge $L_e - L_\mu - L_\tau$ for lepton doublets and arbitrary right-handed charges. The model is able to reproduce the experimental values of the mixing angles of the PMNS matrix and of the $r = \Delta m_{\text{sun}}^2 / \Delta m_{\text{atm}}^2$ ratio, with only a moderate fine tuning of the Lagrangian free parameters. The baryon asymmetry of the Universe is generated via thermal leptogenesis through CP-violating decays of the heavy right-handed neutrinos. We present a detailed numerical solution of the relevant Boltzmann Equations (BE).

1 Introduction

The Standard Model (SM) of particle physics has proven to be one of the most accurate theories to explain microscopic interactions at an unprecedented level. However, it fails to account for relevant low energy data, such as the structure of fermion masses and mixings (in particular, the non-vanishing neutrino masses) and the value of the baryon asymmetry of the Universe (BAU), which is commonly expressed by the parameter η_B . Latest observations ¹⁾ provide a numerical value of $\eta_B \approx 6.1 \cdot 10^{-10}$.

	l_e	l_μ	l_τ	l_e^c	l_μ^c	l_τ^c	F_1	F_2	\bar{F}_1	\bar{F}_2	H_u	H_d	N_1	N_2	N_3
$U(1)_F$	+1	-1	-1	-13	7	3	2	1/2	-2	-1/2	0	0	-1	1	0

Table 1: $U(1)_F$ charges for leptons, Higgses and flavon fields.

In recent times, an enormous experimental progress has been made in our knowledge of the neutrino properties and it has been clearly shown that the lepton mixing matrix contains two large and one small mixing angles, and that the two independent mass-squared differences are both different from zero. A very well motivated possibility to address this problem is given by the $U(1)_F$ flavor symmetry with non-standard leptonic charge $L_e - L_\mu - L_\tau$ for lepton doublets and arbitrary right-handed charges. As it is well known, in the limit of exact symmetry, the neutrino mixing angles are not predicted in the right experimental spots, therefore a symmetry breaking mechanism is needed in order to provide corrections, as we will see in the following. With the present paper we aim to go beyond the existing literature, assessing whether see-saw models based on the $L_e - L_\mu - L_\tau$ quantum number can simultaneously account for neutrino masses and mixing and explain the BAU through thermal leptogenesis.

2 The Model

We summarize the relevant features of our see-saw flavor model based on a broken $U(1)_F$ symmetry. In the proposed scenario, the left handed lepton doublets have charge $L_e - L_\mu - L_\tau$ under the $U(1)_F$, while the right-handed $SU(2)$ singlets $l_{e,\mu,\tau}^c$ have the charges reported in Tab.1. Assuming a SUSY framework, two Higgs doublet fields, H_u and H_d , are considered. Also, the spectrum of the theory contains three heavy sterile neutrinos $N_{i=1,2,3}$, needed for the generation of the light neutrino masses as well as for the implementation of the leptogenesis process. The flavor symmetry is broken by vacuum expectation values (vevs) of $SU(2)$ singlet scalar fields (flavons) suitably charged under the $U(1)_F$ symmetry. Non-vanishing vevs are determined by the D-term potential:

$$V_D = \frac{1}{2}(M_{F1}^2 - g_F|F_1|^2 - g_F|F_2|^2 - g_F|\bar{F}_1|^2 - g_F|\bar{F}_2|^2), \quad (1)$$

where g_F denotes the gauge coupling constant of the $U(1)_F$ symmetry while M_{F1} is the Fayet-Iliopoulos term. Non-zero vevs are obtained by imposing the SUSY minimum $V_D = 0$. Without loss of generality, we can assume equal vevs for the flavons and define $\lambda = \langle F_1 \rangle / M_F = \langle F_2 \rangle / M_F = \langle \bar{F}_1 \rangle / M_F = \langle \bar{F}_2 \rangle / M_F$ the common ratio between the vevs of the flavons and the scale M_F at which the flavour symmetry is broken.

2.1 Charged lepton sector

After flavor and electroweak symmetry breakings, including higher dimensional operators proportional to power of λ , the charged lepton mass matrix, factoring out the τ mass, assumes the following

form:

$$m_l \sim m_\tau \begin{pmatrix} a_{11}\lambda^5 & a_{12}\lambda^3 & a_{13}\lambda \\ a_{21}\lambda^6 & a_{22}\lambda^2 e^{i\phi_{22}} & a_{23}e^{i\phi_{23}} \\ a_{31}\lambda^6 & a_{32}\lambda^2 e^{i\phi_{32}} & 1 \end{pmatrix}. \quad (2)$$

For $\lambda < 1$, the following mass ratios $m_e : m_\mu : m_\tau = \lambda^5 : \lambda^2 : 1$ is found, which naturally reproduces the observed pattern if $\lambda \sim 0.22$.

2.2 Neutrino sector

In the neutrino sector, masses are generated through the standard type-I see-saw mechanism: $m_\nu \simeq -v_u^2 Y^T M_R^{-1} Y$, where Y and M_R are respectively the Yukawa matrix and the Majorana mass matrix. After the symmetry breaking and at the price of some fine tuning, they can be written as:

$$Y = \frac{m_D}{v_u} \sim \begin{pmatrix} \lambda^2 d_{11} & a e^{i\Sigma} & b e^{i\Omega} \\ c e^{i\Phi} & \lambda^2 d_{22} & \lambda^2 d_{23} e^{i\Theta} \\ \lambda^2 d_{31} & \lambda^2 d_{32} & \lambda^2 d_{33} \end{pmatrix}, \quad M_R \sim \mathcal{M} \begin{pmatrix} \lambda^2 m_{11} & W & \lambda^2 m_{13} \\ W & \lambda^2 m_{22} & \lambda^2 m_{23} \\ \lambda^2 m_{13} & \lambda^2 m_{23} & Z \end{pmatrix}, \quad (3)$$

where \mathcal{M} is the sterile neutrinos overall mass scale and (W, Z, m_{ij}, d_{ij}) can be regarded as free parameters. Notice that the Dirac mass matrix contains un-suppressed entries because of the choice $Q_{N_1} = -Q_{N_2}$ for two of the right-handed neutrinos. The four physical phases $\Sigma, \Omega, \Phi, \Theta$ in Y , obtained after a suitable redefinition of the fermion fields, are the only source of CP violation of our model and are not fixed by the symmetries of the Lagrangians. For the sake of simplicity and without any loss of generality, we can assume the parameters $m_{ij} \sim m$ and consider m as a real quantity. In general, from the type-I seesaw master formula follows that the mass scale of the sterile neutrinos must be set around 10^{15} GeV, so that the light neutrino masses are below the experimental upper bounds. In our case, this means that there are three very massive sterile neutrinos with masses close by 10^{15} GeV. We dub this scenario as the *resonant scenario*. On the other hand, one could lower the overall mass scale to 10^{13} GeV. In such a case, in order to maintain a good agreement with the low energy phenomenology¹ we must assume a hierarchy among the parameters in the Majorana mass matrix: $W/Z \sim 10^2$. This leads to a splitting of the sterile neutrino masses, in other words we end up with one lighter state at $M_3 \sim 10^{13}$ GeV and two heavier states with $M_{1,2} \sim 10^{15}$ GeV. From now on we refer to this scenario as the *hierarchical scenario*.

Also, it can be proved that, in both cases, it is possible to recast the m_ν obtained from the type-I seesaw master formula in this simple form:

$$m_\nu = m_0 \begin{pmatrix} \lambda^2 x_1 & 1 & x \\ 1 & x_2 \lambda^2 & x_3 \lambda^2 \\ x & x_3 \lambda^2 & x_4 \lambda^2 \end{pmatrix}, \quad (4)$$

where m_0 is the overall mass scale and (x, x_i) are suitable combinations of the coefficients present in Dirac and Majorana matrices in eq.(3). Computing U_ν and U_l , which are the neutrino mixing

¹The complete discussion can be found in ²).

matrix and the charged lepton mixing matrix respectively, we can obtain the final expression of the neutrino mixing angles, using $U_{PMNS} = U_l^\dagger U_\nu$. These, as well as the mass ratio $r = \Delta m_{sol}^2 / \Delta m_{atm}^2$, are in good agreement with the results given in ³⁾. This conclusion has been further strengthened by a successful numerical scan ⁴⁾ over the model free parameters, with moduli extracted flat in the intervals $[0.2, 5]$ and all the phases in $[-\pi, \pi]$.

3 Leptogenesis

As stated above, our study of leptogenesis will be performed within two reference scenarios, identified by different mass patterns for the heavy right-handed neutrinos: the *resonant* and *hierarchical* scenarios. The three Majorana neutrinos decay in the early Universe creating a lepton asymmetry, which is consequently converted in a baryon asymmetry through non perturbative processes, known as *sphaleron processes*. As we will clarify in the following, a different Majorana neutrino mass spectrum can lead to different CP-violating parameters, affecting the final amount of baryon asymmetry in the Universe.

3.1 Resonant Scenario

The first scenario we consider is the *resonant scenario*, with three degenerate sterile neutrinos with mass $M \sim 10^{15}$ GeV. Being mass degenerate, we expect that all the three right-handed neutrinos contribute to the leptogenesis process. The resonant regime is characterised by the presence of an enhancement of the CP-violation; this is a very powerful tool because it allows producing the right amount of BAU even if the sterile neutrinos are much lighter than 10^{10} GeV. However in our case this is a problem since the masses of the Majorana neutrinos are very high, close by the GUT scale; this would lead to an excess of the BAU. In other words, in order to obtain a value of the baryon-asymmetry comparable to the one observed so far, we need to impose a fine tuning on the CP-violating phases in the Majorana mass matrix.

The full BE² in this scenario are:

$$\begin{aligned} \frac{dN_i}{dz} &= -(D_i + S_i)(N_i - N_i^{\text{eq}}) \quad i = 1, 2, 3 \\ \frac{dN_{B-L}}{dz} &= \sum_i^3 \varepsilon_i D_i (N_i - N_i^{\text{eq}}) - W_i N_{B-L}, \end{aligned} \tag{5}$$

where N_i stands for number density of the RH sterile neutrinos, while N_{B-L} is the amount of $B-L$ asymmetry, both normalized by comoving volume. D_i and S_i indicate, respectively, inverse decay and scattering contributions to the production of the right-handed neutrinos while the W_i represent the total rate of Wash-out processes including both inverse decay and $\Delta L \neq 0$ scattering contributions. Also, $\varepsilon_i = \varepsilon_i(z)$ are the full time dependent asymmetry parameters as discussed in ²⁾ and in references therein. As shown in fig.(1), the time dependence of the CP-asymmetry

²All the details regarding the Boltzmann Equations can be found in ²⁾ and in references therein.

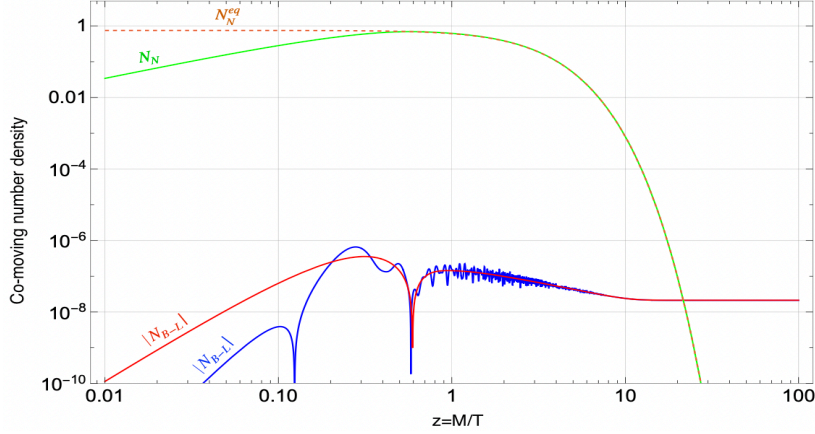


Figure 1: $B-L$ asymmetry and neutrino abundance evolution during the expansion of the Universe. The blue line refers to the full solution of the Boltzmann's equations, obtained retaining the time dependence of the CP -violation parameter. The red line refers to the solution of the analogous system but adopting a time-constant value of the asymmetry parameters. Finally, the green line represents the abundance of the right-handed neutrinos, as given by the solution of the system. For reference, the latter is compared with the function N_N^{eq} (dashed line) which represents a thermal equilibrium abundance for right-handed neutrinos.

parameters does not affect the final amount of baryon-asymmetry. This is because this scenario is characterised by the *strong wash-out regime*, *i.e.* the lepton asymmetry generated during the N_i creation phase is efficiently washed out. After the fine tuning on the CP -violating phases, as discussed above, and keeping all the other parameters to order one, we evaluated the final BAU solving the set of differential equation in eq.(5) obtaining $\eta_B \simeq 3.01 \cdot 10^{-10}$. Notice that the relatively good value for η_B has been obtained for a particular representative choice of the model parameters (also adopted in fig.(1)); we are confident that regions of the parameter space consistent with the correct baryon asymmetry exist in our model.

3.2 Hierarchical scenario

This alternative scenario is obtained by lowering the mass scale \mathcal{M} down to a value of the order of 10^{13} GeV, which brings to a hierarchical mass spectrum for the sterile neutrinos, with two heavy, almost degenerate, states with $M_1 \simeq M_2 \sim 10^{15}$ GeV, and a lighter one with $M_3 \simeq 10^{13}$ GeV. In this set-up, the relevant BE present the same structure as in the previous case with the substantial difference that now only the out-of-equilibrium decay of the lightest heavy neutrino generates the BAU via thermal leptogenesis, and the CP -asymmetry parameter ε is no longer time dependent, but it is constant and essentially it depends on the mass splitting M_3/M_i , with $i = 1, 2$. The numerical solution of the BE is shown in fig.(2). The result is $\eta_B = 3.96 \cdot 10^{-10}$. It is interesting

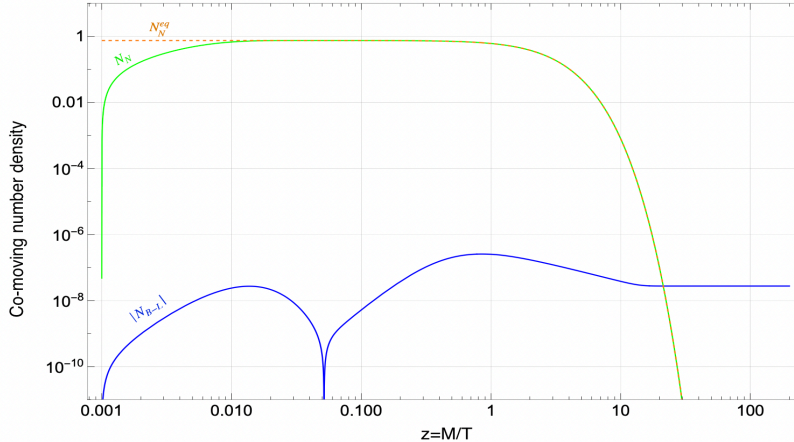


Figure 2: *Evolution of the $B - L$ asymmetry in the hierarchical scenario. The color code is the same as in fig.1.*

to notice that, contrary to the resonant regime, in the hierarchical scenario it is possible to find a parameter assignation leading to viable leptogenesis without imposing a fine tuning on the CP violating phases.

4 Conclusion

In this paper we have provided a proof of existence about the possibility of contemporary achieving viable masses and mixing patterns for the SM neutrinos and a value of the BAU, via leptogenesis, compatible with the experimental determination, in models based on the abelian flavor symmetry $L_e - L_\mu - L_\tau$. We have identified two reference scenarios and we have showed how it is possible to obtain the right amount of BAU in both of them.

5 Acknowledgements

The author would like to thank the organizers for the opportunity to have a talk. Many thanks also to D. Meloni and G. Arcadi for the useful discussions.

References

1. Aghanim, N. and others, *Astron. Astrophys.* **641**, A6 (2020).
2. G. Arcadi, S. Marciano and D. Meloni, [arXiv:2205.02565 [hep-ph]].
3. Esteban, Ivan *et al.* *JHEP* **2020**, 9 (2020).
4. Marciano, Simone, *J. Phys. Conf. Ser.* **2156**, 012188 (2021).

PROBING DARK ABELIAN GAUGE SECTOR AT THE INTENSITY FRONTIER

Gabriel Massoni Salla

Instituto de Física, Universidade de São Paulo, C.P. 66.318, 05315-970 São Paulo, Brazil

Abstract

In this study we explore the phenomenology of an UV complete dark photon model, in which we explicitly consider a new scalar sector responsible for the mass generation. In this context, we compute the present and future sensitivity regions for KOTO, LHCb and Belle II by considering meson decays to 4-lepton final states. We find that these experiments have large sensitivity to this model and that, under some circumstances, the connection between the dark photon and the scalar sector can completely change the low-energy phenomenology of both.

1 Introduction

Models containing new vector fields associated to new gauge symmetries are among the best motivated extensions of the Standard Model (SM). In particular, a large class of beyond the SM (BSM) models predict the existence of a new $U(1)_D$ gauge symmetry with a massive gauge boson at low-energies (see Ref. ¹⁾ for a recent review). In most studies it is assumed that this vector field has a Stückelberg mass, thus making the model incomplete and possibly ill-defined in the UV. This owns to the lack of a mass generation mechanism for the new gauge boson and the presence of potentially non-vanishing operators that induce a bad high-energy behaviour ²⁾. In the present study, instead, we consider an UV complete scenario, in which the simplest mass generation mechanism is responsible for the mass of the new gauge boson ³⁾. We then predict how the standard phenomenology of the model with a Stückelberg mass is modified in this new context by analysing meson decay signatures at KOTO ⁴⁾, LHCb ⁵⁾ and Belle II ⁶⁾ experiments. For a complete discussion and more details on the analysis, we refer the reader to Ref. ⁷⁾.

2 UV complete Dark Photon model

Our starting point is the most general renormalizable Lagrangian for a massless gauge boson Z_D , named here dark photon

$$\mathcal{L}_{\text{vector}} = -\frac{1}{4}Z_{D\mu\nu}Z_D^{\mu\nu} + \frac{\epsilon}{2}Z_D^{\mu\nu}B_{\mu\nu}, \quad (1)$$

with ϵ the kinetic mixing parameter¹. Notice that we consider all SM particles to be neutral under the new symmetry group. The mass generation proceeds via a dark Higgs mechanism, in which a new scalar field S , the dark Higgs, spontaneously breaks $U(1)_D$. The Lagrangian for the scalar sector reads

$$\mathcal{L}_{\text{scalar}} = |D_\mu H|^2 + |D_\mu S|^2 - V(H, S), \quad (2)$$

with H the SM-like Higgs boson and

$$V(H, S) = m_H^2|H|^2 + \lambda|H|^4 + m_S^2|S|^2 + \lambda_S|S|^4 + \kappa|H|^2|S|^2. \quad (3)$$

The dark Higgs is supposed to be a SM-singlet, such that $D_\mu S = \partial_\mu S + ig_D Z_{D\mu} S$, with g_D the $U(1)_D$ gauge coupling. After both scalars pick up a vacuum expectation value (vev), we have four effects:

- The kinetic mixing term in Eq. (1), after diagonalization of kinetic and mass terms, generates a coupling between the dark photon Z_D and the electromagnetic current suppressed by a factor ϵ . This result holds as long as $\epsilon \ll 1$ and $m_{Z_D} \ll v$, v being the electroweak vev, which is precisely the region of interest;
- The quartic term $\kappa|H|^2|S|^2$ induces a mass mixing between both scalars. Up to first order in the couplings, the physical mixing angle is given by

$$s_h \simeq \frac{\kappa v_S v}{m_s^2 - m_h^2}, \quad (4)$$

where v_S is the vev of S and $m_{h,s}$ are the masses of the physical scalars h, s after the diagonalization. As a direct consequence of this mixing, the dark Higgs s inherits all interactions of the SM-like Higgs, suppressed, however, by a power of s_h ;

- The kinetic term of the dark Higgs produces a mass term for the dark photon, namely $m_{Z_D} = g_D v_S$;
- In addition to the dark photon mass, the kinetic term $|D_\mu S|^2$ contains an interaction between the dark particles given by

$$|D_\mu S|^2 \supset g_D m_{Z_D} s Z_{D\mu} Z_D^\mu. \quad (5)$$

The interactions of the Z_D field with the electromagnetic current and the scalar mixing are precisely what characterises the usual dark photon and dark Higgs phenomenology, respectively^{1, 9)}. The $U(1)_D$ gauge connection in Eq. (5) brings together both scalar and vector sectors and can thus give rise to novel phenomenological signatures. If we take $g_D \rightarrow 0$ while maintaining m_{Z_D} constant, we decouple both sectors and recover the usual phenomenology for both models. Hence, in order to study the effects of the dark gauge connection (5), we need to assume that its strength is at least comparable to the other interactions².

¹A tiny kinetic mixing ranging in $10^{-2} < \epsilon < 10^{-13}$ can be obtained through multi-loop processes in theories where the tree-level is forbidden in the UV⁸⁾.

²Here we neglect the decays of S to a photon and a dark photon that take place via the kinetic mixing, as the width is further suppressed by ϵ^2 .

One of the main features of Eq. (5) is to give a contribution to the dark Higgs decay width that is independent of s_h^2 . The partial width $\Gamma(s \rightarrow Z_D Z_D)$ is proportional to g_D^2 and is parametrically larger than the decay rates inherited from the SM-like Higgs that scale with s_h^2 . More precisely, the branching ratio to a pair of dark photons will be approximately 1 if $g_D \gg 7 \cdot 10^{-3} s_h$ is satisfied. While most dark Higgs searches rely on the dark Higgs decaying to pairs of fermions⁹⁾, the scenario in which this hierarchy is respected allow us to probe directly the gauge structure of the $U(1)_D$ group. For this reason we focus our phenomenological analysis on the channel $s \rightarrow Z_D Z_D$.

3 Phenomenology

In order to probe the decay $s \rightarrow Z_D Z_D$ in a real experiment, we must first produce the dark Higgs. This can be achieved through the scalar mixing, in which a SM particle, in our case a meson, decays to s plus other SM states³. The corresponding branching ratio will turn out to be small considering that s_h is expected to be small. To compensate for this, we can profit from experiments at the high intensity frontier, *i.e.* experiments that will take large amounts of data and perform very precise measurements. In particular, the KOTO, LHCb and Belle II experiments aim to probe, respectively, extremely rare kaons, B -mesons and Υ 's decays with increasing luminosity in the years to come.

3.1 Visible signatures - LHCb and Belle II

In LHCb and Belle II we consider $B^\pm \rightarrow K + s$, with K a kaon state, and $\Upsilon(1S, 2S, 3S) \rightarrow \gamma + s$ respectively^{9, 11)}. The number of events expected in these experiments is given by the formula

$$N_{\text{evt}} = N_M \text{BR}(M \rightarrow s + M') \text{BR}(s \rightarrow Z_D Z_D) P_{\text{dec}}^{\text{in}} f_{\text{geom}} \text{BR}(Z_D \rightarrow \ell^- \ell^+)^2 \varepsilon, \quad (6)$$

where $M (M') = B^\pm (K)$ or $\Upsilon (\gamma)$, N_M is the total number of mesons produced, $P_{\text{dec}}^{\text{in}}$ is the probability of the dark photons to decay inside the experimental volume⁴, f_{geom} is the geometrical acceptance and ε is the particle detection efficiency. In the equation above we take both dark photons to be decaying into a pair of charged leptons, which implies that the experimental signature involves a 4-lepton final state. Since we demand all final states to be observed within the detector, the signature given by Eq. (6) is denoted as *visible*.

In both LHCb and Belle II cases we might have background coming from the SM. Since the SM backgrounds decay promptly, we can rely on the long-lived nature of the dark particles and require the signal to be displaced, in other words, demand that the dark particles are enough long-lived such that they decay some distance away from the initial vertex. In this manner one can univocally disentangle the signal from the background. The definition of a displaced signal depends on the spatial resolution of the vertex detector of each experiment. For LHCb we use 0.82 cm, while for Belle II we use 3.8 cm. The situation is more complicated if the dark particles decay promptly, but background can still be avoided if either the decay rate of the model is expected to be much larger than the SM one (approximately for $s_h > 10^{-3}$ in the case of LHCb and $s_h > 10^{-2}$ for Belle II), or by searching for resonances in di-lepton invariant masses, which are characteristic of the decay chain $s \rightarrow Z_D Z_D \rightarrow 4\ell$.

³Measurements of the Higgs coupling strength imposes that $s_h < 0.1$ 10).

⁴We consider throughout our analysis that $g_D > 10^{-3}$. For such values the dark Higgs decays promptly in all experiments considered, that is, with decay length less than the corresponding spatial resolution. Whence, all decay probabilities refer to the dark photons only.

To compute the number of events in Eq. (6) we simulated the initial meson flux with `Pythia8`¹²⁾ and computed the decay probability with `MadDump`¹³⁾, using the UFO model of Ref. 3). For LHCb we use that the angular acceptance is $2 < \eta < 5$ and that the maximum baseline of the detector is 20 m. Moreover, we use the combined luminosities of Run 1 and 2 of 9 fb^{-1} , meaning that about 10^{11} B 's were produced. For Belle II we consider the detector to be a cylinder of radius of 3.48 m and length 7.38 m, while the angular acceptance is given by $17^\circ < \theta < 150^\circ$ with respect to the dislocated collision point. We assume here that Belle II will produce approximately 40 times more Υ 's than Belle, which is equivalent to $4 \times 10^9 \Upsilon(1S)$, $6.3 \times 10^9 \Upsilon(2S)$ and $4.8 \times 10^8 \Upsilon(3S)$ events.

In Fig. 1 we show the sensitivity regions in the dark photon and dark Higgs parameter spaces corresponding to $N_{\text{evts}} \geq 3$. We see in general that the regions we obtain in our case are significantly different from the ones obtained considering either only the dark photon or only the dark Higgs, meaning that the dark gauge coupling can indeed affect the phenomenology of both particles. In the left panel of Fig. 1, the lines crossing the regions denote when the dark photons have a particular decay length, which are then used to define whether a signal is displaced or not. Also, we end up being sensitive to much smaller values of ϵ due to the fact that in Eq. (6) the total number of dark photons produced does not depend on the kinetic-mixing, thus de-correlating production and detection.

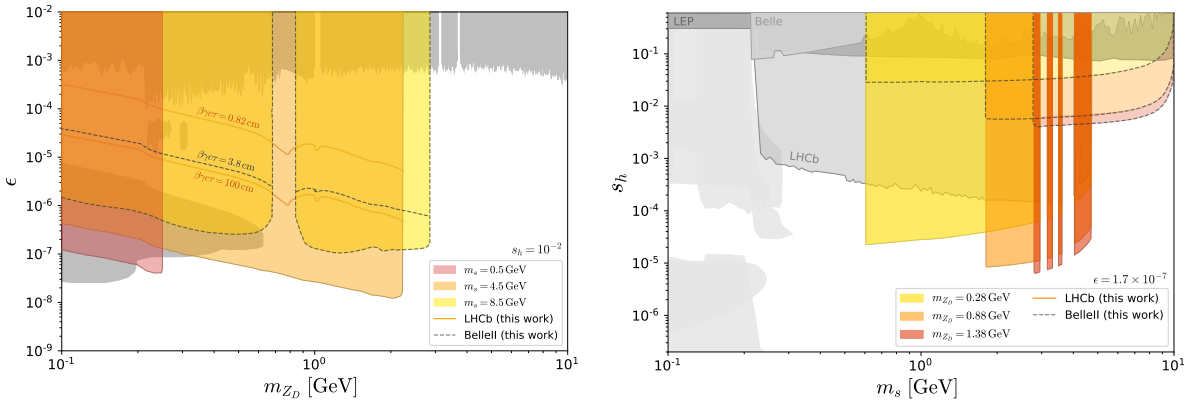


Figure 1: *Left)* Expected sensitivity in the $m_{D} \times \epsilon$ parameter space for the LHCb (solid) and Belle II (dashed) searches. We fix $s_h = 10^{-2}$. The solid orange (dashed black) line crossing LHCb (Belle II) bounds indicate where the dark photon decay length reaches 0.82 cm (3.8 cm), which is the spatial resolution of the detector's vertex locator. We also indicate $\beta\gamma c\tau = 100 \text{ cm}$ for LHCb, corresponding to when dark photons start to exit the vertex detector. *Right)* Expected bounds in the $m_s \times s_h$ plane for the LHCb search (solid) and the future sensitivity projection for the Belle II search (dashed). We fixed the kinetic mixing parameter to $\epsilon = 1.7 \times 10^{-7}$. The vetoed regions represent the meson resonances that we have considered as irreducible backgrounds. In both plots the gray regions denote limits from searches for dark photons and dark Higgs in the limit they are decoupled.

3.2 Invisible signatures - KOTO

The situation in KOTO is very different from LHCb and Belle II. The main goal of the collaboration is to measure the CP-violating decay $K_L \rightarrow \pi^0 \nu \bar{\nu}$. Latest measurements can set an upper bound on the respective branching ratio, given by $\text{BR}(K_L \rightarrow \pi^0 X) < 3.7 \cdot 10^{-9}$ for X invisible¹⁴⁾. Note that X in this case must be necessarily invisible to the detector, so to mimic the neutrinos in the SM decay. Therefore, the bound from KOTO can be translated to a bound on the model parameter space if the dark photons

decay outside the detector, which can be quantified by the effective branching ratio

$$\text{BR}_{\text{eff}} \equiv \text{BR}(K_L \rightarrow \pi^0 s) \text{BR}(s \rightarrow Z_D Z_D) P_{\text{dec}}^{\text{out}}, \quad (7)$$

where now $P_{\text{dec}}^{\text{out}}$ is the probability of the dark photons to escape the detector, as opposed to $P_{\text{dec}}^{\text{in}}$ in Eq. (6). The branching ratio for $K_L \rightarrow \pi^0 s$ was taken from Ref. 15).

To estimate the effective branching ratio of Eq. (7) we simulate a K_L flux according to Ref. 16) with approximately $6.4 \cdot 10^{12}$ kaons produced and consider the decay volume used in Refs. 14, 17). Our results are presented in Fig. 2, in which we show the regions in the dark photon (left panel) and dark Higgs (right panel) parameter space that are excluded by demanding that $\text{BR}_{\text{eff}} \leq \text{BR}(K_L \rightarrow \pi^0 X)$. We note that in the $m_s \times s_h$ parameter space we lose sensitivity as the kinetic-mixing grows and saturates as $\epsilon < 10^{-6}$. In the dark photon parameter space we can achieve a much larger sensitivity due to the fact that BR_{eff} depends on ϵ and m_{Z_D} solely through $P_{\text{dec}}^{\text{out}}$. As a consequence, the experiment is sensitive to lower and lower values of kinetic-mixing and mass, as in this region the dark photons are more long-lived and thus escape more often the KOTO detector⁵.

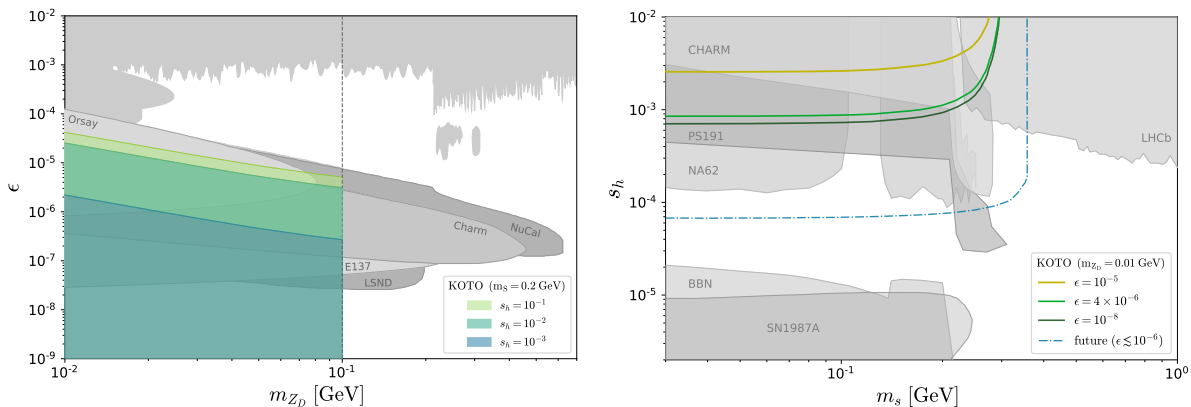


Figure 2: *Left)* Limits from KOTO translated to the dark photon parameter space, where we have fixed $m_s = 0.2$ GeV and colored regions are excluded for $s_h = 10^{-1}$ (green), 10^{-2} (blue) and 10^{-3} (dark blue). The regions extend down to $\epsilon = 0$. *Right)* Current bounds on the dark Higgs parameter space coming from KOTO fixing $m_{Z_D} = 0.01$ GeV. The different solid curves consider $\epsilon = 10^{-5}$ (yellow), 4×10^{-6} (green) and 10^{-8} (dark green). We show in blue dashed-dotted the maximum future sensitivity of the KOTO experiment assuming the SM prediction for $\text{BR}(K_L \rightarrow \pi^0 \nu \bar{\nu})$ can be attained. Gray regions are the same from Fig. 1.

4 Discussion and conclusions

In this work we have addressed the question whether or not the consideration of an explicit mass generation mechanism for the simplest dark photon model can impact its low-energy phenomenology. Indeed, we find that under some assumptions the dark gauge connection can dramatically modify experimental searches for dark photons and dark Higgs. We have seen this explicitly by considering 4-lepton final state decays of K_L , B^\pm and Υ 's at KOTO, LHCb and Belle II. Taking into account present and future data for

⁵Analogously, upper bounds on the SM Higgs invisible width can put bounds on the $m_{Z_D} \times \epsilon$ plane that are similar to those obtained for the KOTO experiment⁷).

these experiments, we see great prospects of probing interesting and very unique regions of the parameter space.

Acknowledgements

The author acknowledges financial support from Fundação de Amparo à Pesquisa de São Paulo (FAPESP) under contract 2020/14713-2 and partial financial support from the school organization to attend the XX LNF Summer School “Bruno Touschek” in Nuclear, Subnuclear and Astroparticle Physics.

References

1. M. Fabbrichesi, E. Gabrielli and G. Lanfranchi, doi:10.1007/978-3-030-62519-1 [arXiv:2005.01515 [hep-ph]].
2. G. D. Kribs, G. Lee and A. Martin, Phys. Rev. D **106**, no.5, 055020 (2022) doi:10.1103/PhysRevD.106.055020 [arXiv:2204.01755 [hep-ph]].
3. D. Curtin, R. Essig, S. Gori and J. Shelton, JHEP **02** (2015), 157 doi:10.1007/JHEP02(2015)157 [arXiv:1412.0018 [hep-ph]].
4. T. Yamanaka [KOTO], PTEP **2012** (2012), 02B006 doi:10.1093/ptep/pts057
5. A. A. Alves, Jr. *et al.* [LHCb], JINST **3** (2008), S08005 doi:10.1088/1748-0221/3/08/S08005
6. T. Abe *et al.* [Belle-II], [arXiv:1011.0352 [physics.ins-det]].
7. A. L. Foguel, G. M. Salla and R. Z. Funchal, [arXiv:2209.03383 [hep-ph]].
8. T. Gherghetta, J. Kersten, K. Olive and M. Pospelov, Phys. Rev. D **100**, no.9, 095001 (2019) doi:10.1103/PhysRevD.100.095001 [arXiv:1909.00696 [hep-ph]].
9. M. W. Winkler, Phys. Rev. D **99** (2019) no.1, 015018 doi:10.1103/PhysRevD.99.015018 [arXiv:1809.01876 [hep-ph]].
10. R. L. Workman [Particle Data Group], PTEP **2022** (2022), 083C01 doi:10.1093/ptep/ptac097
11. F. Wilczek, Phys. Rev. Lett. **39** (1977), 1304 doi:10.1103/PhysRevLett.39.1304
12. T. Sjostrand, S. Mrenna and P. Z. Skands, Comput. Phys. Commun. **178** (2008), 852-867 doi:10.1016/j.cpc.2008.01.036 [arXiv:0710.3820 [hep-ph]].
13. L. Buonocore, C. Frugiuele, F. Maltoni, O. Mattelaer and F. Tramontano, JHEP **05** (2019), 028 doi:10.1007/JHEP05(2019)028 [arXiv:1812.06771 [hep-ph]].
14. J. Liu, N. McGinnis, C. E. M. Wagner and X. P. Wang, JHEP **04** (2020), 197 doi:10.1007/JHEP04(2020)197 [arXiv:2001.06522 [hep-ph]].
15. H. Leutwyler and M. A. Shifman, Nucl.Phys.B**343**(1990), 369-397 doi:10.1016/0550-3213(90)90475-S
16. K. Shiomi *et al.* [KOTO], Nucl. Instrum. Meth. A **664** (2012), 264-271 doi:10.1016/j.nima.2011.11.010
17. J. K. Ahn *et al.* [KOTO], Phys. Rev. Lett. **126** (2021) no.12, 121801 doi:10.1103/PhysRevLett.126.121801 [arXiv:2012.07571 [hep-ex]].

Twin stau as a self-interacting dark matter

Michał Lukawski

Institute of Theoretical Physics, Faculty of Physics, University of Warsaw,
ul. Pasteura 5, PL-02-093 Warsaw, Poland
mlukawski@fuw.edu.pl

Abstract

Supersymmetric Twin Higgs models allow for reducing the fine-tuning with respect to Minimal Supersymmetric Standard Model by protecting the mass of the Higgs boson by additional, accidental global symmetry. This class of models introduce numerous new states, some of which might be candidates for dark matter. Since those reside in twin sector, they are not charged under Standard Model gauge group. We proposed twin stau as a candidate for dark matter. Even though twin stau is charged under twin electromagnetism, since supersymmetric partners obtain large masses from supersymmetry breaking they can easily escape bounds for self-interacting dark matter. The mass of twin stau which reproduces correct relic abundance is usually between 300 and 500 GeV. This scenario can be probed by future direct detection experiments such as Lux-Zepelin.

1 Introduction

The mass of the Higgs particle is not protected from the large corrections from higher energy scales such as Planck mass. One of the most successful mechanisms protecting the mass of the Higgs is supersymmetry, which allows for cancellation of the these corrections above the scale of supersymmetry breaking, m_{SUSY} , at which new particles enter ¹⁾. Naturalness requires that m_{SUSY} is not much above the EW scale, usually at below 1 TeV. Hence, one of the main features of supersymmetric models are relatively light coloured particles which should be produced at LHC in hadron collisions. Since no such signal has been found ²⁾, the minimal implementations of supersymmetry such as Minimal Supersymmetric Standard Model (MSSM) requires large fine-tuning of the parameters to reproduce the correct electroweak scale. One of the mechanisms which can relax the fine-tuning of supersymmetric models is Twin Higgs (TH), first introduced in non-supersymmetric context ³⁾. TH mechanism extends the particle content with partners of all MSSM states and imposes Z_2 symmetry between sectors, which we refer to as visible (even though supersymmetric particles have not been observed yet) and twin. The Higgs particle in this class

of models is then the pseudo-Nambu-Goldstone boson (pNGB) of an accidental, global symmetry of the potential. Its mass is generated by explicit breaking of the global symmetry. Since the mass of the Higgs is proportional to small breaking of the symmetry, it is protected from large quantum corrections.

Twin Higgs models predict existence of numerous new states, some of which could be dark matter (DM) candidates, including dark matter in twin supersymmetric sector ⁴⁾. However, in cases of charged DM, one has to either break or eliminate twin electromagnetism gauge symmetry to escape bounds on self-interacting dark matter. In the following, I will show that in Supersymmetric Twin Higgs (SUSY TH) models twin stau is a viable DM candidate with interesting properties such as long range self-interactions mediated by the twin photon.

More detailed discussion of the results presented here can be found in ⁵⁾.

2 Supersymmetric Twin Higgs

First, let's take a look at the scalar potential of a TH model without referring to supersymmetry for simplicity. As mentioned before, the particle content of the Standard Model is doubled by adding a second, twin sector. In particular, the scalar sector is extended by twin Higgs doublet H' . Additionally, Z_2 symmetry interchanging particles between sectors is imposed. The potential is given by ⁶⁾

$$V(H, H') = \lambda(H^2 + H'^2)^2 - m_{\mathcal{H}}^2(H^2 + H'^2) + \Delta\lambda(H^4 + H'^4) + \Delta m^2 H^2 \quad (1)$$

Note that these doublets form $SU(4)$ fundamental representation $\mathcal{H}_{SU(4)} = (H, H')$. Having that in mind, we clearly see that first and second terms are $SU(4)$ and Z_2 invariant. These terms form Mexican hat potential, which leads to the spontaneous symmetry breaking. The third term breaks $SU(4)$ while preserving Z_2 and is responsible for generation of the mass of the Higgs particle. The last term breaks Z_2 , generating misalignment of the vacuum expectation values (vevs) between sectors parameterized by ratio v'/v . It is necessary since otherwise exact Z_2 symmetry would imply equal decay branching ratio of the Higgs into visible and twin sectors, which is in contradiction with LHC data. Current constraint on invisible Higgs decays imply that $v'/v \gtrsim 3$, ⁶⁾. Misalignment of vevs requires fine-tuning of parameters needed to reproduce the mass of the visible Higgs, which can be parameterized by $\Delta_{v'/v} = (v'^2/v^2 - 2)/2$ which leads to $\mathcal{O}(30)\%$ fine-tuning for $v'/v = 3$ which will be our benchmark for discussion. Fine-tuning at that level means that model is essentially fully natural. It should be mentioned that ratios $v'/v \geq 7$ are disfavored since they require fine-tuning worse than 5%.

As mentioned before, the minimum of the potential breaks symmetry $SU(4)$ to $SU(3)$ generating 7 pNGBs. Six of them give masses to $SU_L(2)$ and $SU'_L(2)$ gauge bosons, while the remaining one is identified with the SM Higgs.

In supersymmetric models, the scalar potential is fully fixed by the gauge interactions (D-terms) and the particle content (F-terms). Hence, the scalar potential of the form (1) cannot be simply added to the lagrangian and should come from either D-term ^{8, 7, 9)} or F-term ^{10, 11)}. In both cases, the tree-level mass of the Higgs is proportional to $\cos^2(2\beta)$, which approaches 1 in the limit of large $\tan\beta = v_u/v_d$. The key difference between those cases is captured by λ dependence on $\tan\beta$. In general, the fine-tuning in SUSY TH is inversely proportional to the quartic coupling λ of the $SU(4)$ invariant term of the potential. In F-term SUSY TH, quartic term is proportional to $\sin^2(2\beta)$, which is maximized for $\tan\beta = 1$ for which tree-level mass of the Higgs vanishes. It is then necessary to use moderate values of $\tan\beta$, which inevitably lead to fine-tuning which requires further model building to alleviate.

In contrast, in D-term SUSY TH, the quartic term is proportional to $\cos^2(2\beta)$ and is maximized for large values of $\tan\beta$. As a result, fine-tuning in these models can be as low as 20% with heavy stops masses

of 2 TeV. We will focus on this case since it seems far more preferable, however most of the analysis presented here is not UV dependent.

3 Twin stau

Twin stau is Z_2 partner of the supersymmetric scalar partner of tau lepton. Hence, it is charged under twin electromagnetism and twin weak interactions $U'_Y(1) \times SU'_L(2)$ and its mass gets large contributions from the supersymmetry breaking. We will consider Z_2 symmetric SUSY breaking, thus soft masses twin stau obtains are equal in visible and twin sectors. To be more specific, the mass matrix of twin stau is given by ¹³⁾

$$m_{\tilde{\tau}'}^2 = \begin{pmatrix} m_{L_3}^2 + \Delta_{\tilde{\tau}_L} + m_{\tau'}^2 & -\mu v' y_\tau \sin(\beta) \\ -\mu v' y_\tau \sin(\beta) & m_{\tilde{e}_3}^2 + \Delta_{\tilde{\tau}_R} + m_{\tau'}^2 \end{pmatrix} \quad (2)$$

where m_{L_3} and m_{R_3} are soft SUSY breaking masses, μ is Higgs mass term, v' is vacuum expectation value of twin Higgs and $m_{\tau'}$ is mass of the twin tau. Note, that it is assumed that there is no Z_2 breaking in Yukawa sector $y_{\tau'} = y_\tau$ and $\tan \beta' = \tan \beta$. The D-term contributions to the mass of the twin stau are given by $\Delta_{\tilde{\tau}_L} = (-1/2 + \sin^2 \theta_W) \cos 2\beta m_Z'^2$ and $\Delta_{\tilde{\tau}_R} = -\sin^2 \theta_W \cos 2\beta m_Z'^2$, where θ_W is Weinberg angle. Mass matrix of stau is obtained by removing all primes.

Note that for $v'/v > 1$, the off-diagonal terms are larger in twin sector than in visible one. It leads to twin stau lighter than stau in the parameter space with large mixing. By making a common assumption that lightest supersymmetric particle is stable, the twin stau can be candidate for a dark matter.

Note that while twin stau DM prefers large off-diagonal mass matrix, μ cannot be arbitrarily large if the model is to remain natural. Assumption of equal Yukawa couplings in both sectors is not necessary and might even be preferable (see ¹⁴⁾ for ΔN_{eff} problem in TH models and how it could be solved by breaking Z_2 in Yukawas ^{14, 15)}), however I will not cover this case.

As mentioned in the introduction, twin stau is charged under twin electromagnetism, which implies that there are long-range self-interactions mediated by massless twin photons. As discussed in ¹⁶⁾ the bound on mass of self-interacting DM have been overestimated and currently the strongest constraint comes from measurements of non-zero ellipticity of gravitational potential of NGC720. For equal couplings of electromagnetism and twin electromagnetism, the lower bound on mass of twin stau is approximately 210 GeV. That is the reason why breaking of twin electromagnetism is necessary in case of charged, non-supersymmetric candidates for dark matter, such as twin taus or mesons.

3.1 Direct detection

Since twin stau belongs to the twin sector, its only interactions with the visible sector must be mediated by the Higgs portal, Fig. 1. Thus, the interactions of twin stau with atomic nuclei are suppressed by mixing between Higgs and twin Higgs, which is roughly given by v/v' . In particular, the effective interaction between the visible SM Higgs and twin stau is given by

$$\lambda_{h\tilde{\tau}'\tilde{\tau}'} = \frac{g}{m_{W'}} \left[\left(\frac{1}{2} c_{\theta_{\tilde{\tau}'}}^2 - s_W^2 c_{2\theta_{\tilde{\tau}'}} \right) m_Z'^2 c_{2\beta} - m_{\tau'}^2 + \frac{m_{\tau'}}{2} \mu \tan \beta s_{2\theta_{\tilde{\tau}'}} \right] \frac{v}{v'} \quad (3)$$

where c_α and s_α are shortcuts for $\cos \alpha$ and $\sin \alpha$, respectively, and $m_{W'}$ is twin W boson mass. Note that this coupling is maximized for large mixing angle $\theta_{\tilde{\tau}'}$, so we expect DD bounds to be strongest in that region.

In our results, we will assume that in the region with $\Omega h^2 > 0.12$, there exists a mechanism which dilutes DM to observed relic abundance. For region with $\Omega h^2 < 0.12$, we rescale the DM cross section with

factor $\Omega h^2/0.12$. It is justified by the fact that it is possible that twin stau constitutes a fraction of DM, but overproduced DM is not physical. A more detailed discussion of the issue can be found in ⁵⁾

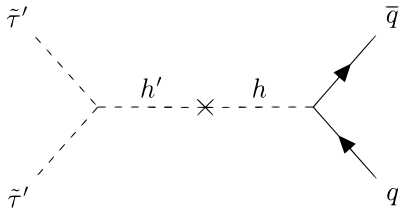


Figure 1: Diagram of twin stau interactions with visible sector quarks. The interaction is mediated by the Higgs portal

4 Results

For the calculation of the relic density, we have modified `Micromegas` ^{17, 18, 19)}. `Micromegas` takes into account twin stau coannihilations within a twin sector, but since in a large portion of the parameter space stau is almost degenerate with twin stau it is necessary to adjust the relic abundance. Upon justified assumption that the annihilation cross section for stau and twin stau is the same, the effective cross section for twin stau is given by

$$\sigma_{\text{eff}} = \sigma \frac{1 + (1 + \Delta)^3 e^{-2x_f \Delta}}{[1 + (1 + \Delta)^{3/2} e^{-x_f \Delta}]^2}, \quad (4)$$

where $x_f = m_{\tilde{\tau}'} / T_f \sim 25$, with T_f the freeze-out temperature. The relic density can then be approximated using $\Omega_{\text{coann}} h^2 = \Omega_0 h^2 \sigma / \sigma_{\text{eff}}$.

First, we will consider the decoupling case where all SUSY breaking masses except the stau are set to 10 TeV, left panel of Fig. 2. We consider $\mu = 1.5$ TeV which is unnatural but is a good starting point for the analysis. As mentioned before, large $\tan \beta$ is preferred both due to naturalness and large twin stau mixing necessary for twin stau LSP. Some of the parameter space is excluded due to mass spectrum. For mostly left-handed twin stau twin sneutrino is always LSP while for mostly right-handed $\tilde{\tau}'$ stau is the LSP and is excluded. For very small soft masses, twin stau is tachyonic due to off-diagonal mass terms proportional to the large μ . In this case, the correct relic abundance is obtained for $m_{\tilde{\tau}'}$ between 260 and 400 GeV, depending on the mixing. Some of the parameter space is excluded due to the direct detection bounds coming from Xenon1T ²⁰⁾ and primary results from Lux-Zepelin (LZ) ²¹⁾. Predicted sensitivity of LZ will allow for probing whole parameters space shown on this plot. The Big Bang Nucleosynthesis (BBN) bound comes from the fact that in this region of parameter space, the difference between masses of stau and twin stau becomes too small to allow $\tilde{\tau} \rightarrow \tilde{\tau}'^\dagger \tau \tau'$ decay. As a result, stau becomes long-lived, and its late decay would change the nuclei composition of the universe. However, in the decoupled case, the lifetime of stau is generically too long. Charged long-lived particles (with decay length above $\mathcal{O}(1)\text{m}$) could have been seen at LHC as charged disappearing tracks if their mass is lower than approximately 430 GeV ²²⁾. Since stau decay is mediated by twin bino and higgsino big, μ and very large M_1 lead to large decay length across whole plot.

A more realistic scenario with $M_1 = \mu = 700$ GeV is shown on right panel of Fig. 2. A large portion of that parameter space has decay length of stau below 1 m. Note that in this plot only small part is

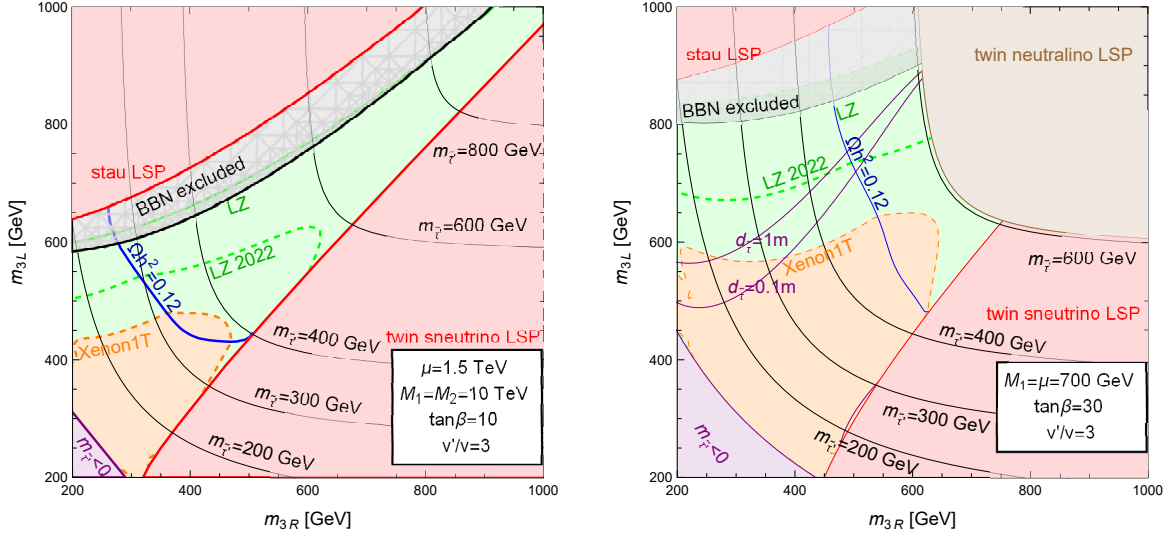


Figure 2: Contour of relic abundance $\Omega h^2 = 0.12$ (blue line) in plane of soft twin stau masses m_{R3} and m_{L3} . In purple region twin stau is tachyonic, in red twin stau is not LSP. Mass contours of twin stau are black. Direct detection bounds from Xenon1T and LZ are coloured orange and green, respectively. Dashed green contour corresponds to new, first results from LZ ²¹⁾

not excluded by either new results from LZ nor by decay length of stau. However, the reason for that is that we keep the most natural, non-excluded value of vevs ratio $v'/v = 3$. One can trade off naturalness for the opening up of the parameter space. I decided to keep the ratio $v'/v = 3$ as originally presented at 7th Young Researchers' Workshop, as well as in ⁵⁾. However, one must keep in mind that new LZ results indicate that the scenario with minimal tuning is now strongly constrained. The final results from Lux-Zepelin will probe the whole parameters space.

Acknowledgements

This work was partially supported by the National Science Centre, Poland, under research grant no. 2020/38/E/ST2/00243.

References

1. R. K. Kaul, Phys. Lett. B **109** (1982), 19-24 doi:10.1016/0370-2693(82)90453-1
2. G. Aad *et al.* [ATLAS], Eur. Phys. J. C **80** (2020) no.8, 737 doi:10.1140/epjc/s10052-020-8102-8
3. Z. Chacko, H. S. Goh and R. Harnik, Phys. Rev. Lett. **96** (2006), 231802 doi:10.1103/PhysRevLett.96.231802
4. M. Badziak, G. Grilli Di Cortona and K. Harigaya, Phys. Rev. Lett. **124** (2020) no.12, 121803 doi:10.1103/PhysRevLett.124.121803
5. M. Badziak, G. Grilli di Cortona, K. Harigaya and M. Łukawski, JHEP **10** (2022), 057 doi:10.1007/JHEP10(2022)057
6. N. Craig, A. Katz, M. Strassler and R. Sundrum, JHEP **07** (2015), 105 doi:10.1007/JHEP07(2015)105

7. M. Badziak and K. Harigaya, *JHEP* **06** (2017), 065 doi:10.1007/JHEP06(2017)065
8. M. Badziak and K. Harigaya, *JHEP* **10** (2017), 109 doi:10.1007/JHEP10(2017)109
9. M. Badziak and K. Harigaya, *Phys. Rev. Lett.* **120** (2018) no.21, 211803 doi:10.1103/PhysRevLett.120.211803
10. A. Falkowski, S. Pokorski and M. Schmaltz *Phys. Rev. D* **74** (2006)
11. S. Chang, L. J. Hall and N. Weiner, *Phys. Rev. D* **75** (2007), 035009 doi:10.1103/PhysRevD.75.035009
12. R. Barbieri, L. J. Hall and K. Harigaya, *JHEP* **11** (2016), 172 doi:10.1007/JHEP11(2016)172
13. S. P. Martin, *Adv. Ser. Direct. High Energy Phys.* **18** (1998), 1-98 doi:10.1142/9789812839657-0001
14. Z. Chacko, N. Craig, P. J. Fox and R. Harnik, *JHEP* **07** (2017), 023 doi:10.1007/JHEP07(2017)023
15. R. Barbieri, L. J. Hall and K. Harigaya, *JHEP* **10** (2017), 015 doi:10.1007/JHEP10(2017)015
16. P. Agrawal, F. Y. Cyr-Racine, L. Randall and J. Scholtz, *JCAP* **05** (2017), 022 doi:10.1088/1475-7516/2017/05/022
17. G. Belanger, F. Boudjema, A. Pukhov and A. Semenov, *Comput. Phys. Commun.* **149** (2002), 103-120 doi:10.1016/S0010-4655(02)00596-9
18. G. Belanger, F. Boudjema, A. Pukhov and A. Semenov, *Comput. Phys. Commun.* **174** (2006), 577-604 doi:10.1016/j.cpc.2005.12.005
19. G. Belanger, F. Boudjema, A. Pukhov and A. Semenov, *Comput. Phys. Commun.* **176** (2007), 367-382 doi:10.1016/j.cpc.2006.11.008
20. E. Aprile *et al.* [XENON], *Phys. Rev. Lett.* **121** (2018) no.11, 111302
21. J. Aalbers *et al.* [LZ], [arXiv:2207.03764 [hep-ex]].
22. M. Aaboud *et al.* [ATLAS], *Phys. Lett. B* **788** (2019), 96-116

EXCLUSIVE VECTOR MESON PHOTOPRODUCTION IN FIXED-TARGET COLLISIONS AT LHCb

Federica Fabiano
Università degli Studi di Cagliari & INFN Cagliari

Abstract

The LHCb forward spectrometer has the unique capability to function as a fixed-target experiment by injecting gas into the LHC beam pipe while proton or ion beams are circulating. The resulting beam+gas collisions cover an unexplored energy range that is above previous fixed-target experiments, but below the top RHIC energy for A-A collisions. The exclusive ρ photoproduction in fixed-target collisions at the LHCb is being investigated, and this report will highlight the importance of this measurement in proton-Neon data with SMOG at $\sqrt{s_{NN}} = 69$ GeV. Indeed, it will probe for the first time the QCD dynamics in a kinematical range complementary to the one studied in the collider mode. Tracking reconstruction performances in Run 3 are discussed as well.

1 Introduction

LHCb is the only experiment among all LHC experiments that can take data both in collider and fixed-target mode. The LHCb fixed-target system, called SMOG (System for Measuring the Overlap with Gas), allows injecting a low flow rate of noble gas into the vacuum vessel of the LHCb VERtEX LOCator (VELO) ^{1, 2}. Albeit it was originally conceived for luminosity measurements, the SMOG system gives the opportunity to study proton-nucleus and nucleus-nucleus collisions onto various target types at different center-of-mass energies. During LHC Run-3, the new system SMOG2 has been put in operation with a new storage cell that allows more efficient beam-gas collisions and several new measurements ³) as shown in Section 2.

The main physics search of this report is the exclusive photoproduction of the neutral vector meson ρ^0 in proton-Neon collisions at $\sqrt{s_{NN}} = 69$ GeV with SMOG. Photon-induced interactions in hadronic collisions allow studies of effects similar to Quark Gluon Plasma (QGP), a dense state of matter where quarks and gluons are free from colour confinement, in regions where QGP is not expected to form. Fixed-target

collisions at the LHC are expected to reach high luminosities ($\mathcal{O}(100\text{-}200 \text{ nb}^{-1})$ per year), which implies that approximately 10^9 events per year will be associated to a ρ produced in an exclusive photon–hadron interaction. As a consequence, the experimental analysis of this process in fixed–target collisions at the LHC is, in principle, feasible⁴⁾ as further discussed in Sections 3 and 4.

An additional topic is reported, which highlights the importance of a step before the analysis procedures: the monitoring and developing of tracking algorithms used to reconstruct Pb-Pb and Pb-SMOG2 events with Monte Carlo simulations after the detector upgrade in Run 3 (Section 5).

2 The LHCb Experiment and its Fixed-Target Programme

LHCb is a dedicated heavy flavour physics experiment at the LHC with the main goal of searching for indirect evidence of new physics in CP violation and rare decays of beauty and charm hadrons. For this reason, the LHCb detector is a single-arm forward spectrometer with a unique coverage in pseudorapidity, $2 < \eta < 5$ ^{5, 6)}.

LHCb is constituted of several sub-detectors. The VELO detector allows reconstructing the precise position of the interaction vertices for collisions occurring in a region of about one meter length along the beam direction, and secondary vertices from heavy flavour decays. The tracking system can determine the momentum of charged particles with a precision that goes from 0.5% at $p < 20 \text{ GeV}/c$ to 1.0% at $200 \text{ GeV}/c$. The unique coverage in pseudorapidity is also fully instrumented with two ring-imaging Cherenkov detectors (RICH), calorimeters (both electromagnetic and hadronic) and a muon system that are exploited to perform the particle identification in the momentum range $[2,100] \text{ GeV}/c$.

The device that allows to turn LHCb into a fixed-target experiment is described in the next section.

2.1 System for Measuring Overlap with Gas: SMOG and SMOG2

By injecting gases in the LHC beam-pipe, LHCb has also operated since 2015 in fixed-target mode, collecting samples with proton and lead beams impinging on gaseous targets. The gas pressure is of the order of 10^{-7} mbar to avoid significant perturbations of the LHC operations. Figure 1 shows the VELO region where SMOG and its upgrade, SMOG2, operate.^{7, 8)}

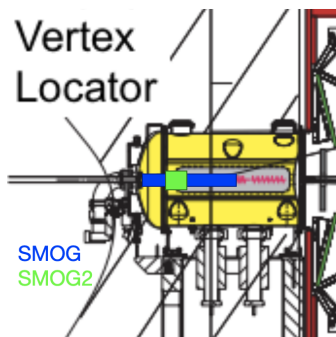


Figure 1: Position of the SMOG (blue) and SMOG2 (green) devices.

The fixed-target configuration guarantees nucleon-nucleon collisions with a centre-of-mass (c.m.) energy

$\sqrt{s_{NN}} \in [41,115]$ GeV, that is between SPS ($\sim 10\text{-}30$ GeV) and RHIC (~ 200 GeV) values. In this unique energy range, the fixed-target programme is expected to probe for instance nucleon and nuclear matter in the domain of high Feynman x_F ¹, the transverse spin asymmetries in the Drell–Yan and quarkonium production as well as the QGP formation⁹).

Since 2022, the SMOG device has been replaced by a storage cell that is located upstream of the nominal LHCb interaction point, SMOG2. This new configuration allows injecting heavier and different noble gases (Kr, Xe, H₂, D₂, O₂, N₂) with a pressure about two orders of magnitude higher than the one of SMOG.³).

The next section focuses on the physics of this report, namely photon-induced interactions in fixed-target collisions.

3 Exclusive Vector Meson Photoproduction

It is important to investigate effects similar to Quark Gluon Plasma (QGP), in regions where QGP is not expected to form. Figure 2 shows the differential cross-section of the photo-produced $\psi(2S)$ in Pb–Pb collisions as a function of rapidity¹⁰). A higher amount of data in the rapidity region covered by LHCb would allow the discrimination among different theoretical models and, as a consequence, a better understanding of the process described in this report.

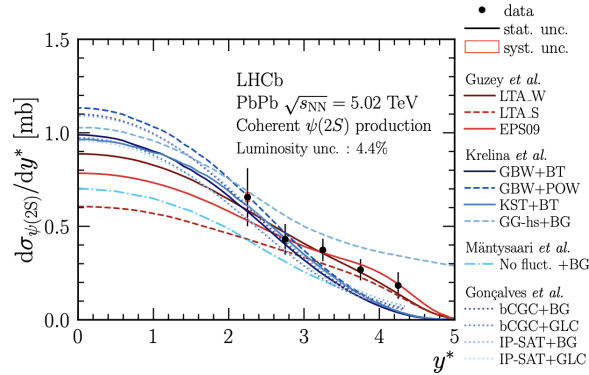


Figure 2: Differential cross-section as a function of the rapidity (y^*) for coherent $\psi(2S)$ production, compared to theoretical predictions. The models are grouped as (red lines) perturbative-QCD calculations and (blue lines) colour-glass-condensate models¹⁰).

Recent studies demonstrated the feasibility of performing experimental analyses of photon-induced interactions in fixed-target collisions⁴). They become dominant in ultra-peripheral collisions (UPCs), where two nuclei collide with an impact parameter, the distance between their centres, larger than the sum of their radii¹¹). Since the nuclei do not overlap, strong interactions are suppressed so that the two ions interact via their cloud of semi-real photons and photon-nuclear interactions dominate. In UPCs, vector mesons are produced from the colourless exchange of a photon from one of the two nuclei and a pomeron from the other. Coherent production occurs when the photon interacts with a pomeron emitted by the

¹Feynman x_F is defined as the fraction of the momentum carried by the parton.

entire nucleus, while for incoherent production, the pomeron is emitted from a single nucleon within the nucleus.

The study of the vector meson photoproduction in hadronic colliders is currently considered one of the most promising processes to improve our understanding of the QCD dynamics and to probe the transverse spatial distributions of gluons in the target ¹²⁾.

4 Analysis Strategy

This analysis has the goal of investigating the coherent photoproduction of the ρ meson in ultra-peripheral proton-Neon collisions. Among all the data collected with SMOG in LHCb Run 2 (2015-2018), the sample considered is the largest one, namely p -Ne collisions at a c.m. energy $\sqrt{s_{NN}} = 69$ GeV. The 2017 p -Ne data has been collected in parallel of high intensity p - p collisions with 2.5 TeV proton beams, with an integrated luminosity $L \sim 210 \text{ nb}^{-1}$. Figure 3 shows all the SMOG data collected through the years and with different noble gases. The highlighted column refers to the sample used in this analysis.

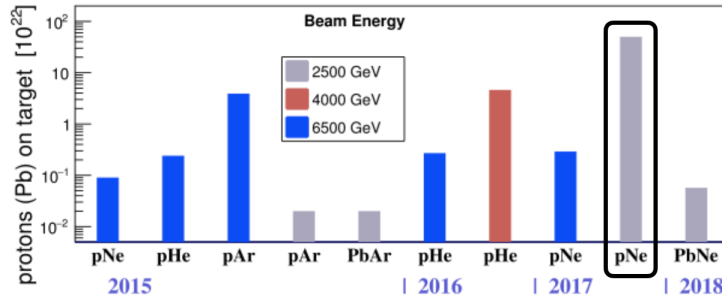


Figure 3: SMOG data collected through the years and with different noble gases ³⁾. The highlighted column refers to the sample considered in this analysis.

As anticipated earlier, the particle considered in this analysis is the neutral vector meson ρ^0 . The information about its mass and width can be found in the PDG ¹³⁾: $M_{\rho^0} = (775.49 \pm 0.34) \text{ MeV}/c^2$ and $\Gamma_{\rho^0} = (147.8 \pm 0.9) \text{ MeV}/c^2$. The reconstruction strategy of the vector meson signal consists in searching for the ρ via its decay products, since it has a very short lifetime ($\sim 10^{-24} \text{ s}$ ¹³⁾). The decay channel considered in the analysis is the preferred one, with a branching ratio $\text{BR} \sim 100\%$: $\rho^0 \rightarrow \pi^+ \pi^-$. The distinctive production mechanism, in which ρ can be observed cleanly, is the exclusive production in ultra-peripheral collisions, as discussed in Section 3. The signature of this decay in UPC is two oppositely-charged pion tracks and nothing else. The data considered for the measurement of ρ mesons were collected from a minimum bias sample, that takes into account every event where a p -Ne interaction occurs. Further selection strategies are being studied to enhance the signal contribution. For this reason, as in previous studies ⁴⁾, a Monte Carlo simulation has been implemented in order to better understand which selection suits best to this analysis, and as a consequence, compute the different contributions to the efficiency.

This result will be the first in fixed-target collisions in a kinematical range complementary to that studied in the collider mode. As a future plan, the same analysis will be reproduced with SMOG2 data.

In order to have a better knowledge of the complete analysis process, the other topic this report fo-

cuses on is the monitoring and developing of tracking algorithms used to reconstruct tracks in Run 3, as described in Section 5.

5 SMOG2 Reconstruction Performances in Run 3

The data acquisition strategy at LHCb has undergone a major upgrade in 2022, and it is now based on a fully-software real-time event reconstruction and selection framework. For this reason, it is crucial to monitor the reconstruction performances and improve them by refining the tracking algorithms currently used, in order to reach even higher multiplicities where QGP is expected to form. This achievement would make LHCb a significant player in the field of heavy-ion physics. Even though the SMOG2 upgrade ³⁾ is expected to have the same reconstruction efficiency between p -He and p - p data, the reconstruction performances of Pb-SMOG2 data are still unknown. For this reason, Pb-Pb data will be crucial to understand the response of the detector in a high-multiplicity collision scenario, and to decide the strategy to be applied to the collection and data analysis of Pb-SMOG2. The tracking algorithms used in Run 2 did not perform efficiently in high occupancy² events (Figure 4 (a)), since they were optimised for p - p collisions, thus unreliable for heavy-ion events. After the upgrade, Run 3 is expected to have better performances without any drop in efficiency (Figure 4 (b)) as seen in the previous run.

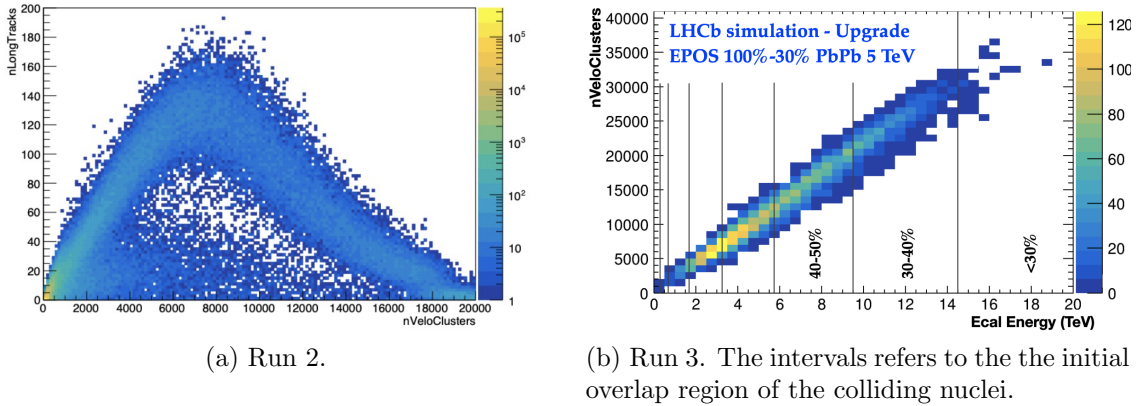


Figure 4: Reconstruction performances in two LHCb runs for Pb-Pb collisions ¹⁴⁾. (a) shows the number of long tracks as a function of the number of clusters in the Vertex Locator, where a drop in efficiency altered the linearity of the trend; (b) reports the number of clusters in the Vertex Locator as a function of the energy in the electromagnetic calorimeter. The information carried by the nVeloClusters variable is related to the initial overlap region of the colliding nuclei (centrality).

The idea to improve the tracking procedure and reduce the misidentified tracks (ghost tracks³⁾ would be to tune the “long tracks”⁴ reconstruction, which have the best momentum resolution and are the most reliable for physics analyses. In the Pb-Pb programme, minor variations of the reconstruction parameters related to the quality of the tracks have already shown the improvement in track reconstruction efficiency, as well as higher reconstruction rate in the different sub-detectors ¹⁵⁾. Following the Pb-Pb approach, after defining the proper parameters for high multiplicity region, the plan is to develop a dedicated

²Occupancy is defined as the fraction of detected photons over the total number of channels.

³The track which has been reconstructed due to the mismatch of hits from separate particles or from detector noise or spill-over.

⁴A long track in LHCb is a track which leaves hits in all tracking sub-detectors.

iterative strategy for the Pb-SMOG2 track reconstruction: the main scheme would be first to find high momentum long tracks, remove the ghosts and then repeat the procedure on the remaining hits in order to reach high efficiency. This tool could show the limitations in the Pb-Pb and Pb-SMOG2 reconstruction, and indicate the route for the further developments needed to successfully observe QGP in LHCb in Run 3.

6 Conclusion and Future Prospects

Several experimental results achieved in the last years by Tevatron, RHIC and LHC have demonstrated that the study of hadronic physics using photon-induced interactions in p - p / p - A / A - A colliders is feasible and provide important information about the QCD dynamics and to probe the transverse spatial distributions of gluons in the target. Recent studies demonstrated the feasibility of performing the same analysis in fixed-target collisions at LHCb, which is the unique experiment with this feature. The study of the exclusive photoproduction of ρ mesons seems promising based on the data sample size. And it will be the first result in fixed-target collisions in a kinematical range complementary to the collider mode one.

As a future plan, the analysis procedure discussed in this report will be reproduced with SMOG2 data.

Moreover, in order to have a better knowledge of the complete analysis procedure, the other topic this report focused on was the monitoring and developing of tracking algorithms used to reconstruct tracks in Run 3, which is expected to show better performances with respect to the previous run.

References

1. C. Barschel, *Precision Luminosity Measurement at LHCb with Beam-Gas Imaging*, PhD thesis, RWTH Aachen U. (2014)
2. R. Aaij et al., Performance of the LHCb Vertex Locator, JINST 9 (2014) P09007, arXiv:1405.7808
3. The LHCb Collaboration, *LHCb SMOG Upgrade*, CERN-LHCC-2019-005; LHCb-TDR-020, <https://cds.cern.ch/record/2673690/files/LHCb-TDR-020.pdf>
4. V. P. Gonçalves, M. M. Jaime, Exclusive vector meson photoproduction in fixed-target collisions at the LHC, Eur. Phys. J. C (2018) 78:693
5. The LHCb Collaboration, JINST 3, S08005 (2008)
6. LHCb collaboration, R. Aaij et al., *LHCb detector performance*, Int. J. Mod. Phys. A30 (2015) 1530022, arXiv:1412.6352
7. C. Barschel, Precision luminosity measurement at LHCb with beam-gas imaging, PhD thesis, RWTH Aachen U., 2014, CERN-THESIS-2013-301
8. M. Ferro-Luzzi, *Proposal for an absolute luminosity determination in colliding beam experiments using vertex detection of beam-gas interactions*, Nucl. Instrum. Meth. A553 (2005) 388
9. A. Bursche et al., Physics opportunities with the fixed-target program of the LHCb experiment using an unpolarized gas target, LHCb-PUB-2018-015; CERN-LHCb-PUB-2018-015

10. The LHCb Collaboration, *Study of the coherent charmonium production in ultra-peripheral lead-lead collisions*, CERN-EP-2022-108 LHCb-PAPER-2022-012, arXiv:2206.08221v1
11. C. A. Bertulani, S. R. Klein, and J. Nystrand, Physics of ultra-peripheral nuclear collisions, Ann. Rev. Nucl. Part. Sci. 55 (2005) 271, arXiv:nucl-ex/0502005
12. S. Klein, D. Tapia Takaki, J. Adam, C. Aidala, A. Angerami, B. Audurier, C. Bertulani, C. Bierlich, B. Blok and J. D. Brandenburg, et al., *New opportunities at the photon energy frontier*, arXiv:2009.03838
13. P.A. Zyla et al. Particle Data Group, Prog. Theor. Exp. Phys. 2020, 083C01 (2020)
14. The LHCb Collaboration, *Upgrade simulations of VELO and SciFi saturations in PbPb collisions at $\sqrt{s_{NN}} = 5$ TeV*, LHCb-FIGURE-2019-021
15. *The LHCb Collaboration*, LHCb upgrade expected reconstruction performance with ions and fixed-target data, 2022, <https://cds.cern.ch/record/2804589>